การปรับปรุงสมบัติเชิงกลของซิลิคอนไนไตรด์โดยใช้วัตถุดิบและกระบวนการผลิตต้นทุนต่ำ

นายนิรุติ หวังหมู่กลาง

วิทยานิพนธ์นี้เป็นส่วนหนึ่งของการศึกษาตามหลักสูตรปริญญาวิทยาศาสตรดุษฎีบัณฑิต
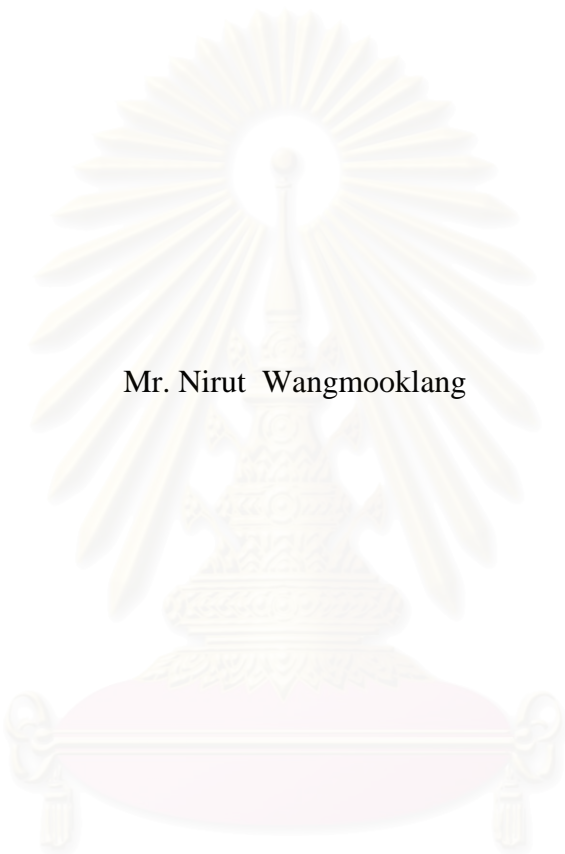สาขาวิชาวัสดุศาสตร์   ภาควิชาวัสดุศาสตร์
คณะวิทยาศาสตร์ จุฬาลงกรณ์มหาวิทยาลัย
ปีการศึกษา 2549

IMPROVEMENT OF MECHANICAL PROPERTIES OF Si_3N_4 USING LOW COST
MATERIALS AND PROCESSES

Mr. Nirut Wangmooklang

A Dissertation Submitted in Partial Fulfillment of the Requirements

for the Degree of Doctor of Science Program in Materials Science

Department of Materials Science

Faculty of Science

Chulalongkorn University

Academic year 2006

Thesis Title   IMPROVEMENT OF MECHANICAL PROPERTIES OF Si$_3$N$_4$
                      USING LOW COST MATERIALS AND PROCESSES
By   Mr. Nirut Wangmooklang
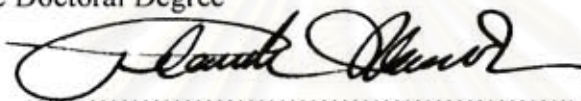Filed of study   Materials Science
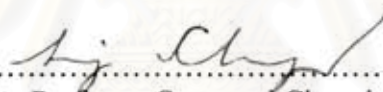Thesis Advisor   Professor Shigetaka Wada, Ph.D.
Thesis Co-advisor   Kuljira Sujirote, Ph.D.
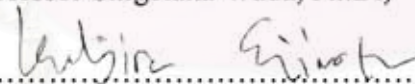Thesis Co-advisor   Thanakorn Wasanapiarnpong, Ph.D.

Accepted by the Faculty of Science, Chulalongkorn University in Partial Fulfillment of the
Requirements for the Doctoral Degree

……………………………………………….. Dean of the Faculty of Science
(Professor Piamsak Menasveta, Ph.D.)

THESIS COMMITTEE
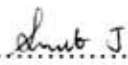
………………………………………….. Chairman
(Associate Professor Saowaroj Chuayjuljit)
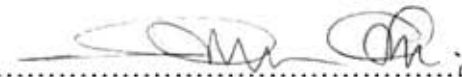
…………………………………..……. Thesis Advisor
(Professor Shigetaka Wada, Ph.D.)

………………………………………….. Thesis Co-advisor
(Kuljira Sujirote, Ph.D.)

………………………………………….. Thesis Co-advisor
(Thanakorn Wasanapiarnpong, Ph.D.)

………………………………………….. Member
(Associate Professor Supatra Jinawath, Ph.D.)

………………………………………….. Member
(Assistant Professor Sirithan Jiemsirilers, Ph.D.)

………………………………………….. Member
(Pavadee Aungkavattana, Ph.D.)

นิรุติ   หวังหมู่กลาง: การปรับปรุงสมบัติเชิงกลของซิลิคอนไนไตรด์โดยใช้วัตถุดิบและกระบวนการผลิตต้นทุนต่ำ (IMPROVEMENT OF MECHANICAL PROPERTIES OF Si_3N_4 USING LOW COST MATERIALS AND PROCESSES) อ.ที่ปรึกษา: ศ. คร.ชิเกทากะ วาดะ, อ.ที่ปรึกษาร่วม: คร.กุลจิรา สุจิโรจน์, อ.คร.ธนากร วาสนาเพียรพงศ์, 119 หน้า.

งานวิจัยนี้ได้ทำการศึกษาถึงความแตกต่างของพฤติกรรมการสูญเสียมวลของซิลิคอนไนไตรด์ระหว่างการเผาซินเทอร์ในเตาบรรยากาศปกติและเผาซินเทอร์ในเตาที่ควบคุมบรรยากาศด้วยแก๊สไนโตรเจน   พร้อมทั้งมีการวิเคราะห์ผลการทดลองอย่างเป็นระบบ   นอกจากนี้ยังศึกษาเพื่อหาองค์ประกอบและภาวะในการเผาซินเทอร์ที่เหมาะสมเพื่อปรับปรุงสมบัติเชิงกลของซิลิคอนไนไตรด์โดยใช้วัตถุดิบและกระบวนการผลิตต้นทุนต่ำ   โดยงานวิจัยนี้ใช้ผงซิลิคอนไนไตรด์และสารเติมแต่งราคาถูกเป็นสารตั้งต้น   และทำการเผาซินเทอร์ทั้งในเตาบรรยากาศปกติและในเตาที่ควบคุมบรรยากาศด้วยแก๊สไนโตรเจน

จากผลการวิจัยพบว่าการสูญเสียมวลของซิลิคอนไนไตรด์ที่เผาซินเทอร์ในเตาเผาบรรยากาศปกติไม่เปลี่ยนแปลงเมื่อเพิ่มอุณหภูมิเผาซินเทอร์   แต่เปลี่ยนแปลงตามปริมาณออกซิเจนหรือซิลิคอนไดออกไซด์ที่มีอยู่ในองค์ประกอบของตัวอย่างก่อนการเผาซินเทอร์ ซึ่งเป็นผลมาจากอิทธิพลของระดับการเปลี่ยนแปลงความดันของความดันไอย่อยออกซิเจน   และการเกิดชั้นซึ่งซึมผ่านไม่ได้ในครูซิเบิล   ในระหว่างการเผาซินเทอร์ ในทางตรงกันข้าม พบว่าการสูญเสียมวลของซิลิคอนไนไตรด์ที่เผาซินเทอร์ในเตาบรรยากาศแก๊สไนโตรเจนจะเพิ่มขึ้นเมื่อเพิ่มอุณหภูมิและระยะเวลาในการเผาซินเทอร์

องค์ประกอบและภาวะในการเผาซินเทอร์ที่เหมาะสมเพื่อให้ได้สมบัติเชิงกลที่อุณหภูมิห้องสูงที่สุดคือ การใช้ผงซิลิคอนไนไตรด์ แมกเนียเซียมออกไซด์ และอะลูมิเนียมออกไซด์ ในอัตราส่วน 96 2 และ 2 เปอร์เซ็นต์โดยน้ำหนัก ตามลำดับ และเผาซินเทอร์ที่อุณหภูมิ 1850 องศาเซลเซียส นาน 2 ชั่วโมง ภายใต้ความดันแก๊สไนโตรเจน 1.0 MPa โดยได้ค่าความแข็งแรงดัด ค่าความทนทานต่อการแตกหัก และค่าความแข็ง เท่ากับ 544 MPa 5.9 MPa m$^{1/2}$ และ 16.0 MPa ตามลำดับ โดยสมบัติเชิงกลที่ได้มีค่าอยู่ในระดับของซิลิคอนไนไตรด์ในเชิงพาณิชย์ที่เผาซินเทอร์แบบปราศจากความดัน

ภาควิชา วัสดุศาสตร์	ลายมือชื่อนิสิต..
สาขาวิชา วัสดุศาสตร์	ลายมือชื่ออาจารย์ที่ปรึกษา.... S. Wada..........
ปีการศึกษา 2549	ลายมือชื่ออาจารย์ที่ปรึกษาร่วม......................
	ลายมือชื่ออาจารย์ที่ปรึกษาร่วม......................

4773820023: MAJOR MATERIALS SCIENCE

KEY WORD: Si_3N_4 / AIR ATMOSPHERE / MASS LOSS / MECHANICAL PROPERTIES / LOW COST

NIRUT WANGMOOKLANG: IMPROVEMENT OF MECHANICAL PROPERTIES OF Si_3N_4 USING LOW COST MATERIALS AND PROCESSES THESIS ADVISOR: PROFESSOR SHIGETAKA WADA, Ph.D., THESIS CO-ADVISOR: KULJIRA SUJIROTE, Ph.D., THANAKORN WASSANAPIRNPONG, Ph.D., 119 pp.

The difference in mass loss behavior of Si_3N_4 between sintering in air atmosphere and sintering under controlled N_2 pressure was intensively studied and the results were systematically evaluated. In addition, the optimal composition and sintering condition for improving the mechanical properties of Si_3N_4 using low-cost materials and processes were investigated. Low-cost Si_3N_4 powder and additives were used as the starting materials. Sintering was performed both under air atmosphere and under N_2 atmosphere.

The results showed that the mass loss of the Si_3N_4 sintered under air atmosphere insignificantly changed with increasing sintering temperature, but significantly increased with the O_2 or SiO_2 contents in the composition before sintering. It was also affected by the pressure gradient of oxygen partial pressure (Po_2) and the formation of the impermeable layer in the crucible during sintering. On the other hand, the mass loss during sintering increased with increasing the sintering temperature and soaking time when Si_3N_4 was sintered under N_2 atmosphere.

The optimal composition and sintering condition for obtaining the highest mechanical properties at room temperature were 96wt% Si_3N_4 + 2wt% MgO + 2wt% Al_2O_3 and sintering at 1850 °C for 2 h under N_2 gas pressure of 1.0 MPa. The flexural strength, fracture toughness and hardness obtained were 544 MPa, 5.9 MPa m$^{1/2}$ and 16 GPa, respectively. The mechanical property values are in the level of commercially available pressureless sintered Si_3N_4 ceramics.

Department __Materials Science__   Student's signature..

Field of study _Materials Science_   Advisor's signature.........._$\mathcal{S}$. _Wada_..............

Academic year ___2006___   Co-advisor's signature..

Co-advisor's signature..

ACKNOWLEDGEMENTS

CONTENTS

LIST OF TABLES

LIST OF FIGURES

Figure   Page

CHAPTER I

INTRODUCTION

1.1 Introduction

Over the past decades, silicon nitride (Si_3N_4) has been known as an excellent material for ideal high-temperature structural applications due to its outstanding physical and mechanical properties under severe environment. Si_3N_4 ceramics have been studied extensively in the last 40 years. The ceramics have a favorable combination of properties that include high strength over a broad temperature range *(1-3)*, moderately high elastic modulus *(1-3)*, high hardness *(2)*, moderate thermal conductivity *(4-5)*, low coefficient of thermal expansion *(6)*, and high fracture toughness *(7)*. From the combination of the properties, Si_3N_4 ceramics have been used for many applications such as cutting tool inserts, bearings, turbocharger rotors, wear parts for many applications, diesel engine parts and so on *(7-10)*. There are several technologies to produce Si_3N_4 products depending on the applications or utilizations. The different production technologies used are reaction bonding (RB), pressureless sintering (PLS), gas pressure sintering (GPS), hot pressing (HP), and hot isostatic pressing (HIP) *(6,11)*.

In spite of the excellent properties of Si_3N_4 ceramics, their widespread use is still limited by their costs with respect to (i) expensive raw materials (Si_3N_4 powder and sintering aids), especially high quality Si_3N_4 powder, and (ii) the high production cost of the processes. Considering the production cost, there are two research works attempting to reduce cost. The one is to sinter Si_3N_4 in conventional air furnace by designing the special container for sintering *(12-14)*. As a result, Si_3N_4

could be sintered under air atmosphere without serious oxidation. Though Si_3N_4 could be sintered to almost full density, the mechanical properties were still low when compared to the commercial Si_3N_4 products. The second is to use low-cost materials. There are several works using low price β-Si_3N_4 powder as a starting material *(15-21)*. Some works obtained rather good mechanical properties; however, the production cost is too high due to sintering at very high temperature and high N_2 gas pressure.

In the phase I of the research entitled "Development of low cost Si_3N_4 ceramics"*(21)*, the experiment has combined both low-cost of production technology (sintering in air atmosphere furnace) and starting materials with low-cost (using β-Si_3N_4 powder and low-cost sintering aids (MgO and Al_2O_3)). In the process, Si_3N_4 could be sintered to almost full density, but the mechanical properties of the sintered body were still low. Moreover, interesting phenomenon relating to the mass loss behavior of Si_3N_4 during sintering in air atmosphere was found. It was significantly different from the mass loss of Si_3N_4 sintered by conventional sintering by controlling the atmosphere with N_2 gas.

Based on the findings of the phase I work, the motivations for the following research are to prove the mass loss phenomenon of Si_3N_4 ceramics during sintering in air atmosphere furnace, and to improve the mechanical properties of Si_3N_4 ceramics by way of lowering the cost of starting materials and lowering the sintering temperature. Therefore, this research is divided into two parts as the following.

Part I: Solid/gas reaction during sintering of Si_3N_4 ceramics in air atmosphere furnace is investigated in order to prove the mass loss phenomena under air atmosphere comparing it under N_2 atmosphere.

Part II: Improvement of mechanical properties of Si_3N_4 ceramics using low-cost materials and processes to the level of practical utilizations.

1.2 Objectives

The major objectives of this research are summarized as follows:

1. Studying on the solid/gas reaction during sintering of Si_3N_4 ceramics in air atmosphere furnace comparing it under nitrogen atmosphere.

2. Finding the optimal composition and sintering condition for improving the mechanical properties of Si_3N_4 ceramics prepared from low-cost Si_3N_4 powder and additives.

Five chapters present the complete view of findings and development obtained in this study. Chapter II is a literature review of basic information and relevant studies of Si_3N_4. Chapter III is the experimental set-up and detailed procedure. Experimental results and discussion are presented in chapter IV. Finally, chapter V includes the summary and the recommendations for future work.

CHAPTER II

LITERATURE REVIEW

2.1 Si$_3$N$_4$ Phases

Silicon nitride (Si$_3$N$_4$) occurs in three crystallographic modifications designated as α, β and γ phases. α and β-Si$_3$N$_4$ have hexagonal structures, which are built up by corner-sharing SiN$_4$ tetrahedra *(11)*. However, their respective structural dimensions are different. The unit cell of α phase is twice as large as the β phase, and they differ in the stacking sequence of the layer subunits along the *c* axis. For the α phase, the stacking is of the *ABCDABCD...*, while for the β phase it is of the type *ABAB...* (see Fig. 2.1a and b). The *AB* layer is the same in α and β phases, and the *CD* layer in the α phase is related to *AB* by a *c*-glide plane. The SiN$_4$ tetrahedra in β-Si$_3$N$_4$ are interconnected in such a way that tunnels are formed, running parallel with the *c* axis of the unit cell. Due to the *c*-glide plane that relates *AB* to *CD*, the α structure contains cavities instead of tunnels.

The newly observed γ-Si$_3$N$_4$ modification can be formed only at extremely high pressures *(22-23)* and has no practical use yet. The cubic γ-Si$_3$N$_4$ is often designated as *c* modification in the literature, in analogy with the cubic modification of boron nitride (*c*-BN). It has a spinel-type structure in which two silicon atoms each coordinate six nitrogen atoms octahedrally, and one silicon atom coordinates four nitrogen atoms tetrahedrally, as seen in Fig.1.1c.

(a)

(b)

(c)
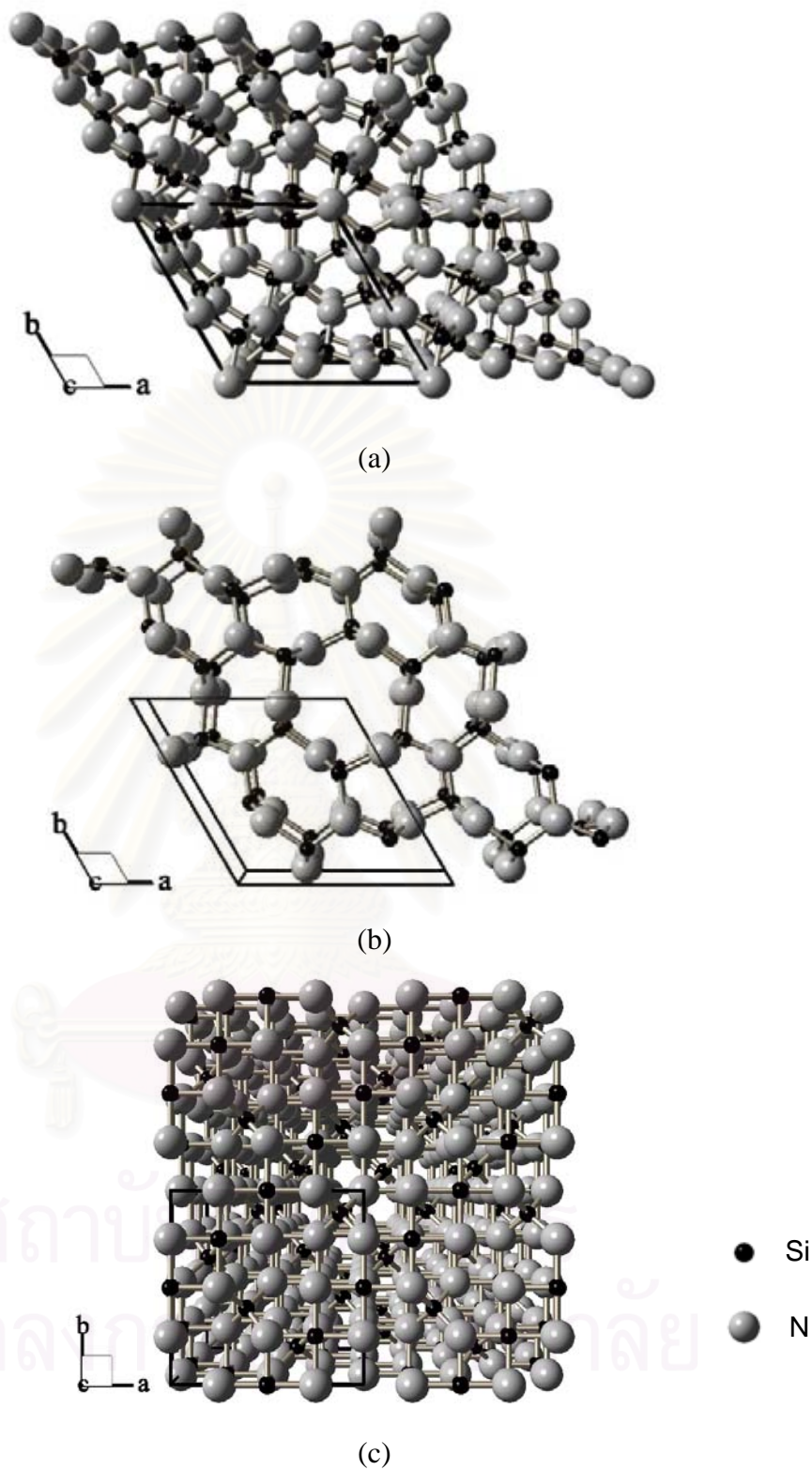
Fig.2.1 Crystal structure stacking model of α-Si_3N_4, β-Si_3N_4 and γ-Si_3N_4: a) The *ABCD* layer stacking in α-Si_3N_4; b) The *ABAB* layer stacking in β-Si_3N_4 along the *c* axis; c) The spinel structure of γ-Si_3N_4. (Black lines indicate a unit cell)

The space group of α-Si$_3$N$_4$ is *P31c*, with the following lattice parameters: $a = 0.7748 – 0.7818$ nm and $c = 0.5591 – 0.5628$ nm, while the axial ratios c/a are reasonable constant. *(24)* The corresponding datum for the β modification is *P6$_3$* with $a = 0.7595 – 0.7608$ nm and c $= 0.2900 – 0.2911$ nm. *(24)* The symmetry of γ-Si$_3$N$_4$ is *Fd-3m* with $a = 0.7738$ nm. While α- and β-Si$_3$N$_4$ can be prepared under normal nitrogen pressure and hence may be widely used commercially, cubic γ-Si$_3$N$_4$ can only be prepared in a diamond anvil cell *(23)* or by shock transformation *(25)* at high pressures and temperatures.

2.2 Si$_3$N$_4$ Powders

2.2.1 Synthesis Routes

Si$_3$N$_4$ is not found in the nature, but can be synthesized in a variety of methods with varying effects on the resulting properties. There are many different production routes for synthesizing Si$_3$N$_4$ powders, namely

- direct nitridation of silicon
- carbothermic reduction nitridation of silica
- diimide synthesis
- vapor phase synthesis
- plasmachemical synthesis
- pyrolyses of silicon organic compounds and
- laser induced reactions.

All of these routes are based on four different chemical processes (Table 2.1).

Table 2.1 Chemical reaction of Si_3N_4 with various synthesizing processes *(26)*

Method	Chemical process
direct nitridation	$3Si\ (s) + 2N_2\ (g) \rightarrow Si_3N_4\ (s)$
carbothermal nitridation	$3SiO_2\ (s) + 6C\ (s) + 2N_2\ (g) \rightarrow Si_3N_4\ (s) + 6CO\ (g)$
diimide synthesis	$SiCl_4\ (l) + 6NH_3\ (l) \rightarrow Si(NH)_2\ (s) + 4NH_4Cl\ (g)$ $3Si(NH)_2\ (s) \rightarrow Si_3N_4\ (s) + 2NH_3\ (g)$
vapor phase synthesis	$3SiCl_4\ (g) + 4NH_3\ (g) \rightarrow Si_3N_4\ (s) + 12HCl\ (g)$

The starting materials are either silicon (Si) powder, silicon dioxide (SiO_2), or silicon tetrachloride ($SiCl_4$), depending upon the process chosen.

Direct nitridation of silicon is an older method. The process is based on the contacting elemental Si with N_2 at temperature in the range of 1200 – 1400 °C. The reaction is highly exothermic. Extreme care must be taken to prevent thermal run-away, which results in melting of Si particles. The direct nitridation is more complicated than the reaction implied in Table 2.1, several models have been proposed to describe the nitridation of Si, *(27-30)* but there is no general agreement regarding the mechanism of the nitridation.

Carbothermal nitridation is a commonly applied method, due to the low cost of starting materials and the relatively high-quality of resulting powders. The starting materials are silica and carbon, both commercially available at low costs. These are reacted at around 1500°C in the presence of nitrogen first to reduce the silica then to nitridate it *(31-33)*. The characteristics of the Si_3N_4 powders resulting from carbothermic reduction depend on many factors namely the C/SiO_2 ratio, the nitrogen flow rate, reaction temperature, particle size and specific surface area of silica and carbon and the impurities present. Although this route has an advantage

over direct nitridation because of the ready availability of the reactants C and SiO_2 compared to Si powder, the process has not yet been commercialized.

Diimide decomposition utilizes $SiCl_4$ and ammonia to produce Si_3N_4 powder *(33-34)*. The first step in this process produces an intimate mixture of ammonium chloride and silicon diimide. Washing with liquid ammonia followed by a sublimation/calcination step produces silicon imide chloride. A final evaporation of the ammonium chloride thus produced yields a mixture of amorphous Si–N compounds which are crystallized above 1250°C, influenced by conditions including such as impurities, heating time, and atmosphere. There is usually residual chlorine impurity in the reaction products. Again, fine powder requires milling to produce. Since the reactants are liquids or gases, very pure Si_3N_4 with a high content of α-phase (>95%) can be prepared *(35)*. However, the production cost is high due to complexities of the process and extensive efforts to purify the intermediate silicon diimide.

The vapor phase synthesis takes place between different gaseous species in the temperature range from 800 °C up to 1400 °C. Usually, the starting materials are $SiCl_4$ and ammonia (NH_3) which react to form amorphous Si_3N_4 *(33)*. Crystallization of the amorphous powder is carried out at temperatures 1300 – 1500 °C. Deagglomeration is also a necessary step to be carried out.

2.2.2 Commercial Si_3N_4 Powders

Si_3N_4 powder of regular, micron to sub-micron sizes can be synthesized by the methods mentioned in 2.2.1. All of those processes involve low-cost raw materials, but subsequent milling and purification steps result in high prices of products. For instance, the direct nitridation is exothermic reaction, hence, it is

difficult to control the temperature caused by thermal run-away. Also, the shape and size of the product powder are difficult to control. In carbothermal reduction of silica, numerous steps are necessary to eliminate co-products, such as silicon carbide (SiC), silicon oxynitride (Si_2N_2O) and remaining carbon *(11,34)*. The post-synthesis heat treatment is required to obtain crystalline form of Si_3N_4 powder from $Si(NH)_2$ obtained in the NH_3-$SiCl_4$ reaction, and NH_4Cl, the by product needs to be removed.

The carbothermal reduction has been employed to produce low grade Si_3N_4 powder, while the direct nitridation and the diimide method have been used to produce high grade powder. Though the diimide process can provide highest quality Si_3N_4 powder, its production costs is higher than that from direct nitridation of Si.

The direct nitridation of silicon is also generally used to produce β-Si_3N_4 powder for refractory purposes *(33)*. Depending on the quality of the starting powders, reaction time and resulting quality are affected. This process generally produces coarse, agglomerated particles, requiring milling to obtain a suitable powder. Therefore, the powder obtained from this production process is inexpensive.

There are many grades of Si_3N_4 powder in the market depending upon the quality of the powder. The good powder for sintering to obtain high quality Si_3N_4 ceramics normally includes high-purity, high α-phase content, free of agglomerations, spherical sub-µm in size, and narrow size distribution *(7,33)*. Typical chemical analysis data and properties for commercial silicon nitride powders synthesized by different techniques as mentioned above are given in Table 2.2.

Table 2.2 Typical properties of Si_3N_4 powders produced by various processing techniques

Technique	Direct nitridation of silicon	Vapor phase synthesis	Carbothermal nitridation	Diimide synthesis
Specific surface area (m^2/g)	8-25	3.7	4.8	10
Oxygen content (wt%)	1.0-2.0	1.0	1.6	1.4
Carbon content (wt%)	0.1-0.4	-	0.9-1.1	0.1
Metallic impurities (wt%) Σ Fe, Al, Ca	0.07-0.15	0.03	0.06	0.005
Crystallinity (%)	100	60	100	100
$\alpha/(\alpha + \beta)$ (%)	95	95	95	>95
Morphology	equiaxed	equiaxed + rod-like	equiaxed + rod-like	equiaxed

2.3 Sintering Methods of Silicon Nitride Ceramics

2.3.1 Conventional Sintering Methods

The high degree of covalent bond of Si–N makes it very difficult to produce pure dense Si_3N_4 ceramics by classical sintering (simple heating of powder compacts) *(36)*. The main reason for this is that the diffusion of silicon (at 1400 °C $D_{Si} \approx 0.5 \times 10^{-19}$ m^{2}s^{-1}) and nitrogen (at 1400 °C $D_N \approx 6.8 \times 10^{-10}$ m^{2}s^{-1}) in the volume or at the grain boundaries of Si_3N_4 is extremely slow *(11)*. Moreover, at high temperatures Si_3N_4 starts to dissociate *(37,38)*. Therefore, sintering additives are utilized as a possibility to promote liquid phase sintering and thus enhance volume or grain boundary diffusion.

Dense Si_3N_4-based ceramics can only be produced, on a technologically interesting scale, in combination with addition of sintering aids. Almost every Si_3N_4 ceramic contains at least one of the sintering aids: MgO *(39-42)*, Al_2O_3 *(43-45)*, Y_2O_3 *(46-49)*, AlN *(50)*, BeO *(51-52)*, CeO_2 *(53-55)*, ZrO_2 *(56)*, Yb_2O_3 *(57-58)*, etc., and magnesia, alumina and yttria are the most widely used ones. The most common sintering methods used to consolidate Si_3N_4-based ceramics are as follows:

- Reaction bonding (RB)

- Pressureless sintering (PLS)

- Gas pressure sintering (GPS)

- Hot pressing (HP)

- Hot isostatic pressing (HIP)

Reaction bonding implies a direct reaction between Si and N_2 during the sintering. By this method, complex shapes can be produced using various ceramic forming methods (slip casting, injection molding, die pressing, isostatic pressing) with low costs. However, this process often results in materials with high porosity (about 70-88%) resulting in poor mechanical properties. Furthermore, the pore structure leads to high oxidation rates and to small erosion resistance *(36)*. Thus, low densities and pore structure limit the range of possible applications of RBSN materials.

For the pressureless or normal sintering (SSN), the powder mixtures (Si_3N_4 plus additives) are compacted to required shapes by various shaping methods. The sintering is performed under 0.1 MPa N_2 at 1700 – 1800 °C. Complex-shaped components of dense Si_3N_4 which require little machining remain after sintering. Because the highest sintering temperature is restricted by thermal dissociation of

Si_3N_4 *(37,59-60)*, relatively large amounts of additives are necessary to fabricate high density materials. It is very difficult to get fully dense Si_3N_4-based ceramics without introducing a large amount of liquid phase, using pressureless sintering.

Gas pressure sintering implies that the specimens are sintered in an appropriate gas atmosphere at high pressures. High nitrogen pressures are used in connection with gas pressure sintering of Si_3N_4 based ceramics, which prevents decomposition of Si_3N_4, and higher sintering temperatures can accordingly be applied. This method allows sintering of complex-shaped parts with medium cost.

Hot pressing is the most established pressure-assisted sintering method, in which the specimen is placed in a die and an axial pressure is applied by punches. Both the die and the punches are made of graphite or boron nitride-coated graphite, and the whole assembly is placed in a furnace. Although the applied pressure promotes the densification of the specimen, the method has severe limitations when it comes to preparation of specimens of complex shapes. Because of high cost and difficulties to machine the components, hot-pressing, today, has limited use for the production of simple shaped parts and low quantities.

In the HIP process the isostatic pressure is applied via a gaseous medium, which allows manufacturing of more complicated-shape components in large quantities. For silicon nitride ceramics, the green bodies are usually coated with a glass that acts as a gas-tight protective membrane against the gas used as pressure medium. The furnace is placed in a pressure vessel, and a high-pressurised gas (normally argon) is pumped into the vessel during the sintering cycle. During this process a high gas pressure is applied to consolidate a powder compact or to remove the residual porosity from presintered bodies. The uniform manner of applying the high pressure results in fully isotropic material properties. The possibility to use much

higher pressures than in uniaxial hot-pressing leads to an enhancement in the densification of the products. Thus, fully dense ceramic parts can be produced from powders of lower sintering activity and with smaller amounts of additives as compared with unaxial hot pressing. However, the entire set-up is quite complicated and costly, and the glass coating and de-glassing procedures are also very time-consuming.

2.3.2 Sintering of Si_3N_4 under Air Atmosphere

Pressureless sintering of Si_3N_4 ceramic in a N_2 gas furnace is a common sintering method that is thought to be a low-cost fabrication. However, N_2 gas furnace is still special comparing to air furnace. According to Wada et al *(12-13)*, Si_3N_4 could be sintered without serious oxidation under air atmosphere. Isolating Si_3N_4 specimen from air, it is set in a special crucible structure shown in Fig. 2.2.
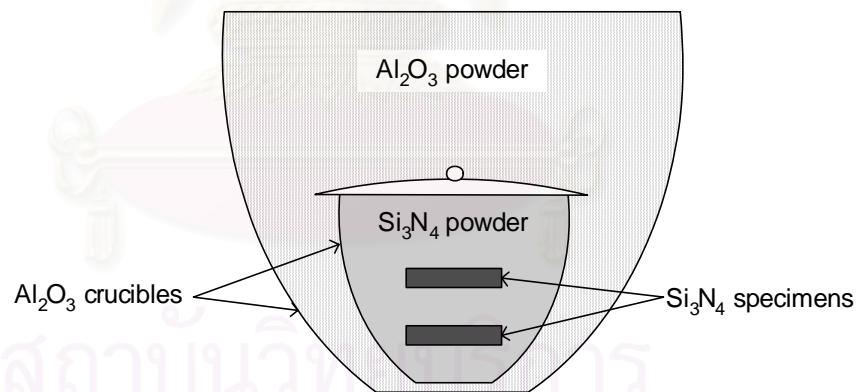
Fig. 2.2 Schematic crucible structure for sintering Si_3N_4 under air atmosphere

Si_3N_4 specimens are buried in Si_3N_4 powder in the smaller crucible and Al_2O_3 powder in the larger crucible. The packing powders (Al_2O_3 and Si_3N_4 powders) helps the Si_3N_4 specimens to protect oxygen from outside that will come to react with the specimens during sintering. When Si_3N_4 ceramics are sintered in the mentioned crucible structure, the Si_3N_4 powder consumes oxygen in the crucible via reaction

(2.1) and then, when Po_2 in the crucible decreases to below 10^2 Pa, reaction (2.2) occurs, three moles of O_2 (g) change to 6 mol of SiO (g) and 4 mol of N_2 (g).

$$Si_3N_4 \text{ (s)} + 3O_2 \text{ (g)} \quad \rightarrow \quad 3SiO_2 \text{ (l)} + 2N_2 \text{ (g)} \qquad (2.1)$$

$$2Si_3N_4 \text{ (s)} + 3O_2 \text{ (g)} \rightarrow \quad 6SiO \text{ (g)} + 4N_2 \text{ (g)} \qquad (2.2)$$
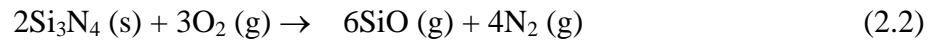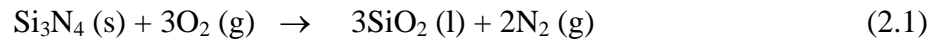
Therefore, once active oxidation occurs, the generated gas increases in volume and flows out through the gap of the crucible, thereby decreasing the oxygen partial pressure in the crucible and protecting the diffusion of air from outside of the crucible. After most of the oxygen in the crucible has reacted with Si_3N_4, the generated gas flow stops and air will again diffuse into the crucible. However, since the crucible is filled with Si_3N_4 powder, oxygen diffusing into the crucible reacts with Si_3N_4 powder near the gap of the crucible and these will not reach the Si_3N_4 specimen. Recently, Plucknett and Lin *(14)* have also sintered Si_3N_4 in air atmosphere furnace, but the crucible structure differs from the structure mentioned above.

2.4 Liquid Phase Sintering

Liquid-phase sintering (LPS) is defined as a sintering process that involves liquid and solid particles. This is a conventional technique that has been used to manufacture ceramics for many centuries. LPS is important for systems which are difficult to densify by solid state sintering, i.e. ceramics that possess a high degree of covalent bonding e.g., (Si_3N_4 and SiC). The liquid is normally produced from a mixture of at least two powders, a major component and an additive. On heating of the mixture, the additive melts or reacts with a small part of the major component to form a eutectic. The amount of liquid produced at the sintering temperature is usually maintained in the range of 5 – 15 vol%.

According to Kingery's model, the classic liquid-phase sintering process can be divided into three steps that may in certain cases be partly overlapped *(61)*, see Fig.2.3.
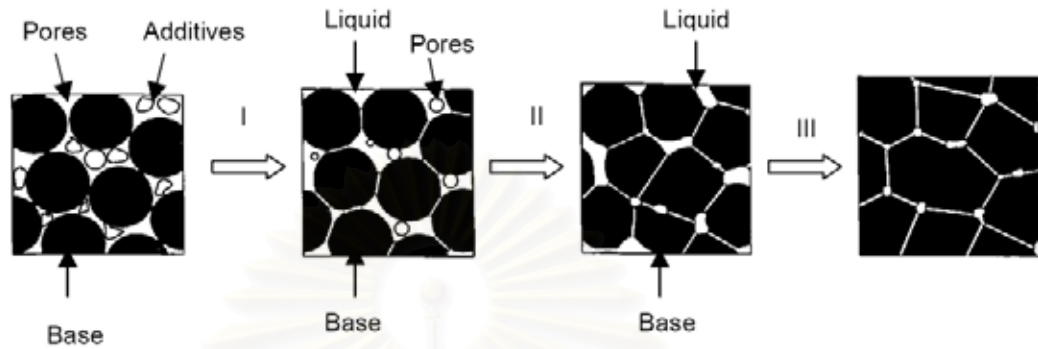
Fig. 2.3 A schematic drawing showing the microstructural evolution during classic liquid-phase sintering of powder mixtures: I) Rearrangement, II) Solution–precipitation; and III) Microstructure coarsening and solid-state sintering.

The mechanisms for classic liquid-phase sintering have been described in detail by Kingery *(61-62)* and German *(63)*. In order to understand these mechanisms, a number of experimental and theoretical investigations were made. All of them come to the same conclusion that the LPS process occurs in three stages, so that there is some degree of overlapping between the theories. Classically, the following sequence of sintering stages is considered to be prevailing:

1. Particle rearrangement

2. Solution-reprecipitation

3. Solid-state sintering

2.4.1 Particle Rearrangement

Particle rearrangement takes place immediately after the liquid phase forms, accompanied by rapid partial densification due to the capillary force exerted by the wetting liquid on the solid particles. The elimination of porosity takes place as the system minimises its surface energy. The most favourable features for rearrangement are: *(i)* A homogeneous distribution of a congruently melting liquid that wets the particles present; *(ii)* The solid particles are soluble in the liquid; *(iii)* A large solubility ratio. The rate and extent of shrinkage depend upon the viscosity and quantity of liquid phase formed and on its wetting properties. This process is rapid. However, except for large liquid contents, it cannot lead to complete densification. Many parameters, such as the amount of liquid, its viscosity, green density, wetting, sintering temperature etc. strongly affect this stage. Kingery's model gives an empirical approach in which the rate of densification corresponds approximately to the viscous flow and follows a relation as given in equation (2.3).

$$\frac{\Delta L}{L_0} \approx (\frac{1}{3}) \frac{\Delta V}{V_0} \approx t^{1+y} \tag{2.3}$$

where ΔL is the change in length and L_0 the original length, ΔV and V_0 correspond to the change in volume and initial volume respectively. The exponent $1+y$ is slightly greater than unity due to the fact that pore sizes decrease and the driving force increases during the process, while at the same time t, the resistance to rearrangement, increases from the initially pure viscous flow. There are other approaches to analyzing the rearrangement during liquid-phase sintering, such as analysis of the capillary forces between particles separated by a liquid layer. All of these models are quite complex and calculations are very cumbersome.

2.4.2 Solution-Reprecipitation

The small grains are more soluble than the large ones, and the difference in solubility establishes a concentration gradient in liquid. Material is therefore transported from small grains to large grains by diffusion, so that the large grains grow at the expense of the small during the liquid-phase sintering. This process is known as coarsening, or static Ostwald ripening. The major driving forces for Ostwald ripening are the reduction of interfacial energy and the capillary force. This process relies strongly on two critical steps: dissolution of solid into the liquid and diffusion through the liquid. If the transport is limited by mass transfer from the source to the sink, this process is diffusion-controlled; if the transport is confined by interfacial dissolution or precipitation, the process is reaction-controlled. Ostwald ripening plays an important role during the solution–reprecipitation step. It contributes not only to grain growth but also to densification.

2.4.3 Solid-State Sintering

The final step of liquid-phase sintering is controlled by densification of the solid structure. A solid skeleton is formed, and grain coalescence occurs. The rigidity of the solid skeleton hinders further rearrangement, although microstructure coarsening continues by diffusion. In this case, the residual pores will enlarge if they contain entrapped gas that results in swelling. The densification rate is greatly decreased during this part of the sintering cycle. The three stages of liquid-phase sintering are sketched as a sintering curve in Fig. 2.4.

Densification (%)
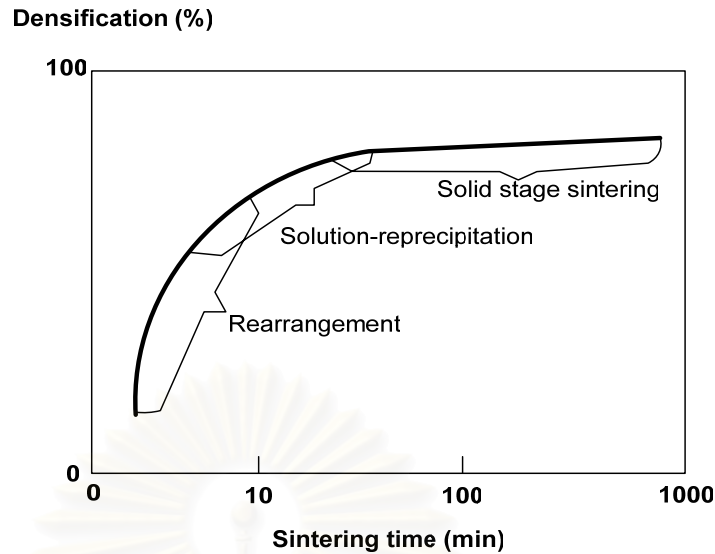
Fig. 2.4 Schematic diagram illustrating the three stages of liquid-phase sintering on a typical sintering curve

Particle rearrangement is the process occurring in the fastest on a time scale of minutes *(64)*. The solution-reprecipitation process and skeleton sintering depend on diffusion through the liquid and solid, respectively, and hence, are slower in comparison to particle rearrangement stage.

2.5 Liquid Phase Sintering of Si_3N_4

Many manufacturing techniques such as pressureless sintering, gas pressure sintering, hot pressing and hot isostatic pressing that are employed for obtaining dense Si_3N_4 bodies are related to liquid-phase sintering. At high temperatures the introduced metal oxides react with the SiO_2 that is always present at the surface of each Si_3N_4 particle, and with the small Si_3N_4 particles to form an oxynitride liquid phase, which wets solid particles and allows rearrangement of them. With increasing temperature, more nitride particles dissolve in the liquid, β-Si_3N_4 or sialon (SiAlON) phases (if possible) will precipitate when the liquid has become supersaturated, and this promotes densification by the mechanism of liquid-phase

sintering. The sintering behavior of Si_3N_4 ceramics is affected directly by the characteristics of the liquid phase present. If the liquid fulfills the conditions of good wettability and solubility of Si_3N_4, densification can be described according to the standard mechanisms of liquid phase sintering: particle rearrangement, solution-reprecipitation and particle coalescence (or grain growth). However, the mechanism of sintering Si_3N_4-based ceramics is much more complicated than that of liquid-phase sintering of hard metals, because intermediate compounds can be formed and phase transformations occur during the sintering process, which all consume the liquid phase and/or alter the composition of the liquid *(65-67)*.

2.5.1 Densification

Once the liquid is formed, densification takes place through particle rearrangement, due to capillary forces. The extent of particle rearrangement mainly depends on the size and shape of particles and amount and viscosity of the liquid phase. The rearrangement process ceases when interparticle contacts are formed that prevent the system from further densification. After formation of the particle bridges, however, the solution-precipitation process starts resulting in the collapse of the bridging. This leads to densification by secondary rearrangement. The driving forces for the second stage are the higher solubility at the contact points of the particles and the differences in the chemical potentials between small and large particles that lead to dissolution of small particles and precipitation of matter on the surface of larger particles.

2.5.2 Phase Transformation

The α-Si_3N_4 phase is thermodynamically unstable during sintering (e.g. at 1400-2000 °C and 0.1 to 100 MPa N_2 pressure *(68))* and shows a tendency to

transform into the more stable β-Si_3N_4. The transformation is reconstructive transformation *(69)*. This process involves the breaking and reforming of Si-N bonds. The nearest neighbor atoms remain the same in both the crystallographic forms. The reverse β-Si_3N_4 to α-Si_3N_4 transformation has never been observed, but it would be expected to be too slow to be detected at temperatures < 1400°C.

Phase transformations play an important role for microstructural development. Different microstructures are possible depending on the location where reprecipitating of solute occurs. This location of reprecipitation can be either new β-nuclei generated by supersaturation or the pre-existing β-grains, which coexist with the α-phase in the starting powders *(66)*. The precipitation on pre-existing β-grains results in a coarser and more equiaxed structure *(66,70)*.

2.5.3 Grain Growth

Growth of Si_3N_4 grains is commonly observed during sintering. The driving force originates from the curvature difference between grains. Si_3N_4 prism planes are more stable compared to basal planes. However, basal planes grow faster than the prism planes resulting in needle-like grain morphology. The growth kinetics can be described by the following formula:

$$G^n - G_0^n = kt \tag{2.4}$$

Where G = average grain size, G_0 = initial grain size, k = kinetic constant, and t = observation time. The grain growth occurs in order for it to reach a steady state. When the grains grow in a steady state, the normalized grain-size distribution is invariant with time, independent of the initial grain-size distribution, and the exponent n is 3 for diffusion control *(71)* and 2 for interface-reaction control *(72)*.

Finally, the consolidation, phase transformation and microstructural development of Si_3N_4 materials in the presence of a liquid phase can be summarized into several regimes as shown in Fig. 2.5.
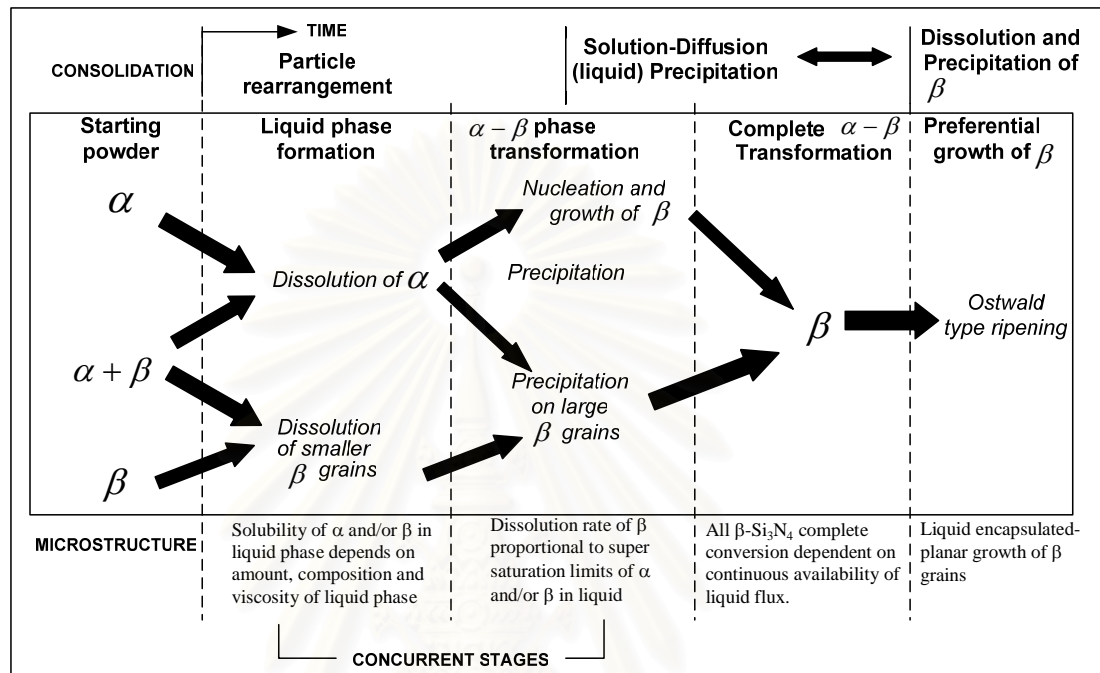
Fig. 2.5 Microstructural development during liquid phase consolidation of various types of Si_3N_4 powder (after Sarin *(66)*)

2.6 Microstructure of Si_3N_4 Ceramics

Sintered Si_3N_4 specimen consists mainly of β-Si_3N_4 and amorphous grain-boundary phase. During cooling, the liquid solidifies to amorphous or partially crystalline secondary phases, which are located either at the grain boundaries in the form of thin layers or at triple junctions. This intergranular phase strongly affects the mechanical properties, especially at high temperature. A typical feature of sintered Si_3N_4 ceramics is the morphology of Si_3N_4 grains. Residual α-grains are equiaxed. β-phase exhibits an elongated grain structure with an aspect ratio (ratio of length to thickness or diameter) usually in the range of 3 to 10 *(73-76)*.

The microstructural development is controlled mainly by Si_3N_4 starting powder, additive composition and sintering condition. It has been shown that the aspect ratio of β-Si_3N_4 grains is strongly influenced by the number and size of β-seeds of the starting powder *(77)*. In the extreme case of β-rich powders (>95 %), steric hindrance is already effective at the beginning of densification. The resulting microstructure is fine-grained, homogeneous and equiaxed grains. Figure 2.6 shows two Si_3N_4 microstructures densified under the same conditions and with the same sintering additives but different Si_3N_4 starting powders.
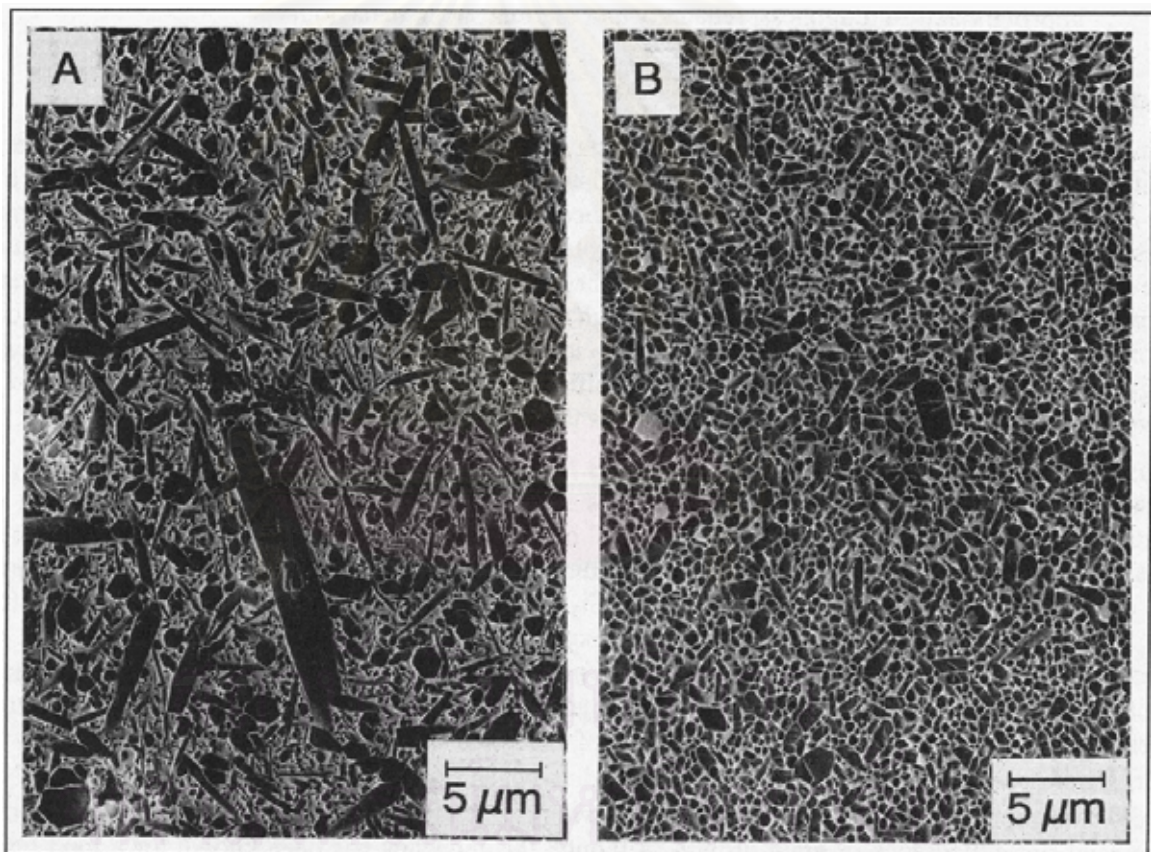
Fig. 2.6 Plasma etched Si_3N_4 microstructure of (A) an α-rich Si_3N_4 and (B) a β-rich Si_3N_4 powder. (After Hoffmann *(77)*)

2.7 Mechanical Properties of Si_3N_4 Ceramics

Typical data for the properties of commercial hot-pressed and pressureless sintered Si_3N_4 are presented in Table 2.3. It can be inferred from the given data that Si_3N_4 possesses high strength, good thermal-shock resistance due to the low coefficient of thermal expansion and relatively good resistance to oxidation compared to other high-temperature structural materials.

Table 2.3 Typical properties (at room temperature) for hot-pressed and pressureless sintered Si_3N_4 *(78)*

Property	Hot pressed Si_3N_4	Pressureless sintered Si_3N_4
Density (g/cm^3)	3.29	3.27
Thermal conductivity (W/mK)	30	29
Flexural strength (MPa)	830	690
Hardness (GPa)	15.8	14.5
Thermal expansion (10^{-6}/°C)	3.3	3.3
Young's modulus (GPa)	310	310
Toughness-K_{IC} (MPa.m$^{1/2}$)	6.1	5.7
Poission's ratio	0.27	0.24

The mechanical property of Si_3N_4 ceramics depends on pores present, cracks and inclusions. Among these factors, porosity has been demonstrated to have a pronounced effect on strength. Figure 2.7 shows the relationship of the relative density and strength of pressureless sintered Si_3N_4 with yttria and alumina additives.
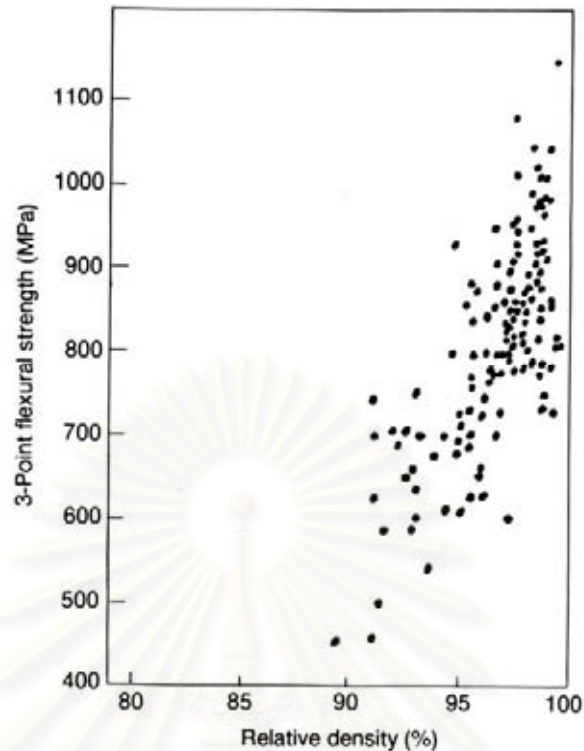
Fig. 2.9 Dependence of the strength of pressureless sintered Si_3N_4 on the density. (After Komeya *(79)*)

Moreover, the mechanical properties of Si_3N_4 are strongly influenced by their grain morphologies. For instance, the influence of different microstructure caused by sintering aids on the flexural strength and fracture toughness is presented in Table 2.4.

Generally, the strength of a brittle material is proportional to the fracture toughness and indirectly proportional to the square root of the defect size. The defect size of the materials can be reduced by optimized processing. The highest measured mean three-point bending strength for Si_3N_4 was 2000 MPa *(81)*. This corresponds to a defect size of about 5 μm. Materials with a strength level of 1400 to 1500 MPa usually have a defect size of 10 μm, i.e. these materials have to have a grain size lower than that of the defect, because larger grains can act as strength-determining defects. This means that high strength materials must be fine-grained.

Table 2.4 Characteristics of different Si_3N_4-based compositions (After Pyzik *(80)*)

| Composition | Grain-size distribution (%) | | | Number of grains per 100 μm² | Fracture toughness (MPa·m^1/2) | Flexure strength (MPa) | Schematic illustration of microstructure |
	$D > 2$ μm	1 μm $< D < 2$ μm	$D < 1$ μm				
A Si₃N₄ + 15 wt% MgO	6.8	13.7	79.5	127	4.7	352	
B Si₃N₄ + 14.5 wt% MgO + 0.5 wt% CaO	3.0	9.3	87.7	163	4.6	380	
C Si₃N₄ + 15 wt% Y₂O₃	2.6	6.4	91.0	267	5.2	580	
D Si₃N₄ + 14.5 wt% Y₂O₃ + 0.5 wt% CaO	1.2	12.0	86.8	240	5.1	540	
E Si₃N₄ + 7.5 wt% Y₂O₃ + 7.5 wt% MgO	1.0	11.1	88.9	260	5.9	650	
F Si₃N₄ + 7.25 wt% Y₂O₃ + 7.25 wt% MgO + 0.5 wt% CaO		5.2	94.8	257	8.0	890	

Fracture toughness differs mainly with variations in the microstructure. The grain shape and the size and phase composition of the grain-boundary phase have a strong influence. Normally, the fracture toughness increases with the square root of the grain size *(16,82-83)*. High fracture toughness of Si_3N_4 based ceramics could be explained on the basis of similar toughening mechanisms as in whisker reinforced composite materials (grain bridging, pull-out, crack deflection, and crack branching *(84-86)*. However, these toughening mechanisms are only active when the dominant fracture mode is intergranular. The ratio of transgranular to intergranular fracture depends on the strength of both intergranular-phase and Si_3N_4 grains. A material with

higher toughness has a weaker grain boundary. On the other side, the strength of the grain-boundary phase is connected with the local residual stresses *(87)*. When the thermal expansion coefficient of the grain-boundary phase is higher than that of the Si_3N_4 grains, the grain-boundary phase is under tensile stress and the fraction of intergranular fracture is high. As a result, the fracture toughness increases. In contrast, ceramics with a grain boundary phase under compression have low fracture toughness because of a higher amount of transgranular fracture *(88)*.

CHAPTER III

EXPERMENTAL PROCEDURE

3.1 Characteristics of Starting Materials

The β-Si_3N_4 powder (SN-F2, DENKA, Japan) is a low-cost powder produced by the direct nitridation method. Chemical composition of the powder was provided by the manufacturer (Denki Kagaku Kogyo K.K. Co.,Ltd., Japan). The impurity contents are given in Table 3.1.

Table 3.1 Characteristic of as-received β-Si_3N_4 powder

β-phase content	~100 %
Fe	0.2 %
Na^+	5 ppm
Cl^-	1 ppm
Fe^{++}	2010 ppm
pH	9
+150 µm	< 0.01 %
− 96 µm	93 %
− 48 µm	66 %
D_{50}	29 µm

The sintering aids for this experiment are commercial MgO (MJ-30 grade, Iwatani Chemicals Co.,Ltd., Japan), Al_2O_3 (AKP-30 grade, Taimei Chemicals Co., Ltd., Japan) and Y_2O_3 (Shin Etsu Chemicals Co., Ltd., Japan). The impurity contents provided by the manufacturers are shown in Table 3.2, 3.3 and 3.4, respectively.

Table 3.2 Characteristic of MgO powder used as additive

MgO	99.9 %
Fe	0.0015 %
Si	0.0031 %
Al	0.0011 %
Ca	0.0001 %
Mean particle size	0.35 µm

Table 3.3 Characteristic analysis of Al_2O_3 powder used as additive

Al_2O_3	99.99 %
Fe	$\leq$ 20 ppm
Si	$\leq$ 40 ppm
Na	$\leq$ 10 ppm
Mg	$\leq$ 10 ppm
Cu	$\leq$ 10 ppm
Packed bulk density	1.1~1.5 g/cm^3
Loose bulk density	0.7~1.1 g/cm^3
Mean particle size	0.4~0.6 μm
Specific surface area	4 ~ 6 m^2/g

Table 3.4 Characteristic analysis of Y_2O_3 powder used as additive

Y_2O_3	99.9 %
CaO	0.0007 %
Al_2O_3	0.001 %
Fe_2O_3	0.001 %
SiO_2	0.0087 %
Specific surface area	29.9 m^2/g
Mean particle size	4.6 μm

The coarse particle Al_2O_3 powder (A-11 garde, Fuji Kasei Co., Ltd., Japan) was used as packing powder for the experiment of sintering Si_3N_4 in air furnace. The specification provided by the manufacturer is given in Table 3.5.

Table 3.5 Characteristic analysis of Al_2O_3 powder used as packing powder

Fe_2O_3	0.01 %
SiO_2	0.01 %
Na_2O	0.30 %
Al_2O_3	99.7 %
H_2O	0.06 %
L.O.I	0.01 %
True specific gravity	3.93 g/cm^3
Mean particle size	63 μm

Part I:

3.2 Experiments on Gas/Solid Reaction during Sintering of Si_3N_4 in Air Atmosphere

This experiment was conducted in order to study the mass loss phenomena of Si_3N_4 during sintering under air atmosphere. The experimental procedures are as follows:

3.2.1 Experimental Flow Chart

The preparation method for sintering Si_3N_4 under air atmosphere is schematically represented in Fig. 3.1.
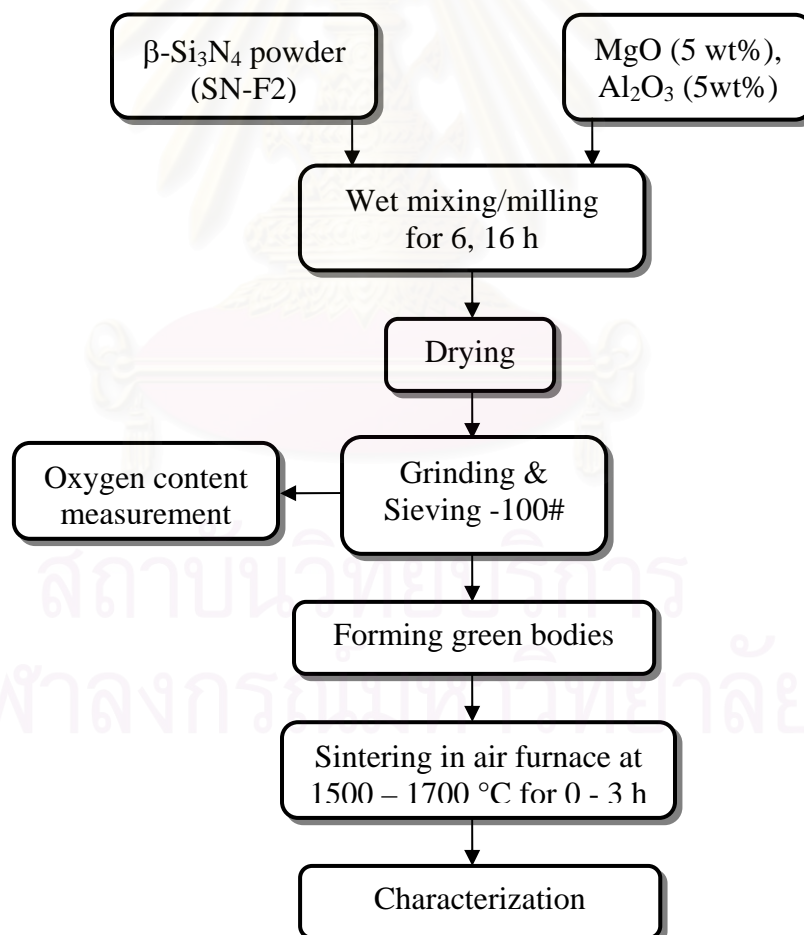
Fig. 3.1 Experimental flow chart for the sintering of Si_3N_4 under air atmosphere

3.2.2 Powder Preparation

The β-Si_3N_4 powder was mixed/milled with 5 wt% MgO and 5 wt% Al_2O_3 by attrition mill using Si_3N_4 balls of 5 mm in diameter as grinding media. The rotation speed is 500 rpm. The weight ratio of powder : medium : grinding media balls is 1 : 3 : 12. The mixture with mixing time for 6 h in ethanol was denoted as E6h and that with mixing time for 16 h in n-hexane was denoted as H16h. Then, the slurry using ethanol as a solvent was dried at 80 °C in an oven and the slurry using n-hexane was first kept at room temperature until most of n-hexane evaporated and then dried at 100 °C in the same oven. The dried powders were sieved through a 100 mesh screen.

3.2.3 Green Body Fabrication

Approximately 2.0 g of the thus obtained powder was formed into tablets of 20 mm in diameter and 5 mm in thickness by uniaxial pressing of 20 MPa followed by cold isostatic pressing (CIP, Dr. CIP, Kobelco Co., Ltd, Japan) of 200 MPa.

3.2.4 Sagger Structure and Sintering

Two tablets of each type were placed within a powder bed of coarse Si_3N_4 powder (SN-F2, particle size > 300 μm) of approximately 32 g in a high purity Al_2O_3 crucible (~ 40 mm inner diameter × ~ 36 mm height, Nikkato Co., Ltd., Japan). Then, the crucible was set in a larger Al_2O_3 crucible (~ 82 mm inner diameter × ~ 70 mm height) as shown in Fig. 3.2. Alumina coarse powder (A-11) of approximately 235 g was filled to the space between the two crucibles. To avoid the reaction of Si_3N_4 packing powder with the bottom of larger Al_2O_3 crucible, Al_2O_3 powder was also layered in the lower part of a small crucible. Sintering was performed in an air

atmosphere furnace at a temperature ranging between 1500 °C to 1700 °C for 2 h with a heating and cooling rate of 10 °C/min.
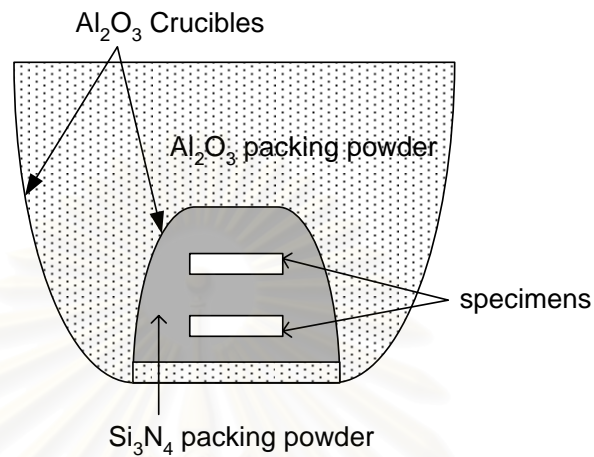
Fig. 3.2 Schematic of the crucible structure

3.2.5 Characterization

3.2.5.1 Particle size distribution and oxygen content

The particle size distributions of the powders before and after milling were measured by particle size analyzer (SA–CP2, Shimadzu, Japan). The oxygen contents of the raw Si_3N_4 powder and the powder mixtures were analyzed by an Oxygen/Nitrogen determinator (TC–436 DR, LECO, USA).

3.2.5.2 Mass loss and bulk density of sintered body

Mass losses (Δm) of the specimens were measured by using the following formula:

$$\Delta m = \frac{m_G - m_S}{m_G}.100 \qquad (3.1)$$

Where m_G = mass of the green body

$$m_S = \text{mass of the sintered body}$$

The bulk density of sintered body was measured by Archimedes' principle (water displacement):

$$\rho_S = \frac{\rho_S \cdot \rho_W}{m_S - m_W} \tag{3.2}$$

Where ρ_S = bulk density (g/cm^3)

ρ_W = density of water at room temperature ($\approx$ 1 g/cm^3)

m_S = mass of the sintered body in air (g)

m_W = mass of the sintered body in water (g)

The relative density (ρ_{rel}) was calculated by dividing the bulk density (ρ_S) by the theoretical density (ρ_{th}). The theoretical density was calculated based on the rule of mixture, i.e. the relative density was calculated based on the theoretical density of each individual constituent and its content.

3.2.5.3 Crystal phases

The crystal phases present in the sintered ceramics were identified by X–ray diffraction using Bruker difractometer model D8 advance (Ni-filtered Cu Kα radiation; λ = 1.5406 Å). The X-ray tube was operated at 40 kV and 40 mA. Diffractographs of the samples were recorded over the 2θ range from 10° up to 70° at a scanning rate of 2°/min.

Part II:

3.3 Modification of Attrition Mill

In Part I, we have used attrition mill consisting of pot, shaft and blades made of tetragonal ZrO_2 (see Fig 3.3). This is known as one of the most wear resistant hard materials. However, the ZrO_2 blade and container still have worn after long time usage (see Fig. 3.4). It can be an impurity for the Si_3N_4 powder mixtures. To avoid the contamination of inorganic impurities, ZrO_2 pot shaft and blades of attrition mill were replaced by polymeric materials. Prochazka *(89)* reported that an agitator blade made of ultrahigh molecular weight polyethylene and a jar lined with silicone rubber show good wear resistance when comminuting hard powder such as B_4C without contamination. The DYNO-MILL, which is a kind of agitation mill and can comminute ceramic powder under 100 nm in size *(90-91)*, also uses a polyurethane blade *(92)*. From the references 2 and 3, polyurethane and polyethylene are the candidate material for the wear parts. Polyethylene is reported only in a scientific paper. On the other hand, polyurethane is used for commercial products. So we selected polyurethane as the main material for our wear parts. The pot and blades were made of polyurethane (PU), and the shaft was made of MC nylon (see Fig. 3.5).
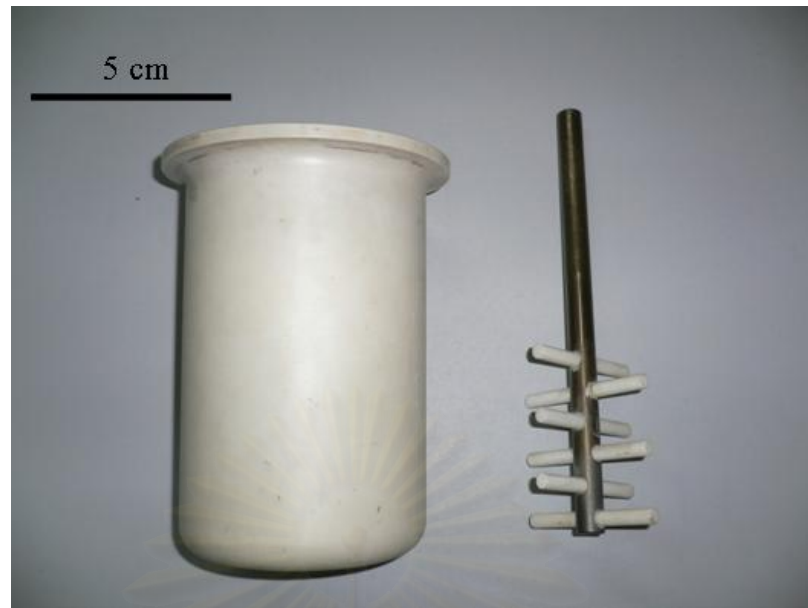
Fig 3.3 Original ZrO_2 pot and shaft of attrition mill
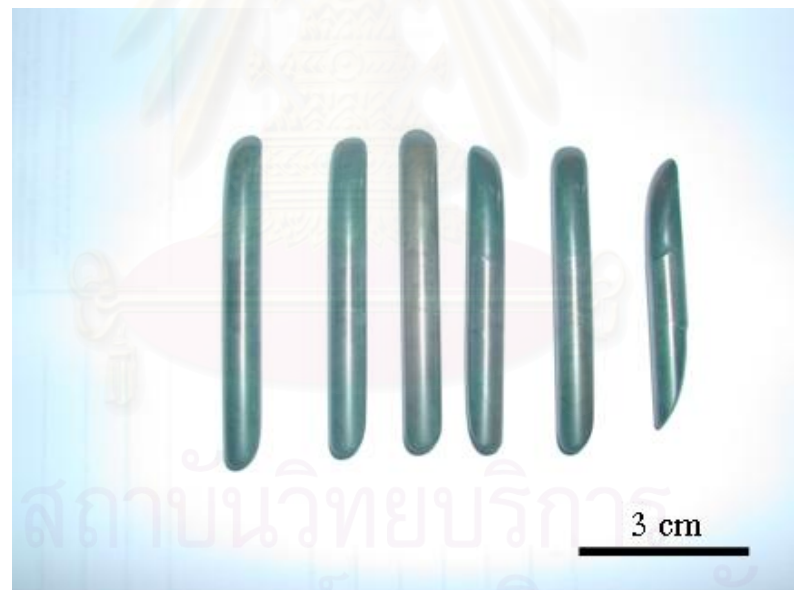
Fig. 3.4 Original ZrO_2 blade after 2 years usage

Fig. 3.5 MC nylon shaft, polyurethane blades and polyurethane container

After finishing installing the equipment, the grinding efficiency of the modified attrition mill was tested. Al_2O_3 powder (A-21 grade, Sumitomo Chemicals Co., Ltd., purity 99.7 wt%, particle size 2-4 micron) was comminuted by the original parts and the newly designed parts. The weight of Al_2O_3 powder, the size and weight of Al_2O_3 balls and the amount of water were 250 g, 3 mm and 1.20 kg and 300 cm^3, respectively. The attrition mill was operated at the speed of 500 rpm for 10 h. The particle size distribution curves measured by MASTERSIZER are shown in Fig. 3.6. The median particle sizes and specific surface areas of powder milled using original and new parts are 0.68 μm, 4.2 m^2/g and 0.65 μm and 4.4 m^2/g, respectively. The Al_2O_3 media balls loss 10 g in wear. The appearance of MC nylon parts, Polyurethane blades and Polyurethane container were no change. The weight of shaft and blade increased slightly due to the slurry adhered to its surface.
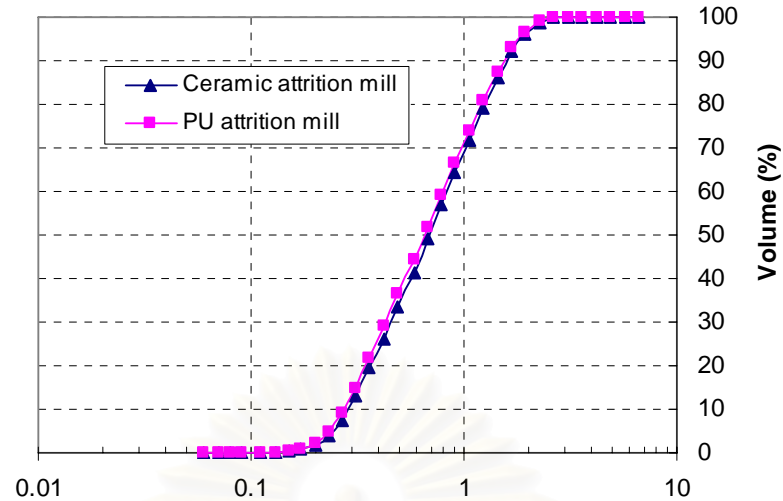
Fig. 3.6 Particle size distribution curves of Al_2O_3 powder milled 10 h by attrition mill with ceramic and PU attrition mill

From the result shown in Fig 3.6, polyurethane has been used as the material of blade and container for an attrition mill. The parts made of polyurethane do not break by mechanical accident and suffer almost no wear. The attrition mill with polyurethane parts comminutes Al_2O_3 powder to the same fineness with the original parts. Moreover, the price of the PU parts is very cheap compared with that of ceramic parts. Consequently, polyurethane is a suitable material for use as the wear parts of attrition mill. Therefore, we have used this equipment for grinding and mixing Si_3N_4 powder for the Part II experiment in order to avoid the contamination of impurities to the powder mixtures. Because the impurities in the sample is one of causes that lowering the mechanical properties.

3.4 Experiments on the Sintering of Si_3N_4 with MgO-Al_2O_3 System Additive

3.4.1 Powder and Green Body Preparation

At first, β-Si_3N_4 powder was ground by the attrition mill using the same method as described in 3.2.2. To reduce the oxygen content in the mixed powder, the milling time of this experiment was only 4 h and ethanol was used as the mixing medium. Then, the particle size distribution and oxygen content of the milled powder were analyzed by the same method as 3.2.5.1. After that, the mixing/milling of Si_3N_4 powder and additives was performed by mixing as-received β-Si_3N_4 powder with MgO and Al_2O_3 for 4 h. The compositions of the powder mixtures are shown in Table 3.6. The forming process of the green specimens was already described in 3.2.3.

Table 3.6 Compositions of Si_3N_4 powder mixed with various MgO and Al_2O_3 contents

Sample code	Composition (wt%)		
	β-Si_3N_4	MgO	Al_2O_3
M0.5A0.5	99	0.5	0.5
M1A1	98	1	1
M2A2	96	2	2
M3A3	94	3	3
M4A4	92	4	4
M5A5	90	5	5

3.4.2 Sintering

The green specimens were placed in a BN sagger. Then, the sagger containing specimens was placed in a larger graphite crucible. Sintering was done in a gas pressure furnace (HIGH MULTI-5000, Fujidempa Co., Ltd., Japan) with graphite heating elements at the temperature ranging from 1700 ºC to 1850 ºC for 2 h under a nitrogen pressure of 1.0 MPa with a flow rate of 2 l/min. The heating rate of all sintering temperatures was 10 ºC/min and the cooling rate was natural cooling. A schematic diagram of the sintering pattern is shown in Fig. 3.3.
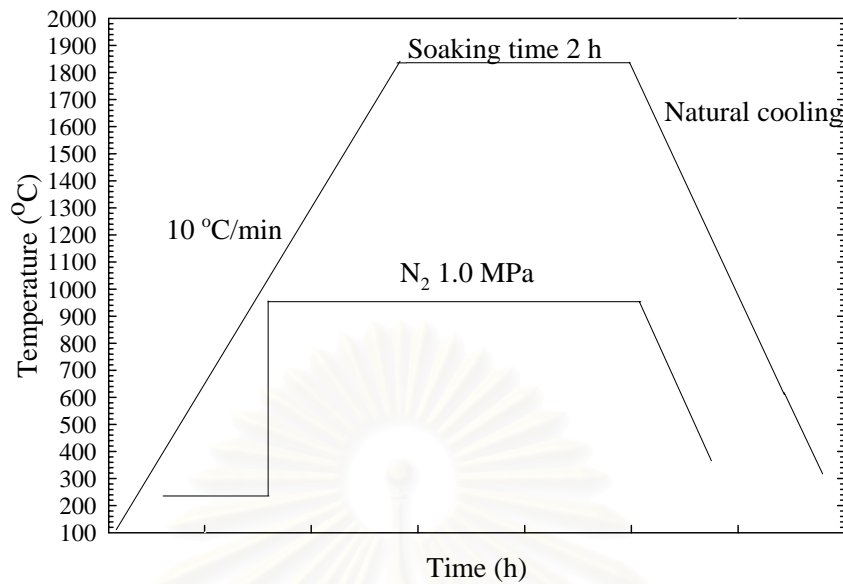
Fig. 3.3 Schematic diagram of sintering schedule

3.4.3 Characterization of the Sintered Ceramics

Mass loss and sintered density of the sintered materials were measured by using the method described in 3.2.5.2. The other characterizations in terms of morphology, Vickers hardness, room temperature fracture toughness and flexural strength were performed using the following methods.

3.4.3.1 Morphology and grain size

In order to observe the microstructure of the sintered ceramics, scanning electron microscope (SEM) was employed. SEM analyses were carried out on polished and plasma etched surfaces of samples using field-emission type scanning electron microscope (FE-SEM, S4800, Hitachi, Japan). For this purpose, the specimens were mirror polished by using 1 μm diamond paste and carbon coated in order to avoid charging effects. Average grain size was determined from secondary electron SEM images using the linear intercept length method *(93)*.

3.4.3.2 Vickers hardness and fracture toughness

The Vickers hardness and fracture toughness of the sintered specimens were measured by Vickers indentation method and calculated according to JIS-R1610 and JIS-R1607, respectively.

Test specimen was ground with 200 grit diamond wheel and then polished with 400, 800 and 1,200 grit SiC papers (Buehler grinding paper) and followed by 6, 3 and 1 μm diamond paste. After polishing, specimens were washed with ethanol in an ultrasonic bath to remove dirt and debris from the surfaces. Vickers indentation was applied at a load of 98.07 N (10 kgf) using microhardness tester (Zwick 3212, Zwick GmbH & Co.). Vickers hardness and fracture toughness were calculated using the following formulae:

$$Hv = 1.854\left(\frac{F}{d^2}\right) \qquad (3.3)$$

Where Hv = Vickers hardness

F = test load (N)

d = average length of diagonal lines of indent (mm)

$$K_{IC} = 0.018\left(\frac{E}{Hv}\right)^{1/2}\left(\frac{P}{C^{3/2}}\right) \qquad (3.4)$$

Where K_{IC} = fracture toughness value (MPa m$^{1/2}$)

E = Young's modulus (Pa)

Hv = Vickers hardness

P = test load (N)

C = crack length (mm)

3.4.3.3 Flexural strength

Selected specimens were cut to a dimension of $3 \times 4 \times 40$ mm^3 and then polished by SiC powder on the glass plate with sequence of powder particle size of 2000, 4000 and 8000 mesh. Then, the bending strength of the polished specimens was measured by 3-point bending method in conformity with JIS R1601 using universal testing machine (Instron 5844, USA).

3.5 Experiments on the Effect of Y_2O_3-Al_2O_3 Additives on the Mechanical Properties of Si_3N_4 Ceramics

3.5.1 Preparation of the Specimens

To compare the mechanical properties of sintered Si_3N_4 using low-cost additives (MgO-Al_2O_3) with higher cost of additives, Y_2O_3-Al_2O_3 system was used as additives. The processing of powder preparation was the same as 3.3.1. The compositions of mixed powder are shown in Table 3.7. Sintering was performed by following the method explained in 3.3.2.

Table 3.7 Compositions of mixed Si_3N_4 powder with various Y_2O_3 and Al_2O_3 contents

Sample code	Composition (wt%)		
	β-Si_3N_4	Y_2O_3	Al_2O_3
Y2A2	96	2	2
Y3A3	94	3	3
Y4A4	92	4	4
Y5A3	92	5	3
(a)Y5A3*	92	5	3

* α-Si_3N_4 powder (Ube industries Co., Ltd., E-10 grade, >94% α phase) was used.

3.5.2 Properties Characterization

The properties such as bulk density, mechanical properties and microstructure were characterized by the same method described in 3.3.

3.6 Wear Properties of the Sintered Ceramics

In the wear test experiment, M2A2, Y5A3 and (a)Y5A3 sintered at 1850 °C for 2 h under a N_2 gas pressure of 1.0 MPa were selected to compare the wear properties of the sintered materials. The selected samples were cut into a plate of dimension $25 \times 55 \times 5$ mm^3, and polished to surface roughness of Ra = 0.005 μm. Unlubricated ball-on-flat experiments were carried out against a commercial Si_3N_4 ball (TOSHIBA Co., Ltd.) with diameter of 5 mm. Wear test conditions were as follows: sliding speed = 0.10 m s^{-1}; normal load = 25 N; test duration = 1000 s; atmosphere = air; temperature = 22-25 °C; relative humidity during testing = 40-60 %RH. Specific wear rate were calculated from weight losses according to the method of JIS R1613. The equation is as follows:

$$w = \frac{(w_a - w_b)}{(P.L.\rho)} \qquad (3.5)$$

Where w = specific wear rate (m^2/N)

w_a = weight before testing (Kg)

w_b = weight after testing (Kg)

P = Load (N)

L = sliding distance (m)

ρ = density of specimen (Kg/m^3)

3.7 Experiments on the Development of Microstructure of Si_3N_4 Prepared from Mixed β- and α-Powders

3.7.1 Background of the Experiment

It is well known that the microstructure of Si_3N_4 ceramics containing high aspect ratio grains strongly affects to the mechanical properties of them. In the previous report, we have tried to develop the high aspect ratio microstructure of Si_3N_4 using β-powder by prolonging the length of soaking time; however, the microstructure was not as good as we expected. Therefore, we have tried to study the development of the high aspect ratio microstructures by adding α type powder to β-powder (SN-F2) expecting that $α-Si_3N_4$ powder can promote the grains with high aspect ratio (rod-like shape). In this experiment, we studied the effect of α-phase content on the development of the microstructures of Si_3N_4 ceramics using MgO and Al_2O_3 as sintering additives. SN-7 grade Si_3N_4 powder was used as α phase source because it was cheaper than the other α type powders like commercial E-10 grade.

3.7.2 Specimens Preparation and Characterization

Si_3N_4 powder (SN-7 grade, Denka Kagaku Kogyo Co., Ltd., Japan) was used as α phase source. It consists of ~74 wt% α phase and 1.6 wt% oxygen content. The average particle size (D_{50}) was 1.5 μm. SN-7 powder was added to β type powder (SN-F2 grade, Kagaku Kogyo Co., Ltd., Japan) with varying amount of 10, 25, 50 and 100 wt%. Each composition was mixed with 2 wt% MgO and 2 wt% Al_2O_3 by attrition mill for 4 h using Si_3N_4 ball and ethanol as grinding media and liquid medium, respectively. To know the effect of additive content on the microstructures, 4 wt% MgO and 4 wt% Al_2O_3 were added to the mixture containing 50 wt% SN-7 powder. The compositions and α/(α+β) ratio are shown in Table 3.8.

The specimen preparation processes was the same as 3.3.1 and 3.3.2. The specimens were sintered at 1700, 1750, 1800 and 1850 °C for 2 h under N_2 gas pressure of 1.0 MPa. For the characterizations of sintered materials, mass loss and bulk density were measured. The fracture surface of sintered specimens was observed by SEM.

Table 3.8 Compositions and calculated $\alpha/(\alpha+\beta)$ ratio of the powder mixtures

Samples	Si_3N_4 powders (wt%)		Additives (wt%)		$\alpha/(\alpha+\beta)$
	SN-F2	SN-7	MgO	Al_2O_3	
10SN7M2A2	86.4	9.6	2	2	0.07
25SN7M2A2	72	24	2	2	0.19
50SN7M2A2	48	48	2	2	0.37
100SN7M2A2	-	96	2	2	0.74
50SN7M4A4	46	46	4	4	0.37

CHAPTER IV

RESULTS AND DISCUSSION

Part I:

4.1 Gas/Solid Reaction during Sintering Si_3N_4 in Air Atmosphere

4.1.1 Properties of Mixed Powder after Milling

The particle size distributions of the raw Si_3N_4 powder and the powders after milling are shown in Fig. 4.1. The attrition mill could reduce the particle size of the powder down to sub-micrometer size and the median (D_{50}) particle size of the powders after milling and mixing for 6 h (E6h) and 16 h (H16h) were 0.8 μm and 0.5 μm, respectively.
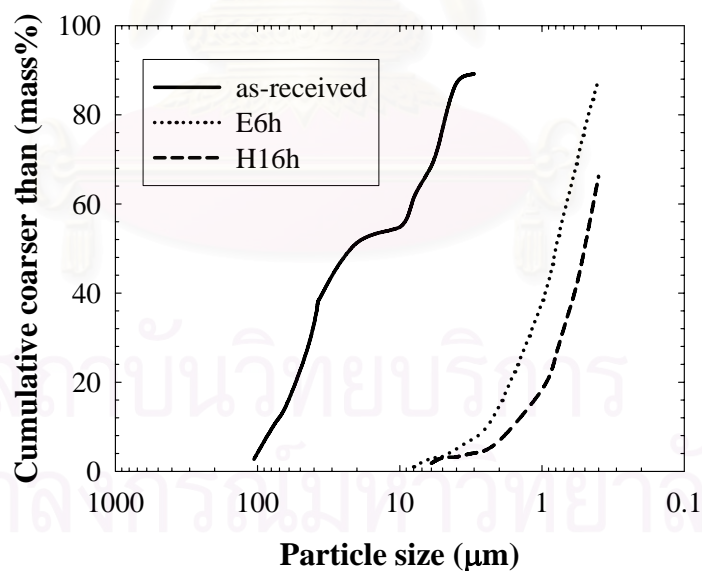
Fig. 4.1 Particle size distribution of as-received SN-F2 and powders after milling by attrition mill

The oxygen contents in these powders are shown in Fig. 4.2. The values in Fig. 4.2 did not include oxygen from the oxide additives. From the results, the oxygen content increased with increasing milling time because the fractured Si_3N_4 surfaces reacted with OH^- generated from ethanol by mechanochemical reaction to form Si–O bond *(94)*. N-hexane was used with attention to avoid oxygen increase during mixing, because n-hexane does not include OH^- in the molecule. Normally, the mixed powder using n-hexane as a medium should be dried in a vacuum rotary evaporator in order to avoid the oxidation of the Si_3N_4 powder. However, due to limited facility the slurry was dried in air as mentioned in 3.2.2. Unexpectedly, the oxygen content in the powder increased more than that in the mixture using ethanol. It was supposed that the active Si_3N_4 surface might adsorb and react with moisture during drying in air and in oven to form Si–O bond on the surface of Si_3N_4 powder.
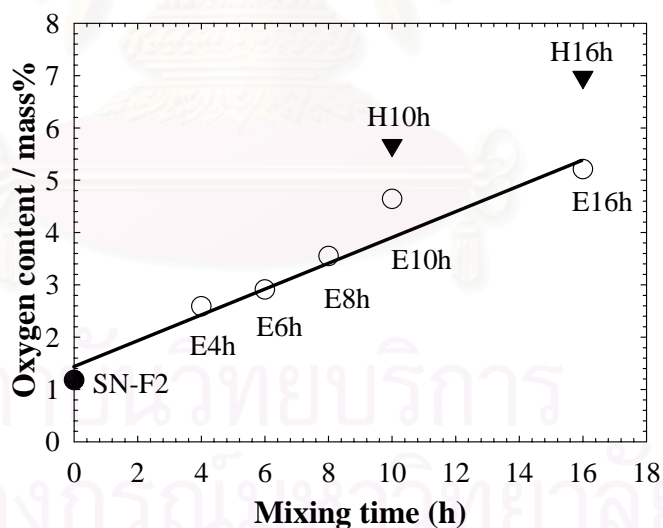
Fig. 4.2 Increment of oxygen content during milling as a function of milling time

4.1.2 Mass Loss

The average mass loss of two specimens, top and bottom shown in Fig. 4.3, as a function of the oxygen content in the mixed powders is shown in Fig. 4.4. The mass loss significantly increased with the oxygen content in the sintered specimen. It was easily understood by comparing Fig. 4.4 with Fig. 4.5.
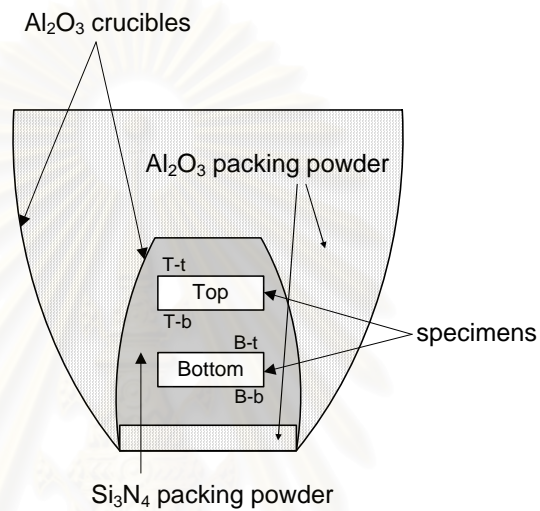
Fig. 4.3 Schematic of the crucible structure and specimen position
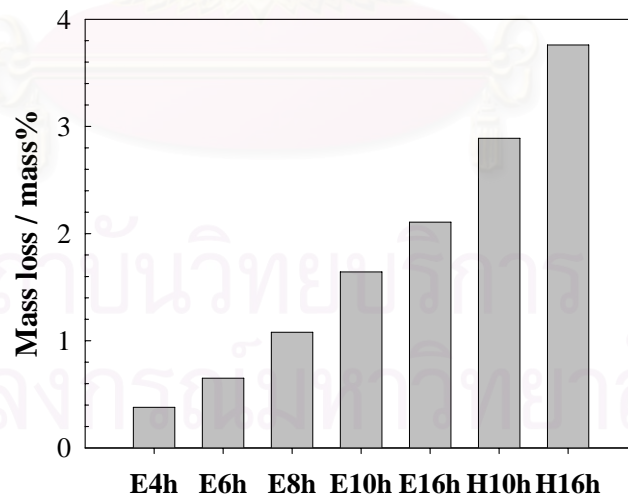
Fig. 4.4 Mass loss of sintered Si_3N_4 at 1700 °C for 2 h in air atmosphere as a function of oxygen content in the mixed powders

From this viewpoint, it was thought that the mechanism was similar to that of sintering in N_2 atmosphere, where Si_3N_4 powder reacts with SiO_2 and formed SiO (g). The main reaction leading to mass loss of specimen during sintering is equated as reaction (4.1) *(95-98)*.

$$Si_3N_4 (s) + 3SiO_2 (s,l) \rightarrow 6SiO (g) + 2N_2 (g) \qquad (4.1)$$
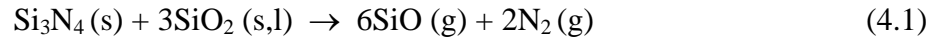
Figure 4.5 shows the average mass loss of E6h and H16h as a function of sintering temperature. The mass losses did not significantly change with the sintering temperature, unlike the mass loss of Si_3N_4 ceramics sintered in N_2 atmosphere which increased with increasing the sintering temperature *(95-97)*.
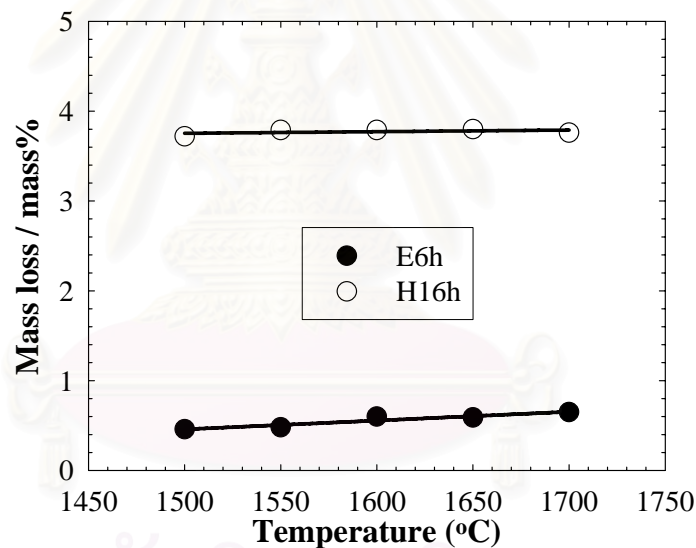
Fig. 4.5 Mass loss of sintered Si_3N_4 (E6h and H16h) as a function of sintering temperatures

Figure 4.6(a) shows the mass loss of each specimen of E6h, top and bottom, as a function of sintering temperature. The mass loss of the top specimen in the crucible was higher than that of the bottom one. The tendency was the same for H16h specimens (Fig. 4.6(b)). It was suggested that the atmosphere or gas partial

pressure at the top and the bottom positions of the crucible is different. Moreover, the mass loss did not increase as much with prolonged soaking time.
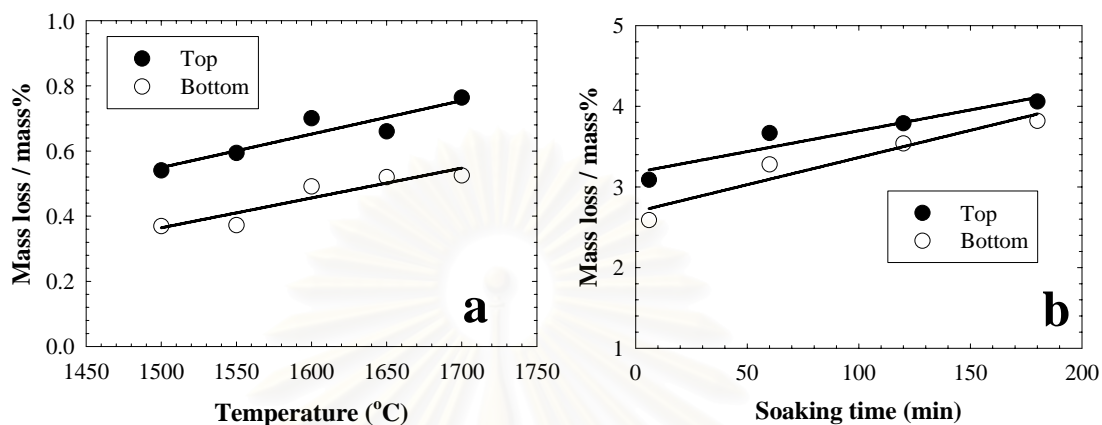
Fig. 4.6 Mass loss of top and bottom specimens (E6h) as a function of sintering temperature; (a), and mass loss of top and bottom specimens (H16h) sintered at 1650 °C as a function of soaking time; (b)

4.1.3 Reaction Taking Place in Packing Powder

After sintering at 1700 °C, the Al_2O_3 packing powder at the bottom of the crucible was hardened and became a solid slab as shown in Fig. 4.7. The slab was approximately 3 mm thick and rather difficult to crush. However, the solid slab was softer and easy to be taken out from the crucible when the sintering temperature was lower.
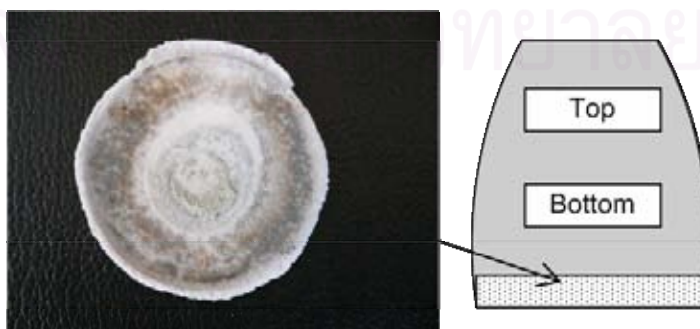
Fig. 4.7 Reacted Al_2O_3 packing powder (bottom side) after sintering at 1700 °C for 2 h in air atmosphere furnace

The XRD profile of the slab is shown in Fig.4.8. The packing powder, which was originally Al_2O_3, changed to the mixture of corundum (Al_2O_3), mullite ($3Al_2O_3.2SiO_2$) and a small amount of amorphous phase as shown in Fig.4.8. The mullite might be formed by the reaction between Al_2O_3 packing powder, SiO (g) generated from reaction (4.1) and/or (4.2) and O_2 (g) as shown in equation (4.3).

$$2Si_3N_4 \text{ (s)} + 3O_2 \text{ (g)} \rightarrow 6SiO \text{ (g)} + 4N_2 \text{ (g)} \tag{4.2}$$

$$3Al_2O_3 \text{ (s)} + 2SiO \text{ (g)} + O_2 \text{ (g)} \rightarrow 3Al_2O_3.2SiO_2 \text{ (s)} \tag{4.3}$$
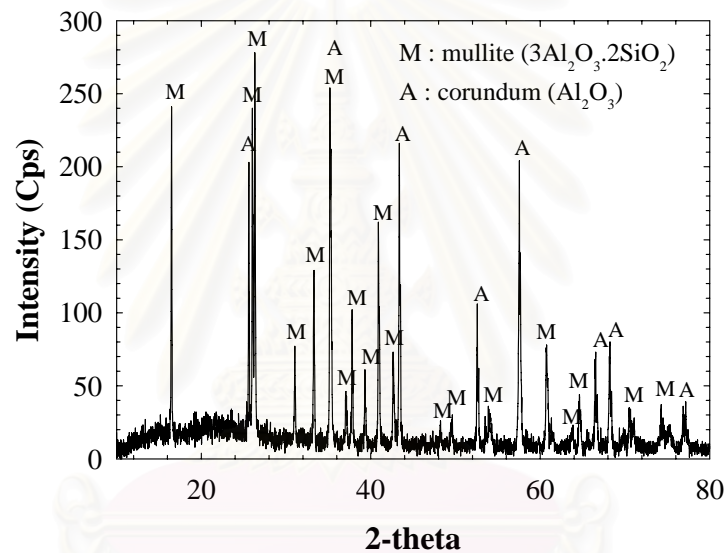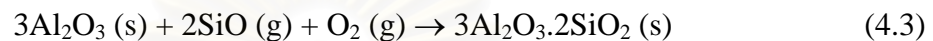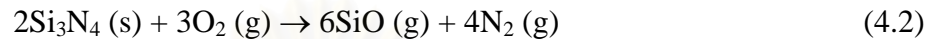
Fig. 4.8 XRD pattern of the reacted Al_2O_3 packing powder (bottom side) after sintering at 1700 °C for 2 h in air furnace

Amorphous phase was observed not only in the slab, but also on the edge of the small Al_2O_3 crucible. We did not analyze it, but the glassy film on the edge of the crucible might be SiO_2. We supposed that it was formed by the reaction of SiO (g) and atmospheric O_2 (g) diffused through Al_2O_3 packing powder.

Moreover, at the interface between Si_3N_4 and Al_2O_3 packing powders, a hardened layer of Si_3N_4 was formed with 1-2 mm in thickness and was easily separated from the packing powder above it. The XRD pattern of this material is

shown in Fig. 4.9. As seen in the XRD profile, small amounts of cristobalite (SiO_2) and Si_2N_2O were observed in this layer. The formation reactions of Si_2N_2O and SiO_2 are discussed in section 4.1.7.
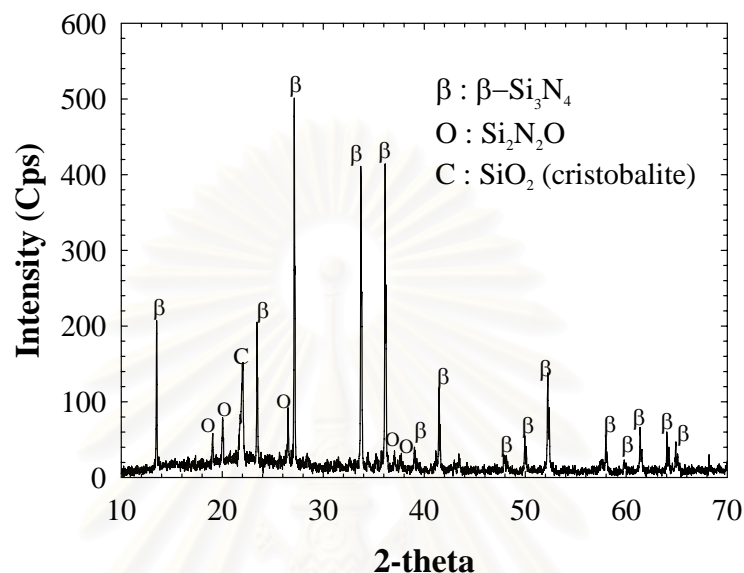
Fig. 4.9 XRD pattern of the reacted Si_3N_4 packing powder layer after sintering at 1700 °C for 2 h

4.1.4 Crystal Phase of Specimens

To corroborate the reactions suggested in this work, the crystal phases of the sintered specimens and packing powder were identified by X-ray diffractometer. The XRD pattern of E6h specimen surface after sintering is shown in Fig. 4.10.

The result indicated that the top surface of the specimen at the top position (T-t, see Fig. 4.3) consisted of only β-Si_3N_4 phase. On the contrary, the bottom surface of the specimen at the bottom position (B-b, see Fig. 4.3) consisted of only silicon oxynitride (Si_2N_2O). The surfaces T-b and B-t in Fig. 4.3 were composed of mixed phases of β-Si_3N_4 and Si_2N_2O. To find out the depth of Si_2N_2O, the B-b surface was ground steply and then characterized by XRD.
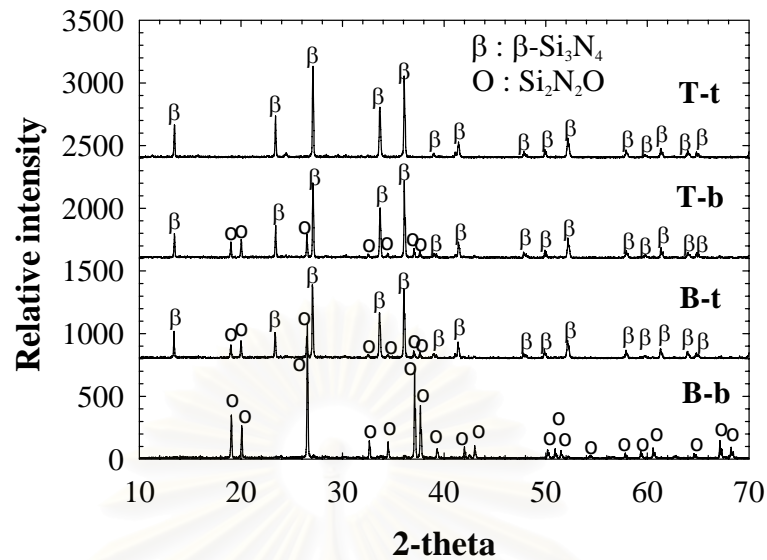
Fig. 4.10 XRD patterns of E6h specimen surfaces after sintering at 1700 °C for 2 h in air atmosphere furnace

The XRD patterns of specimen before and after grinding are shown in Fig. 4.11. At the depth of 47 μm, only Si_2N_2O was observed. After grinding out 75 μm, Si_2N_2O peaks reduced and β-Si_3N_4 appeared.
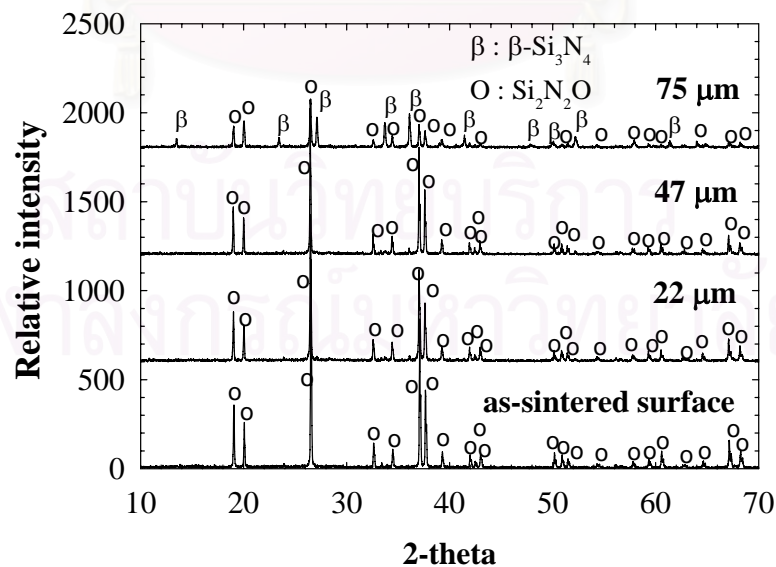
Fig. 4.11 XRD patterns of the specimen surface of E6h before and after grinding the bottom surface of the bottom specimen (B-b) sintered at 1700 °C for 2 h

The effect of sintering temperature on the formation of Si_2N_2O in the specimen surfaces (B-b) was indicated by XRD patterns as shown in Fig. 4.12 (a). β-Si_3N_4 peaks were observed at the sintering temperature of 1500 °C, their intensity gradually reduced at 1600 °C and disappeared at 1700 °C while those of Si_2N_2O clearly increased with the sintering temperature. The formation of Si_2N_2O was also favored by prolonged soaking time as indicated in Fig. 4.12 (b), whereas β-Si_3N_4 was observed only at the shortest soaking time of 6 min, but not at 1 h and 3 h. The formation of Si_2N_2O in the surface of specimens is further discussed in section 4.1.7.
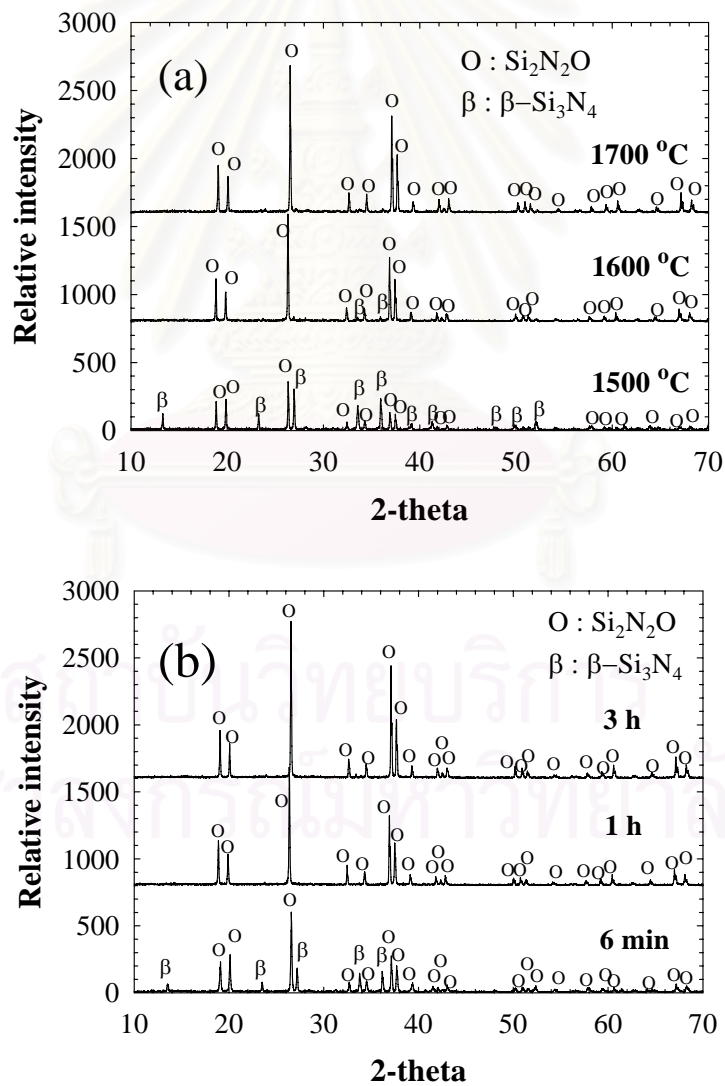
Fig. 4.12 XRD patterns of specimen surface (B-b) of (a) E6h sintered at 1500 °C to 1700 °C for 2 h and (b) H16h sintered at 1650 °C for various soaking times

4.1.5 Mass Loss Reaction

Materials in the small crucible are specimens of Si_3N_4 with glassy phase, Al_2O_3 packing powder, Si_3N_4 packing powder, nitrogen gas and oxygen gas. The glassy phase is composed of SiO_2, MgO and Al_2O_3. Therefore, the major mass change reactions of specimens should be through the gas/solid reactions between materials mentioned via reaction (4.1) and (4.2).

As shown in Fig. 4.4 and 4.5, the average mass loss of specimens was qualitatively proportional to the content of oxygen in the specimens. Consequently, the major mass loss reaction had to be reaction (4.1), nevertheless, the equilibrium P_{SiO} of reaction (4.2) is higher than that of reaction (4.1) when P_{O_2} is higher than $\sim 10^{-10}$ Pa as shown in Fig. 4.13(a).

Another mass loss reaction of the specimens may probably be the volatilization of MgO, which was used as sintering aid. MgO is well known to be highly volatile when used for preparing Si_3N_4 ceramics. It can vaporize to Mg (g) and O_2 (g) and/or MgO (g) at high temperature. However, we did not analyze the final content of $Mg(O)$ in the sintered specimens in this experiment.
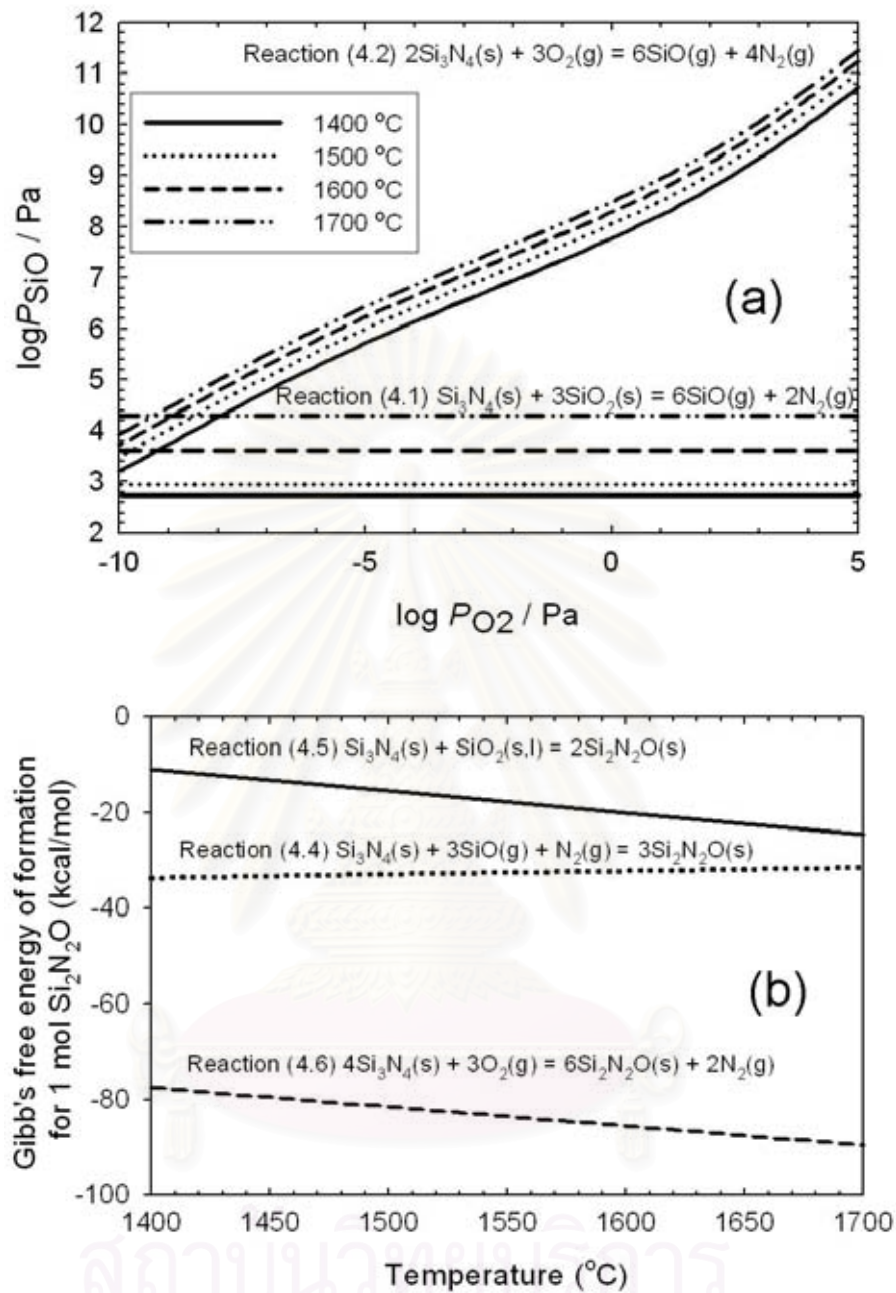
Fig. 4.13 (a) Equilibrium SiO (g) pressure for the reactions (1) and (2) as a function of equilibrium oxygen pressure from 1400 °C to 1700 °C and (b) Gibbs free energy of the formation of Si_2N_2O of the reactions (4), (5), and (6) from 1400 °C to 1700 °C

4.1.6 Amount of Mass Loss as a Function of Sintering Temperature and Soaking Time

Though the P_{SiO} of reaction (1) was independent on an oxygen partial pressure in atmosphere, it increased from 10^3 Pa at 1500 °C to 4.4×10^4 Pa at 1700 °C as shown in Fig. 4.13(a). Therefore, it was reasonable to assume that the mass loss should increase with increasing temperature. However, as shown in Fig. 4.5 and 4.6, the mass loss did not change so much with sintering temperature and soaking time. The independence of the mass loss on the sintering temperature and soaking time may be due to the formation of impermeable layer.

As shown in Fig. 4.7 and 4.8, Al_2O_3 packing powder in the bottom of the small Al_2O_3 crucible partially changed to mullite and SiO_2 glass layer after sintering. As explained in 4.1.3, Si_3N_4 packing powder layer adjoined to Al_2O_3 packing powder changed to Si_3N_4, Si_2N_2O and SiO_2 glass (cristobalite at room temperature) layer after sintering. This layer might soon become less permeable. The amount of gas diffused through the layer would be proportional to the total amount of SiO (g) evaporated from the reaction (4.1) and (4.2). In other words, when sintering temperature was high, the layer became impermeable in a shorter time but in a longer time at low sintering temperature. When the SiO (g) and O_2 generated from outside nearly stopped to diffuse out and in, the reaction would almost stop. As a result, mass loss was not affected by sintering temperature and soaking time by the formation of impermeable layer.

4.1.7 Formation of Si_2N_2O

Si_2N_2O was observed in the surface of specimens and in the Si_3N_4 packing powder adjoined to Al_2O_3 packing powder. The formation of Si_2N_2O is only observed via a presence of liquid phase whereby the liquid phase is generally

provided by the intentionally added metal oxides. The facts had already been reported by Huang et al. *(99)*, Mitomo et al. *(100)*, Ohashi et al. *(101-104)*, Lewis et al. *(105)*, Li et al. *(106)*, Wang et al. *(107)*, and Larker *(108)*.

Possible material balances to form Si_2N_2O are suggested as follows:

$$Si_3N_4 \text{ (s)} + 3SiO \text{ (g)} + N_2 \text{ (g)} \rightarrow 3Si_2N_2O \text{ (s)} \tag{4.4}$$

$$Si_3N_4 \text{ (s)} + SiO_2 \text{ (s,l)} \rightarrow 2Si_2N_2O \text{ (s)} \tag{4.5}$$

$$4Si_3N_4 \text{ (s)} + 3O_2 \text{ (g)} \rightarrow 6Si_2N_2O \text{ (s)} + 2N_2 \text{ (g)} \tag{4.6}$$
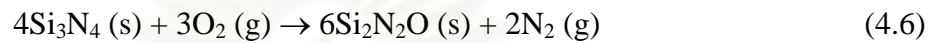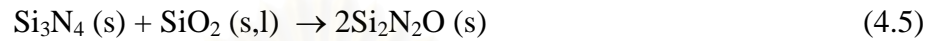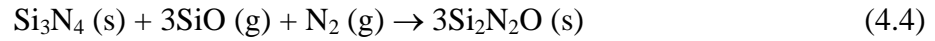
Considering the Gibbs free energies of the reaction (4.4), (4.5) and (4.6) shown in Fig. 4.13(b), the formations of Si_2N_2O via reaction (4.5) and (4.6) are more thermodynamically favorable than reaction (4.4).

As discussed in 4.1.4, more amount of Si_2N_2O in sintered specimens was observed in the surface closer to the bottom side and was also in the outer surface. Therefore, the material to form Si_2N_2O in the specimen was supplied from outside of the specimen. Oxygen gas diffuses in the small Al_2O_3 crucible from outside. Then the amount of O_2 (g) was rich; in other words, oxygen partial pressure (Po_2) was higher in the bottom side. Considering all facts mentioned above, the formation reaction of Si_2N_2O in the specimen might be the reaction (4.6).

Another possible reaction is the reaction (4.5), because SiO_2(s,l) generated by the reaction (4.7) and (4.8). In these reactions, Po_2 affects the amount of SiO_2(s,l) generation.

$$2SiO \text{ (g)} + O_2 \text{ (g)} \rightarrow 2SiO_2 \text{ (s,l)} \tag{4.7}$$

$$Si_3N_4 \text{ (s)} + 3O_2 \text{ (g)} \rightarrow 3SiO_2 \text{ (s,l)} + 2N_2 \text{ (g)} \tag{4.8}$$
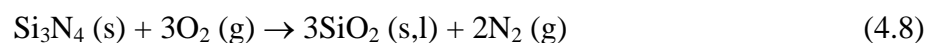
The SiO_2 in reaction (4.7) is formed by reaction between SiO (g) which generates from reaction (4.1) and/or (4.2) and O_2 (g) diffused from the atmosphere.

The SiO_2 in reaction (4.8) is resulted from the passive oxidation of Si_3N_4. Generally, the reaction between Si_3N_4 (s) and O_2 (g) is passive oxidation when oxygen partial pressure (Po_2) is high and it changes to active oxidation (reaction (4.2)) when $Po_{2\ (g)}$ becomes lower. The transition condition of passive to active is affected by the atmosphere temperature and gas flowing rate *(109)*. However, the transition occurred at about 10^2 Pa *(96,109)*.

The Po_2 in the crucible could not be measured. Therefore, we do not know whether Po_2 was higher than 10^2 Pa or not in the area of specimens. As a result, it is not confident that the reaction (4.5) is the only one of the formation reactions of Si_2N_2O in the surface of specimens, but there will be some possibility.

In the layer of Si_3N_4 packing powder adjoined to Al_2O_3 packing powder, Po_2 is presumed to be high. As a result, reaction (4.6), (4.7) and (4.8) occur. The SiO_2 (s,l) in reaction (4.7) and (4.8) provide a viscous glass phase for reaction (4.5) to generate Si_2N_2O. The glassy phase may also be formed by the reaction between SiO_2 and Al_2O_3 powder adjoined to Si_3N_4 packing powder. This liquid formation is strongly influenced by Al_2O_3 which decreases the melting temperature by forming an aluminium silicate melt. It enhances dissolution of Si_3N_4 and in this way promotes the formation of Si_2N_2O solid solution *(99)*.

No Si_2N_2O was generated in T-t surface and much amount of mass loss was observed because Po_2 was too low to precipitate SiO_2 (s,l) by reactions (4.7) and (4.8) to react with Si_3N_4. Hence, reaction (4.5) and/or (4.6) could not occur. Accordingly, the Si_3N_4 packing powder in the top part of the small sagger was easily crushed to powder and it did not include any other phase except Si_3N_4.

Plucknett and Lin sintered Si_3N_4 in air atmosphere. They observed only mass gain and generation of Si_2N_2O at the sintering temperature of 1500 – 1750 °C.

(14) Comparing with our results, the Po_2 around the specimen might be higher than that of this experiment.

4.1.8 Mass Loss Difference between Top and Bottom Specimens

As shown in Fig. 5 and 6, mass loss of the top specimen was much higher than that of bottom one. The reaction (4.1) is the mass loss reaction. The reaction (4.5) and (4.6) are the mass gain reaction.

The difference in the mass loss of the top and bottom specimen is sum of the mass loss and mass gain reactions. And the mass gain reaction is affected by the Po_2 in the crucible as discussed in 4.1.7. However, the sequence of mass loss and mass gain reactions with soaking time is not explained exactly in this experiment.

4.1.9 Mass Loss Difference between Sintering in Air and in N_2 Atmospheres

The mass change of the specimens sintered both in air and N_2 atmospheres is shown in Fig. 4.14. It is clearly indicated that the trends of mass loss with increasing temperature are different between N_2 and air atmospheres. In the case of sintering in N_2 furnace, mass loss strongly increased with increasing the sintering temperature. The mass loss of Si_3N_4 specimen during sintering under N_2 atmosphere is thought to be originated from the reaction of $Si_3N_4(s)$ with $SiO_2(l)$ as in reaction (4.1) *(37,59,98)*. This finding conforms to the thermodynamic calculation that the value of P_{SiO} increases with the increasing temperature at constant P_{N2}, hence, the mass loss rises at high temperature *(59,110)*.
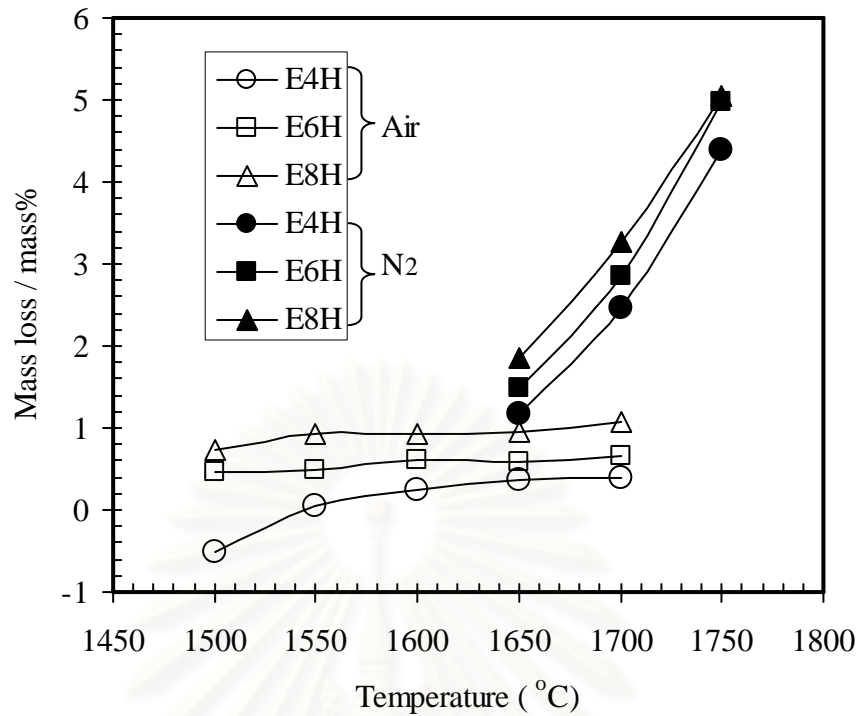
Fig. 4.14 Mass losses of Si_3N_4 ceramics sintered in air and in N_2 atmosphere furnaces

In the case of sintering in air atmosphere, it was found that the mass losses did not change so much with sintering temperature. On the contrary, the mass loss significantly increased with the O_2 or SiO_2 contents in the composition before sintering. Hence, the longer the milling time was, the higher the mass loss. The mass loss behavior of Si_3N_4 ceramic during sintering in air atmosphere was affected by the formation of the impermeable layer.

Part II:

4.2 Sintering of Si_3N_4 with MgO-Al_2O_3 Additives

4.2.1 Particle Size Distribution and Oxygen Content of Si_3N_4 Powder Ground by Modified Attrition Mill

The analyzed oxygen content of milled Si_3N_4 powder was 2.21 wt%. The oxygen content increased from 1.18 wt% to 2.21 wt% due to the mechanochemical reaction of Si_3N_4 with ethanol *(94)*. The median particle size (D_{50}) of milled powder was 0.45 μm and the particle size distribution curve is shown in Fig.4.15. The curve showed that the distribution of particle size was bimodal distribution consisting of larger fraction of fine particles (< 1 μm) and smaller fraction of large particles (> 1 μm).
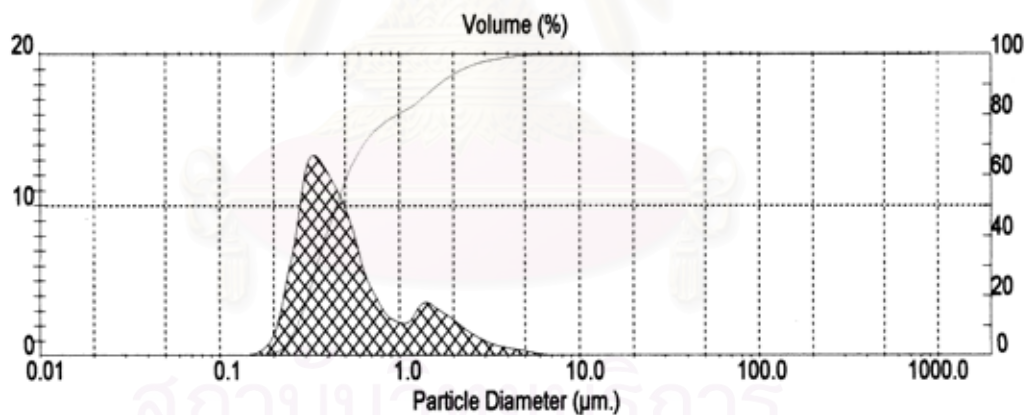
Fig. 4.15 Particle size distribution curve of milled Si_3N_4 powder by attrition mill for 4 h

4.2.2 Mass Loss

Mass loss of sintered specimens increased as a function of sintering temperature, as seen in Fig. 4.16. The increment tendency of the mass loss with temperature was the same with that reported before *(111)*. The main mass loss

reaction of Si_3N_4 came from the reaction of surface silica (SiO_2) with Si_3N_4 (reaction 4.1). In the case of very low additive content (M0.5A0.5 and M1A1), the specimens showed higher mass loss values. The reason for this might be due to much amount of porosity in these specimens as seen in Fig. 4.18. Therefore, the vaporization or diffusion of gases during sintering was easier than those of the lower porosity (higher density) ones. With prolonged soaking time, mass loss of the specimens increased as a function of soaking time as well. The effect of the length of soaking time on the mass loss of the specimens is shown in Fig. 4.17.
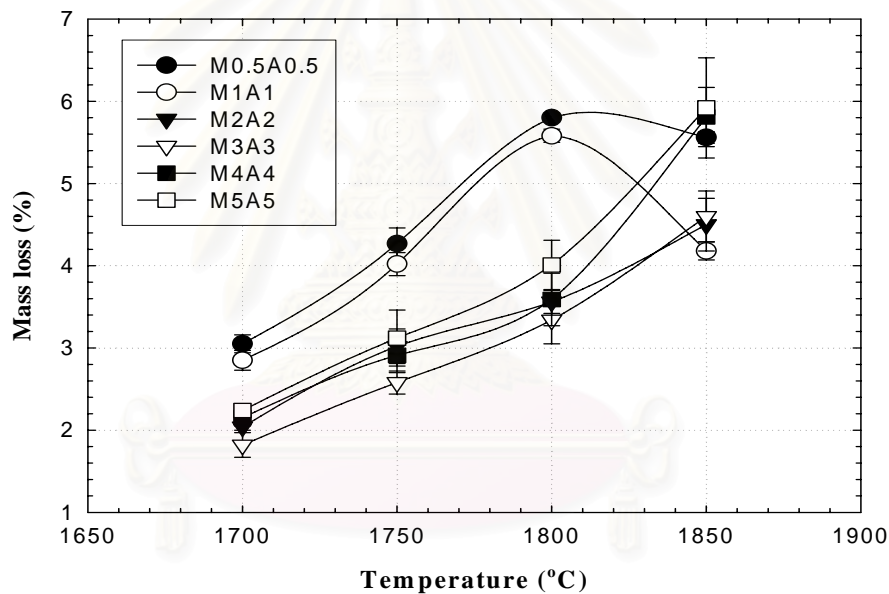
Fig. 4.16 Mass loss of sintered specimens with various contents of mixed additives at 1700 °C to 1850 °C for 2 h under N_2 gas pressure of 1.0 MPa
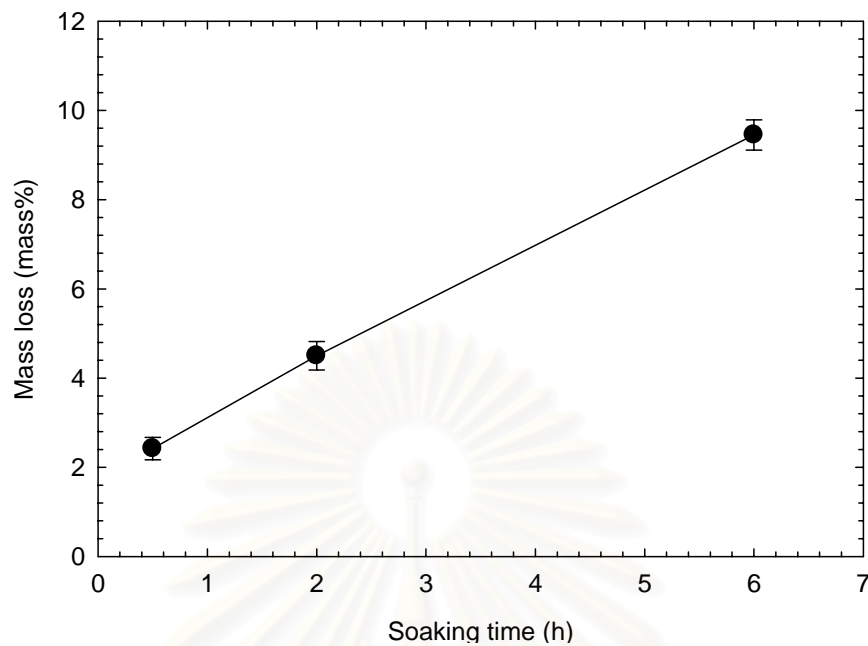
Fig. 4.17 Mass loss of specimens (M2A2) sintered at 1850 °C as a function of soaking time

4.2.3 Bulk and Relative Densities

Bulk and relative densities of the sintered specimens are shown in Fig. 4.18 and Fig. 4.19, respectively. Densities of sintered specimens with effective additive content (M2A2 to M4A4) increased with increasing temperature up to 1850 °C, but in the case of high additive content, M5A5, the density decreased with increasing temperature due to the bloating of specimens (see Fig. 4.20). In the condition of low additive content (M0.5A.5 and M1A1), the density was relatively low even at the maximum sintering temperature of 1850 °C. It was thought that the essential liquid phase for sintering was not enough to densify the materials to full density. The highest density of about 99 % of theoretical density was achieved for M2A2 at the sintering temperatures of 1800 – 1850 °C.
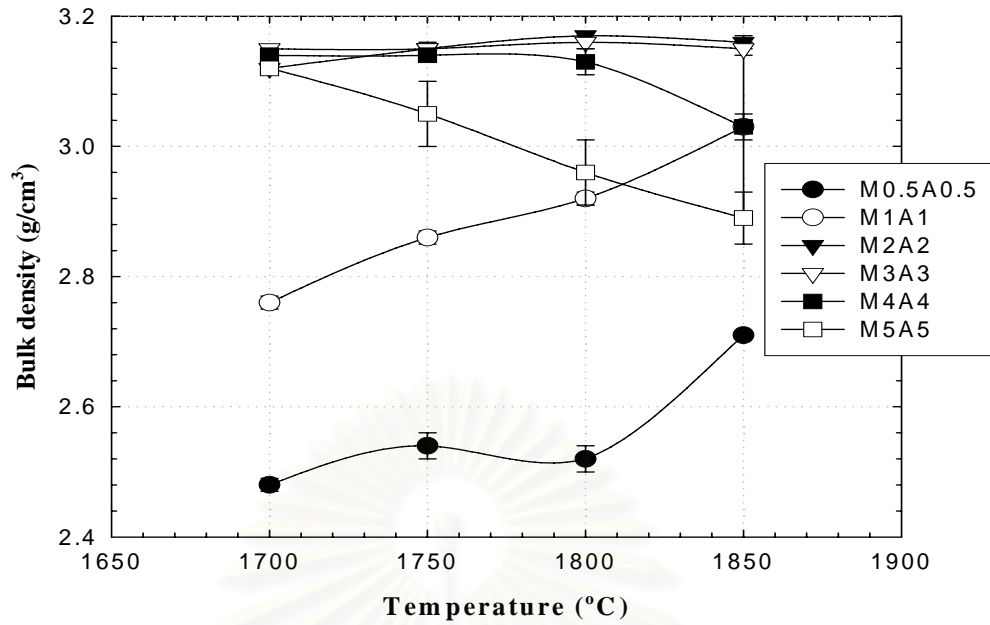
Fig. 4.18 Bulk density of sintered specimens with various contents of additives at 1700 °C to 1850 °C for 2 h under N_2 gas pressure of 1.0 MPa
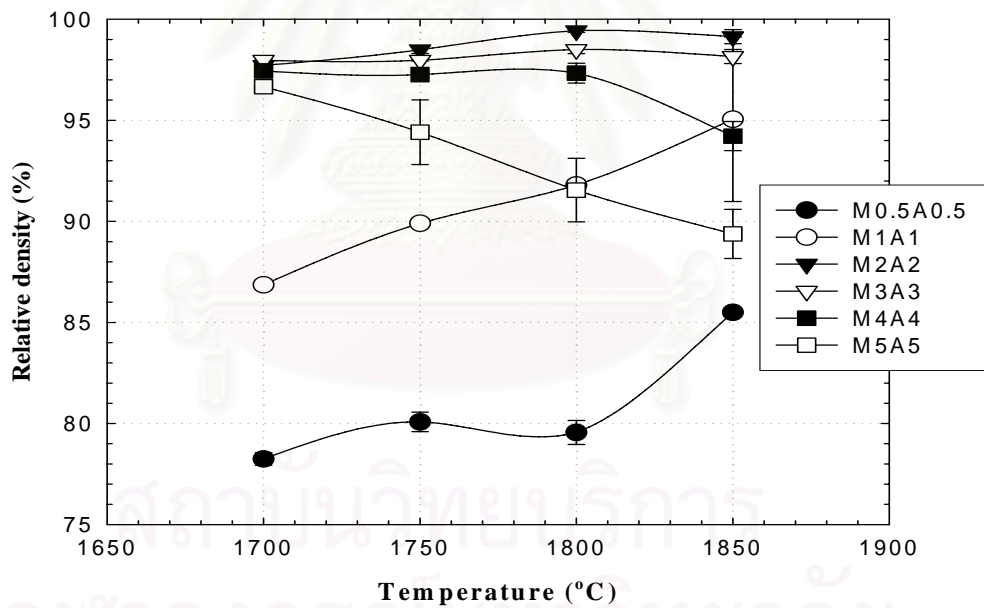
Fig. 4.19 Relative density of sintered β-Si_3N_4 with various contents of additives at 1700 °C to 1850 °C for 2 h under N_2 gas pressure of 1.0 MPa
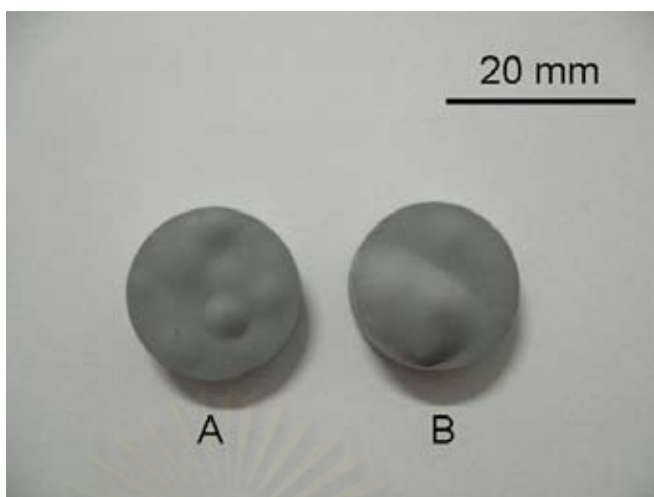
Fig. 4.20 Swollen specimens (M5A5) after sintering at 1800 °C (A) and 1850 °C (B) for 2 h

The effect of soaking time on the density of sintered specimens is presented in Fig. 4.21. From the result, bulk densities of specimens sintered with soaking time of 0.5, 2 and 6 h were 3.14, 3.16 and 3.20 g/cm^3, respectively, which corresponded to the relative densities of approximately 98, 99 and 100 % theoretical density. The soaking time of 0.5 h led to the lowest density, suggesting that 0.5 h was kinetically insufficient for completion of sintering process.
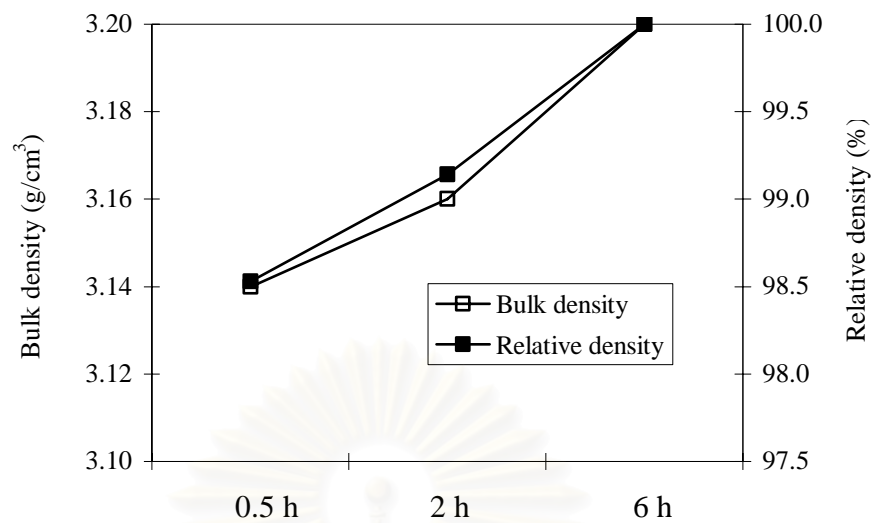
Fig. 4.21 Bulk density and relative density of specimens (M2A2) sintered at 1850 °C as a function of soaking time

4.2.4 Microstructure

Figure 4.22 shows the microstructure of sintered Si_3N_4 specimens (M2A2) as a function of sintering temperature. It can be seen that all specimens composed of equiaxed grains with bimodal size distribution. The average grain size of specimens as a function of sintering temperature is shown in Fig. 4.23. It shows that the grain size of specimens increased with increasing temperature up to 1800 °C and then was nearly constant at 1850 °C, implying that the increment of grain size was the result of large mass transport at the higher sintering temperature *(16)*. Grain growth was based on material transport due to the dissolution of small particles and re-precipitation on large particles *(15,64)*. In the dissolution and re-precipitation process, amount of liquid phase affects the grain growth rate. As seen in Fig. 4.16, mass loss of M2A2 increased with increasing sintering temperature. Increasing the mass loss means decreasing the liquid phase content. Therefore, grain size is affected positively by increasing temperature, but negatively affected by decreasing liquid phase content

at higher sintering temperature. Grain size in Fig. 4.23 might be the result of the both factors.

10 μm
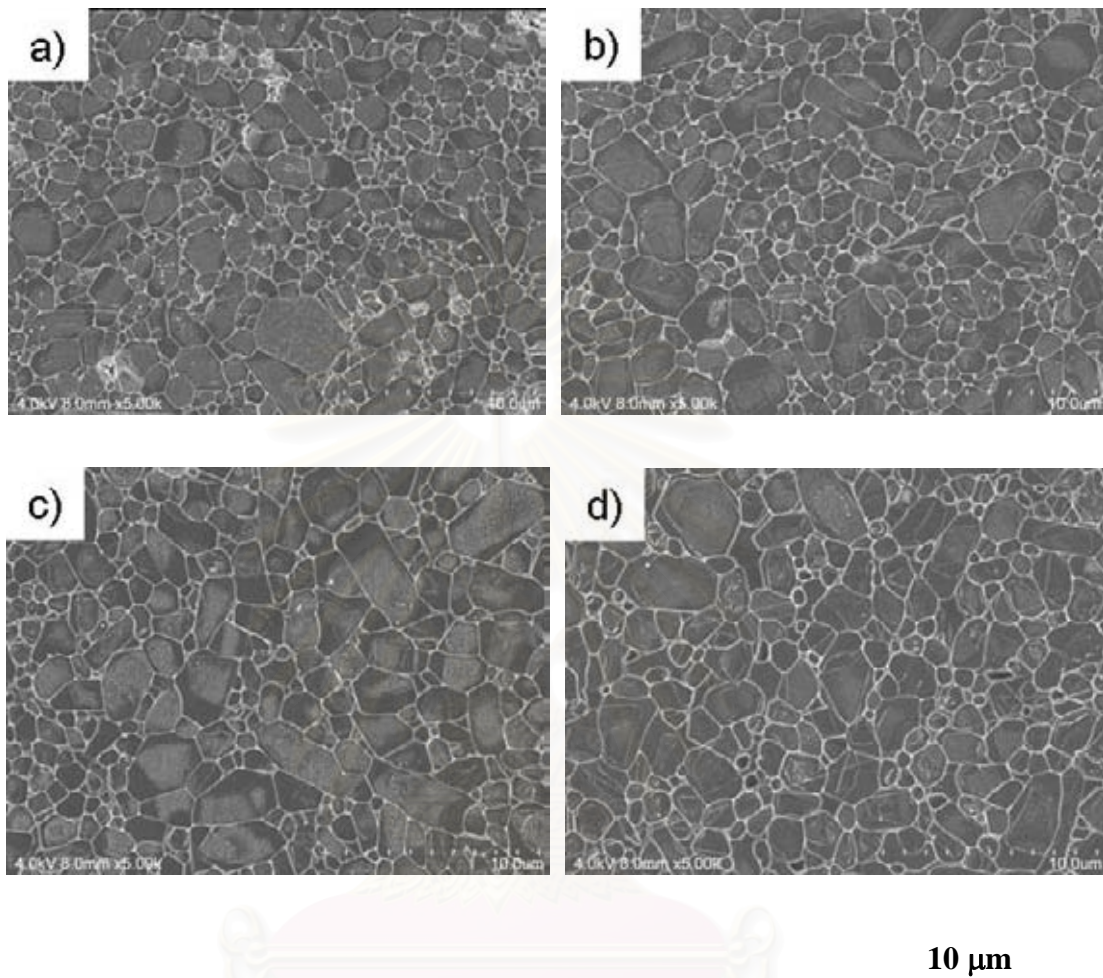
Fig. 4.22 SEM images of the specimens (M2A2) sintered at (a) 1700, (b) 1750, (c) 1800 and (d) 1850 °C for 2 h
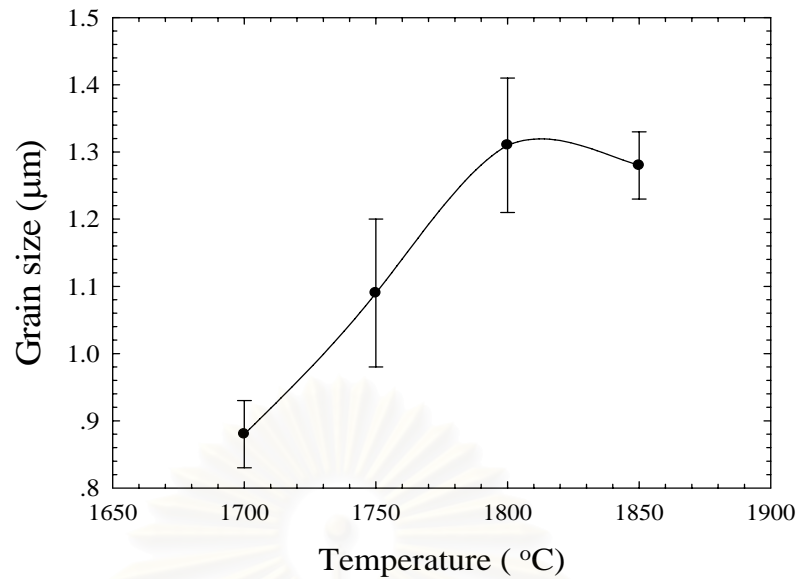
Fig. 4.23 Grain size of sintered Si$_3$N$_4$ specimens (M2A2) as a function of sintering temperature

The microstructures of specimens sintered with soaking time of 0.5 and 6 h are shown in Fig. 4.24. The 0.5 h specimen has equiaxed grains with monomodal size distribution, uniform microstructure and some amount of porosity. The porosity and small grain size are attributed to insufficient soaking time at the maximum sintering temperature; therefore, its density is lower than that of 6 h specimen. The 6 h specimen shows bimodal size distribution with large grains dispersed in small grain matrix due to Ostwald ripening *(6,66)*. No porosity was observed in this specimen. It means that the soaking time is large enough to get high density specimen and some large grains resulted from the grain growth. However, there were not so many needle-like grains (high aspect ratio) because the sintering temperature was too low to grow the needle-like grains *(66)*.
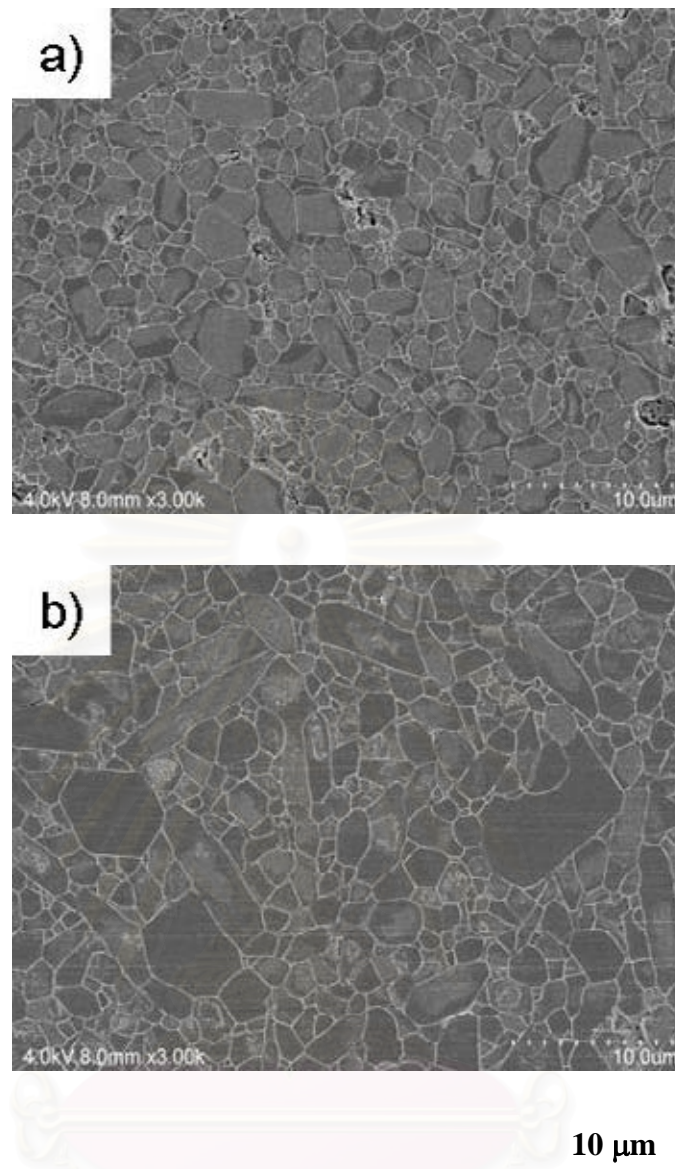
Fig. 4.24 SEM micrographs of specimens (M2A2) sintered at 1850 °C with different soaking times; (a) 0.5 h and (b) 6 h

Figure 4.25 shows a core/rim structure occurring in all sintered specimens. Core/rim structure is commonly seen in various materials fabricated by liquid-phase sintering *(112-113)*. In a solution-reprecipitation process of liquid-phase sintering, impurities or additives in the liquid are sometimes incorporated in the precipitated crystals. This phenomenon results in a different composition between the mother grains and grown crystals. An appropriate etching technique can bring out the difference in composition, so that core/rim structures can be seen. Hirosaki et al. *(114)*

reported that an EDX analysis of the core and rim indicated that the rim contained some aluminum (Al), although the aluminum was not detected in the core. The rate of plasma etching was varied, depending on the material composition *(115-116)*, making it possible to distinguish the core and rim on the basis of the difference in aluminum and oxygen contents.
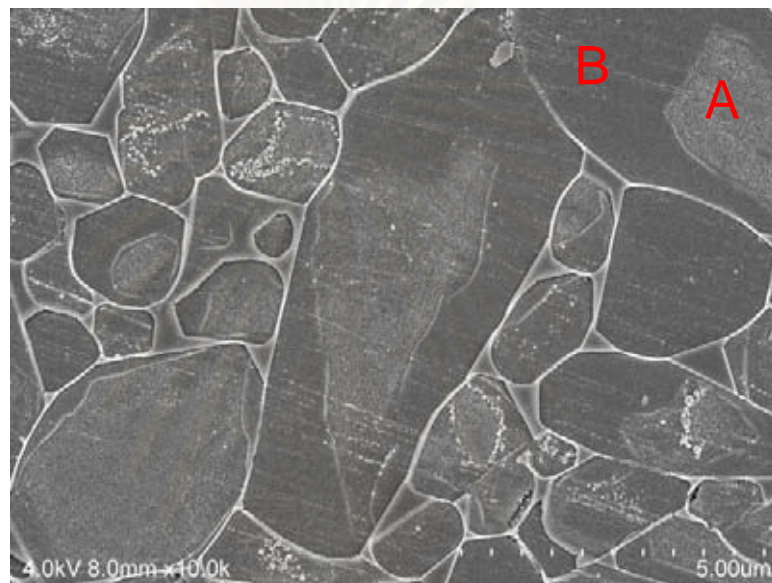
Fig. 4.25 SEM micrograph of core/rim structure of M2A2 specimen sintered at 1850 °C for 6 h; (A) core and (B) rim

4.2.5 Mechanical Properties

4.2.5.1 Effect of additive contents and sintering temperature

As shown in Fig. 4.26, flexural strength values of Si_3N_4 at the same sintering temperature slightly decreased with increasing additive contents. When increasing the sintering temperature, the flexural strengths slightly increased (comparing M2A2-1800 and M2A2-1850). M2A2-1850 specimen showed the highest strength value of 544 MPa.

Figure 4.27 shows Vickers hardness and fracture toughness of sintered specimens. The Vickers hardness and fracture toughness of M2A2-1850 specimens are 16 GPa and 5.9 MPa m$^{1/2}$, respectively, and are the highest values. Considering at the sintering temperature of 1800 °C, Vickers hardness decreased with increasing additive contents. It might be caused by the large amount of glassy phase resulting from increase in the additive content. For the fracture toughness, both of M2A2-1800 and M2A2-1850 show higher value than M3A3 and M4A4 sintered at 1800 °C.
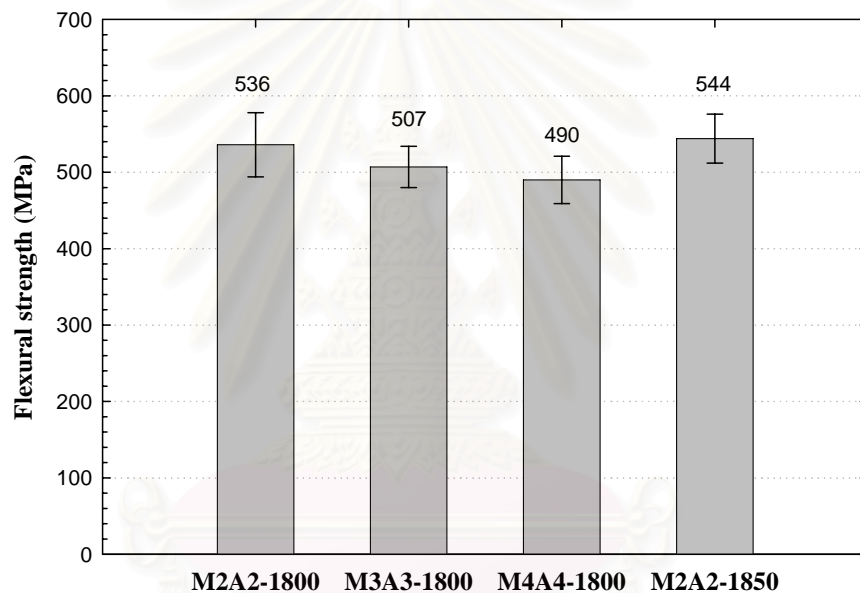
Fig.4.26 Flexural strength of sintered specimens with different contents of mixed additives at 1800 and 1850 °C
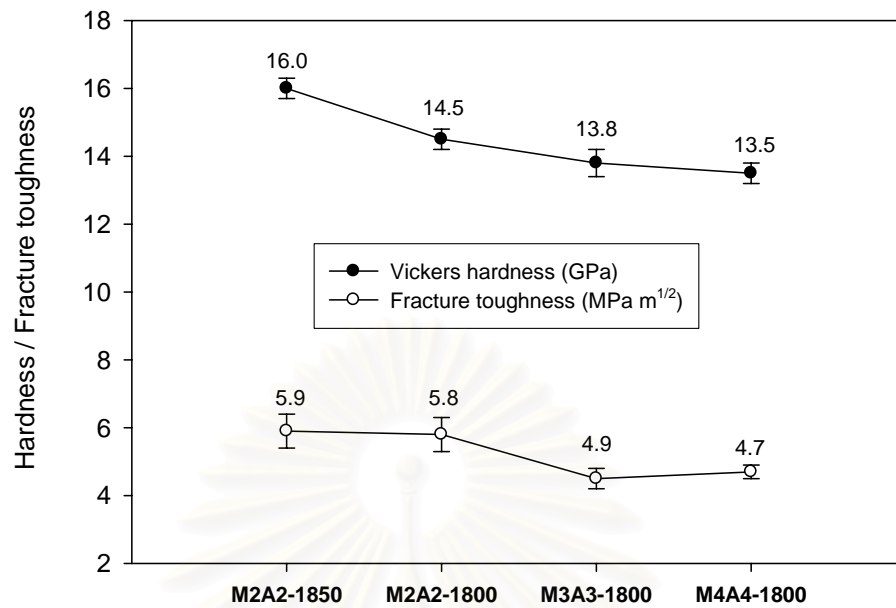
Fig. 4.27 Vickers hardness and fracture toughness of specimens sintered with different contents of mixed additives at 1800 and 1850 °C

4.2.5.2 Effect of soaking time

As seen in Fig. 4.28, the flexural strength of specimens (M2A2) with soaking time of 0.5, 2 and 6 h was 491, 544 and 528 MPa, respectively. The strengths of 2 h and 6 h specimens were insignificantly different, but the strength of 0.5 h specimen was quite lower than that of the others due to the lower density and much higher porosity.

Vickers hardness (Hv) and fracture toughness (K_{IC}) of specimens (M2A2) sintered with different soaking times are shown in Fig. 4.29. Hv and K_{IC} of 0.5, 2 and 0.6 h specimens were 12, 16 and 14 GPa, respectively. The 0.5 h specimen exhibited lower Hv than those of the 2 h and the 6 h sintered specimens because its density was lower. Although the density of the 2 h specimen was similar to the 6 h specimen, Hv of the 6 h specimen was lower than the 2 h specimen. The difference

might come from the difference in grain size, because a decrease in grain size was accompanied by an increase in hardness as the dislocations generated by the indenter were blocked by the grain boundaries *(117)*. The K_{IC} of 0.5 h, 2 h and 6 h specimens were 5.2, 5.9 and 5.7, respectively. The values were similar in all of the specimens.
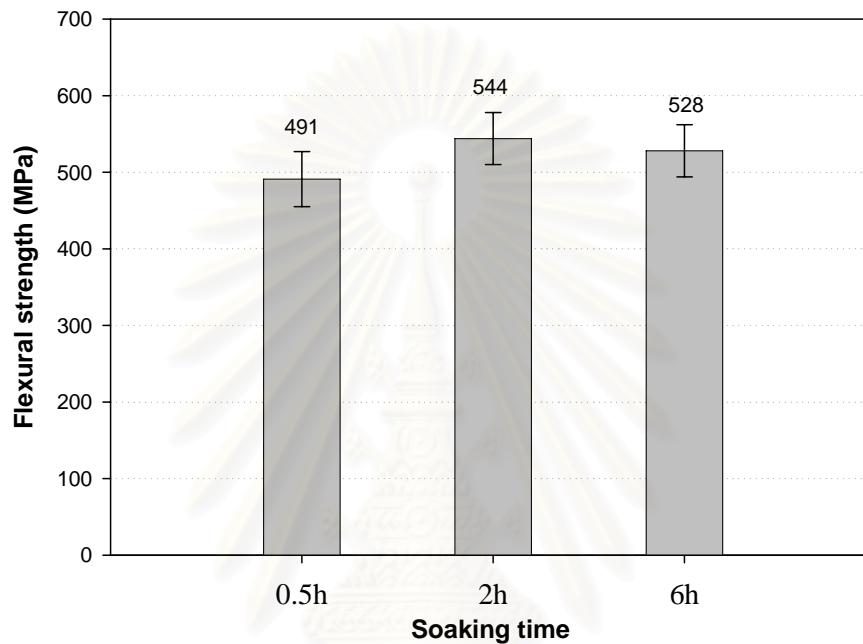
Fig.4.28 Flexural strength of specimens (M2A2) sintered at 1850 °C with different soaking times
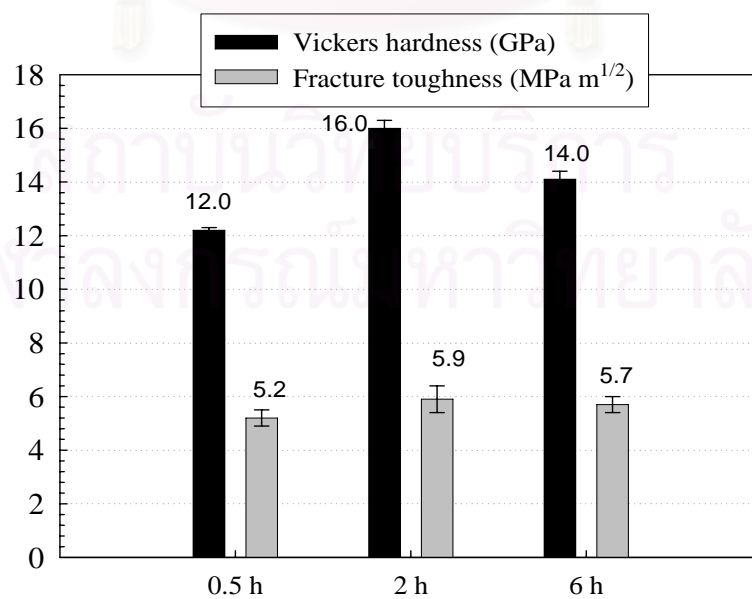
Fig. 4.29 Hardness (Hv) and fracture toughness (K_{IC}) of specimens (M2A2) sintered at 1850 °C with different soaking times

Figure 4.30 shows typical crack paths of specimens (M2A2) with different grain morphology which were obtained at two sintering conditions as 1850 °C/0.5 h and 1850 °C/6 h. The crack trajectory propagates through the pores and the relatively straight line without bridging and deflection due to the equiaxed microstructure in the specimen made at 1850 °C/0.5 h. The tortuous crack path is observed around the coarse elongated Si_3N_4 grains in the specimen sintered at 1850 °C/6h. It is obvious that the large elongated grain resulted in the increase in fracture toughness.
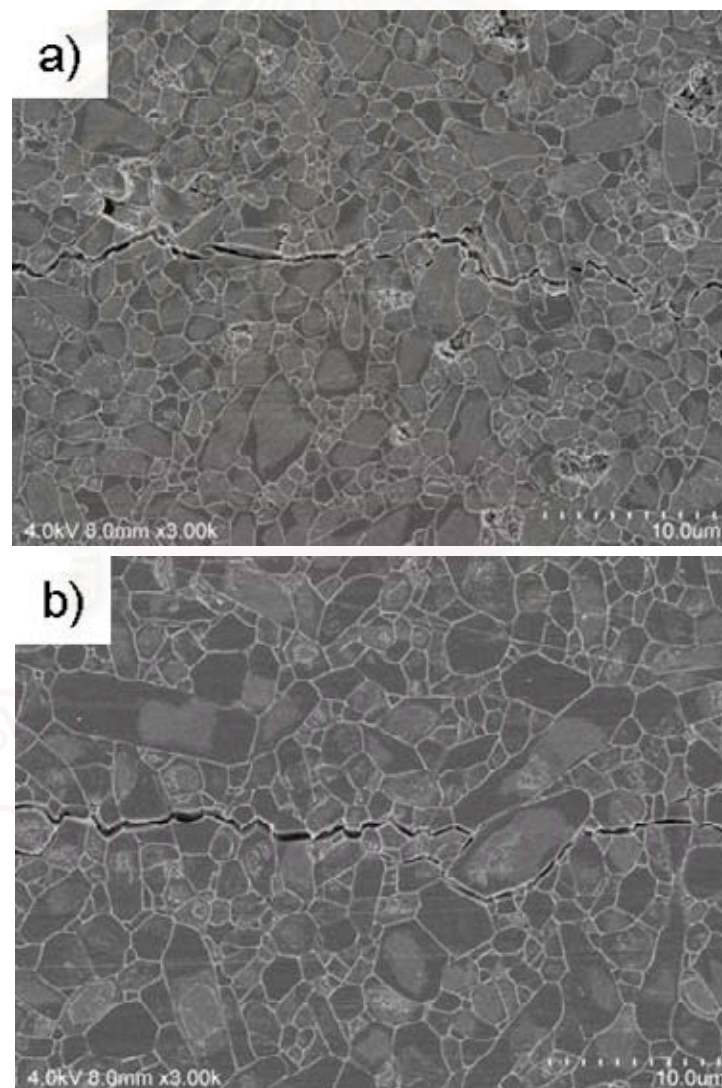
Fig. 4.30 SEM micrographs of crack propagation of Si_3N_4 (M2A2) sintered at 1850 °C, soaking time for (a) 0.5 h and (b) 6 h

4.3 Effect of Y_2O_3-Al_2O_3 on the Mechanical Properties of Si_3N_4

4.3.1 Mass Loss and Density

Mass loss, bulk density and relative density of sintered Si_3N_4 at 1850 °C for 2 h under N_2 gas pressure of 1.0 MPa with various Y_2O_3-Al_2O_3 contents are shown in Table 4.1. Mass loss values of all specimens were lower than those of specimens sintered with MgO-Al_2O_3 additives, because Y_2O_3 was more stable than MgO at high temperature *(98)*. Bulk density and relative density increased with increasing the amount of additives due to the increment of heavy elements in the specimens.

Table 4.1 Mass loss, bulk density and relative density of sintered Si_3N_4 with Y_2O_3-Al_2O_3 additives at 1850 °C for 2 h under N_2 pressure of 1.0 MPa

Samples	Mass loss (%)	Bulk density (g/cm^3)	*Relative density (%)
Y2A2	1.43	2.85	87.55
Y3A3	1.34	3.12	95.23
Y4A4	1.35	3.22	97.44
Y5A3	1.59	3.23	97.58

* based on the theoretical density of mixed powder with additives

4.3.2 Mechanical Properties

Figure 4.31 shows the Vickers hardness (Hv) and fracture toughness (K_{IC}) of sintered specimens as a function of Y_2O_3-Al_2O_3 content. Hardness is directly related to density which, in this case, increases with increasing additive content. Therefore, specimens with higher additive contents (Y4A4 and Y5A3) have higher Hv. The increase of K_{IC} with increasing additive content in this case, was not so significant, and was difficult to deduce, but this might have some connection to the increase in heterogeneity of grain size (see Fig. 4.33).

Figure 4.32 shows the flexural strengths of sintered Si_3N_4 under N_2 gas pressure of 1.0 MPa at 1850 °C for 2 h using Y_2O_3 and Al_2O_3 as additives. From the results in Fig. 4.32, the Y5A3 specimen, which contains 5 wt% Y_2O_3 and 3 wt% Al_2O_3, shows the highest flexural strength value of 543 MPa.
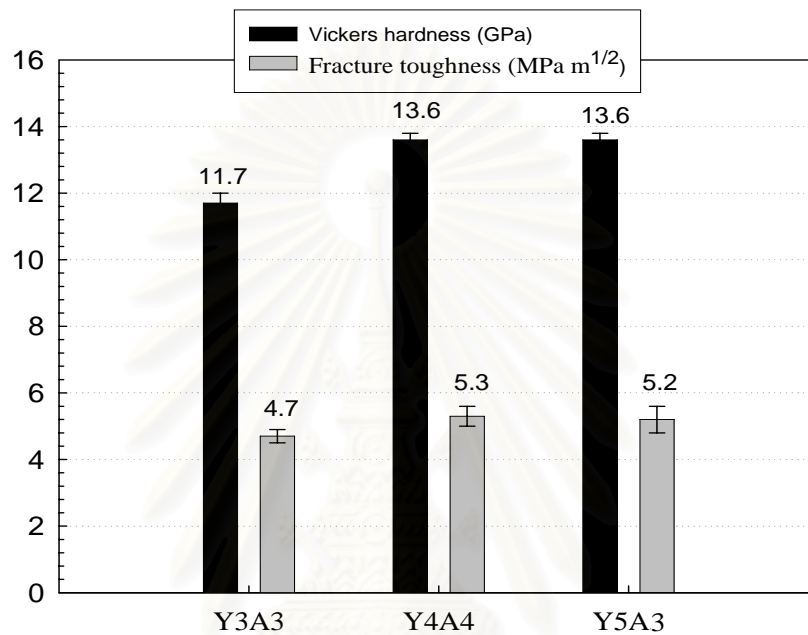
Fig. 4.31 Vickers hardness and fracture toughness of sintered specimens with Y_2O_3-Al_2O_3 additives, at 1850 °C for 2 h under N_2 pressure of 1.0 MPa
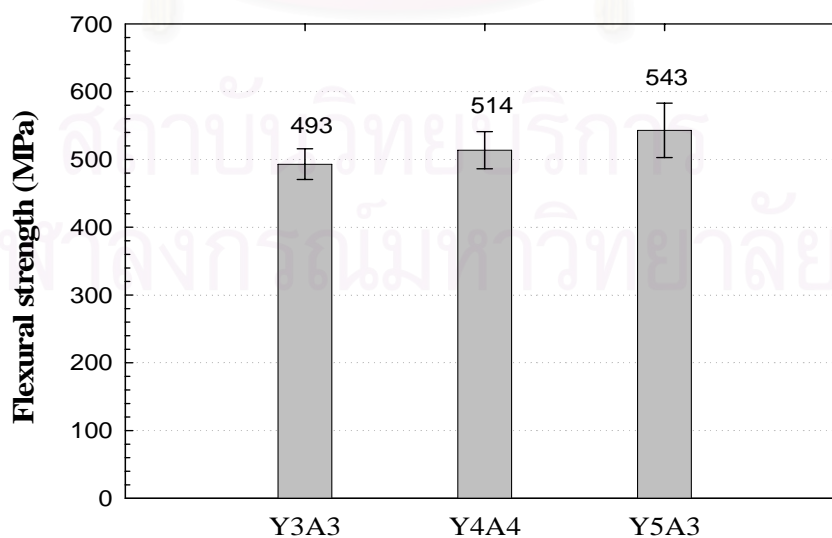
Fig. 4.32 Flexural strength of sintered specimens with Y_2O_3-Al_2O_3 additives, at 1850 °C for 2 h under N_2 pressure of 1.0 MPa
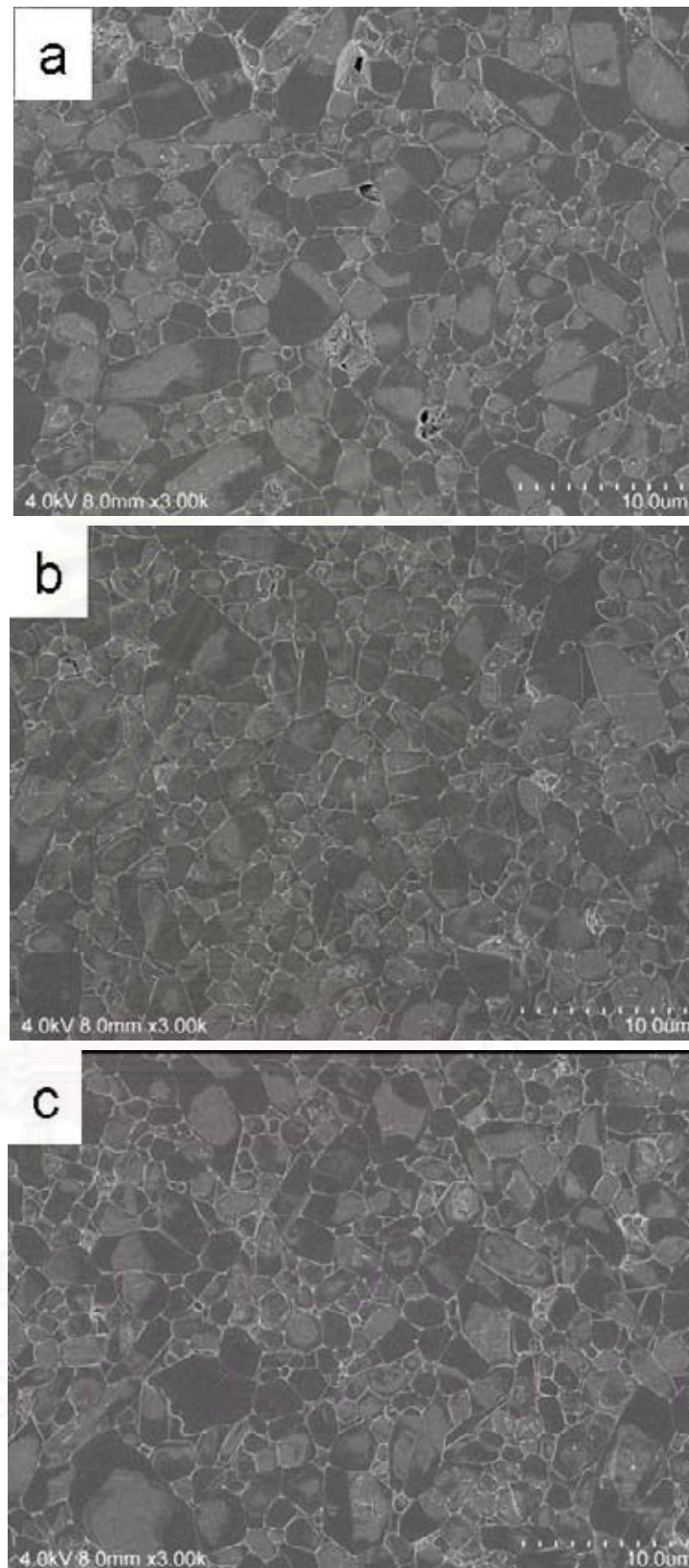
Fig. 4.33 SEM micrographs of sintered Si_3N_4 with various Y_2O_3 and Al_2O_3 contents, at 1850 °C for 2 h under N_2 gas pressure of 1.0 MPa

4.4 Wear Properties of the Sintered Si_3N_4 Ceramics

4.4.1 Properties of Sintered Si_3N_4

Properties of the sintered Si_3N_4 specimens selected for wear test are shown in Table 4.2. The densities of all samples were ~98 % of theoretical density. The highest mechanical properties 18.6 GPa for Hv, 8.2 MPa $m^{1/2}$ for K_{IC} and 875 MPa for flexural strength were shown in the specimen prepared from α type powder (*(a)*Y5A3). The values were higher than those of the materials prepared from β-powder. It is attributed to the smaller grain size and higher aspect ratio (see Fig. 4.34). As we known that the flexural strength and the fracture toughness of Si_3N_4 ceramics increase with increasing grain aspect ratio increased *(6,11,16,118-119)*. The material prepared from α-powder was fabricated and used as the reference material of wear test. For the samples prepared from low-cost β-powder (*(b)*Y5A3 and *(b)*M2A2), the mechanical properties of these samples were similar in spite of changing the type of sintering aid.

Table 4.2 Properties of the sintered Si_3N_4 specimens for wear test

Samples	Properties			
	*RD (%)	Hv (GPa)	K_{IC} (MPa $m^{1/2}$)	**Flexural strength (MPa)
*(a)*Y5A3	98	18.6	8.2	875 ± 98
*(b)*Y5A3	97	14.0	5.2	543 ± 40
*(b)*M2A2	98	16.0	5.9	544 ± 34

*Relative density, ** 3-point bending

Figure 4.34 shows SEM micrographs of the plasma etched surfaces of the Si_3N_4 specimens. The grain morphology of the materials prepared from β-powder (Fig. 4.34(a) and (b)) was equiaxial grain. In the case of the material prepared from α-powder, it contained typically bimodal structure consisting of small matrix grains dispersed in large high aspect ratio grains (Fig. 1(c)). It was caused by the

transformation of α-phase to β-phase during sintering *(120-122)*. The average grain

sizes are 1.28 μm for *(b)*M2A2, 1.63 μm for *(b)*Y5A3 and 0.40 μm for *(a)*Y5A3.

10 μm
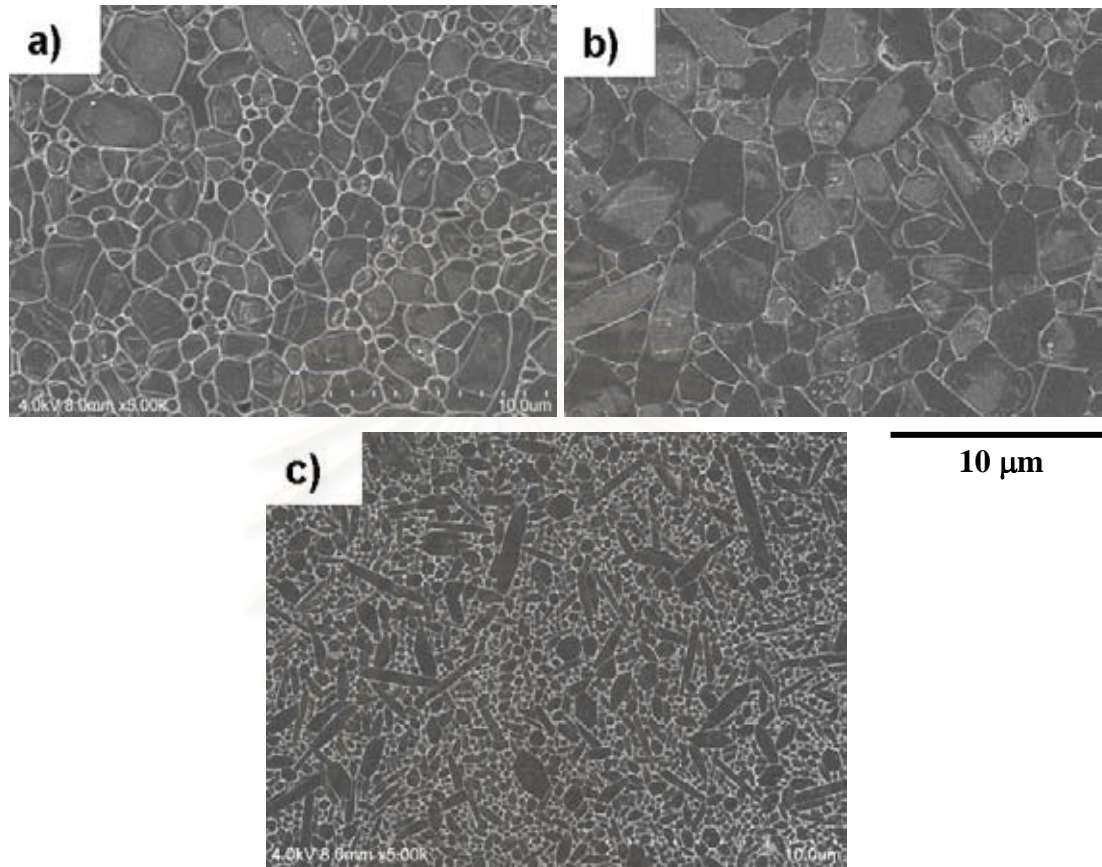
Fig. 4.34 SEM micrographs of Si_3N_4 specimens; a) *(b)*M2A2, b) *(b)*Y5A3 and c) *(a)*Y5A3, sintered at 1850 °C for 2 h under a nitrogen gas pressure of 1.0 MPa

4.4.2 Wear Property

The specific wear rates of the sintered Si_3N_4 ceramics prepared from

both of α type and β type powders are shown in Fig. 4.35. The wear resistance of

*(b)*M2A2 sample was close to the material prepared from the higher price α-powder

(*(a)*Y5A3). The difference in the wear rate for the sample containing different types

of starting powders and additives might be due to the differences in the mechanical

properties. However, the results of this experiment showed that the specific wear rate

of all samples was not so much different. Although the material prepared from α-powder had smaller grain sizes and higher mechanical properties, the specific wear rate of the material was almost similar to the ones prepared from β-powder. According to the previous work by Cho et al. *(123)*, wear resistance of ceramics increased with decreasing grain size. However, the reported relationships between wear resistance and microstructure were often contradictory. For example, Wang and Mao *(124)*, underlined that elongated grains not only improved both fracture toughness and strength due to the crack deflection process, but they also improved the wear resistance as result of the pullout mechanism of the grains. On the contrary, Zutshi et al. *(125)* found that the pullout mechanism caused third-body wear and this mechanism was enhanced when both the aspect ratio and the grain size increased.
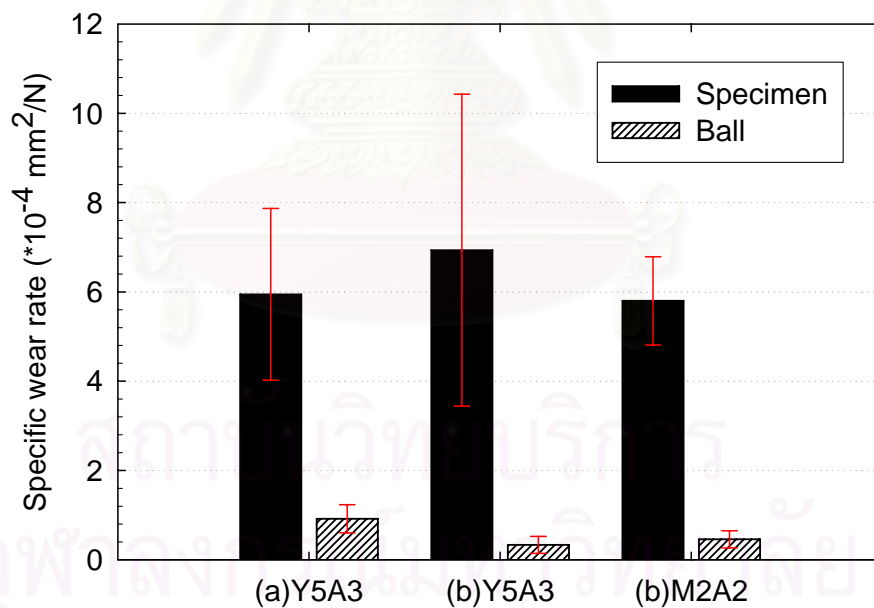
Fig. 4.35 Specific wear rate of sintered Si_3N_4 specimens
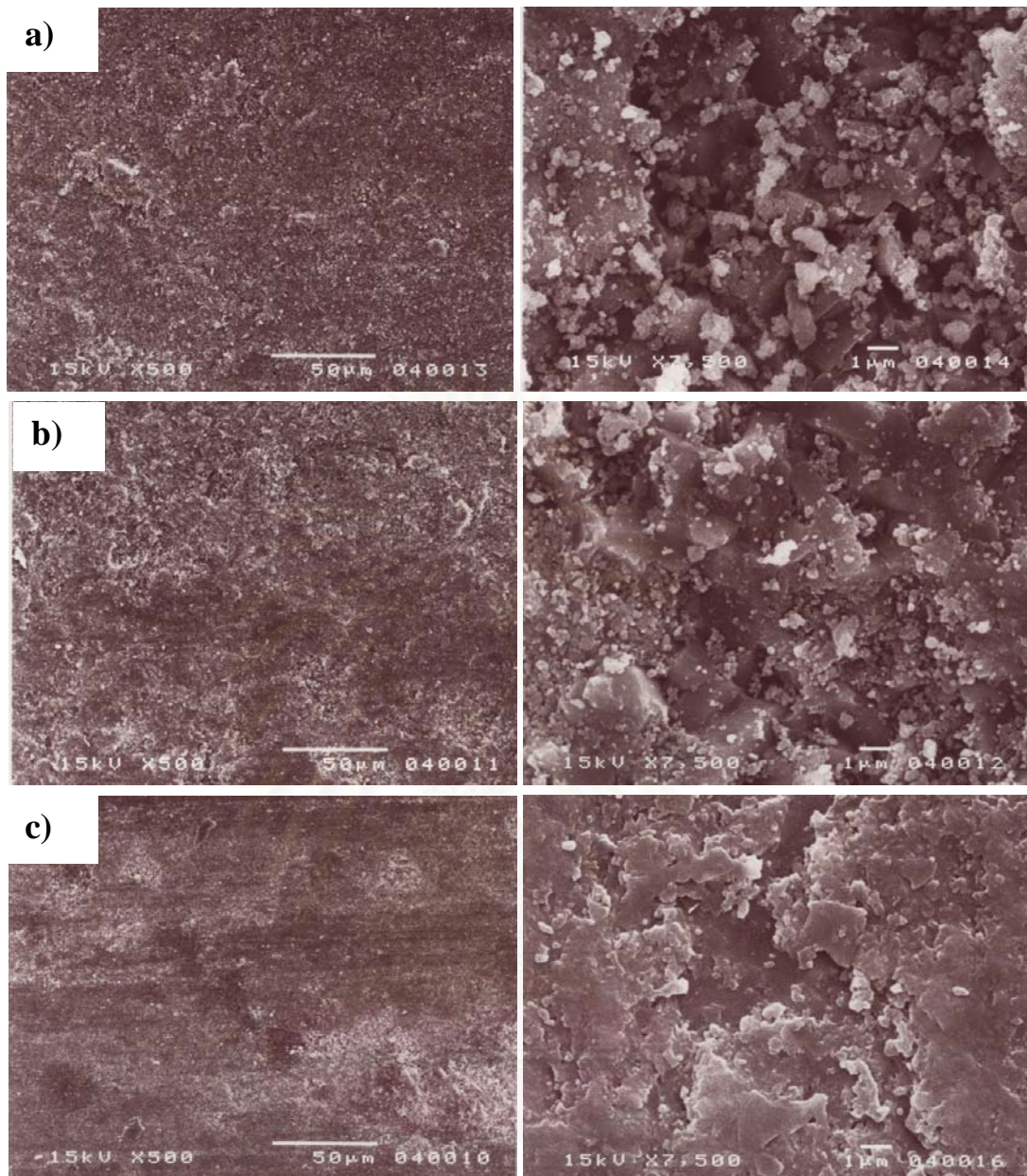
Fig. 4.36 Worn surfaces of the Si_3N_4 specimens after testing wear resistance; a) *(b)*M2A2, b) *(b)*Y5A3 and c) *(a)*Y5A3

Figure 4.36 shows the SEM images of the worn surfaces following the wear test. All samples exhibited surfaces showing typical abrasive wear with particulate debris and rough surface. This kind of surface appearance indicated that the wear mechanism was predominantly one of microstructure fracture. Generally, wear behaviors are affected by factors such as mechanical, thermal and chemical

properties. Also, they are influenced by composition, microstructure (such as grain size, grain boundary and others) and test conditions *(126)*.

4.5 Development of Microstructure of Si_3N_4 Prepared from Mixed β and α Powders

4.5.1 Mass Loss

Figure 4.37 shows the mass losses of sintered Si_3N_4 specimens as a function of sintering temperature. Mass loss of all specimens increased with increasing the sintering temperature according to their thermodynamics behavior. It is well known that the major mass loss reaction of Si_3N_4 ceramics comes from the reaction of Si_3N_4 and SiO_2 covering on its particles. The largest mass loss was found in 50SN7M4A4. It might be caused by the higher amount of MgO in its composition, because MgO is well known to be highly volatile when used for preparing Si_3N_4 ceramics. However, the content of Mg (O) in the sintered specimens has not been analyzed.
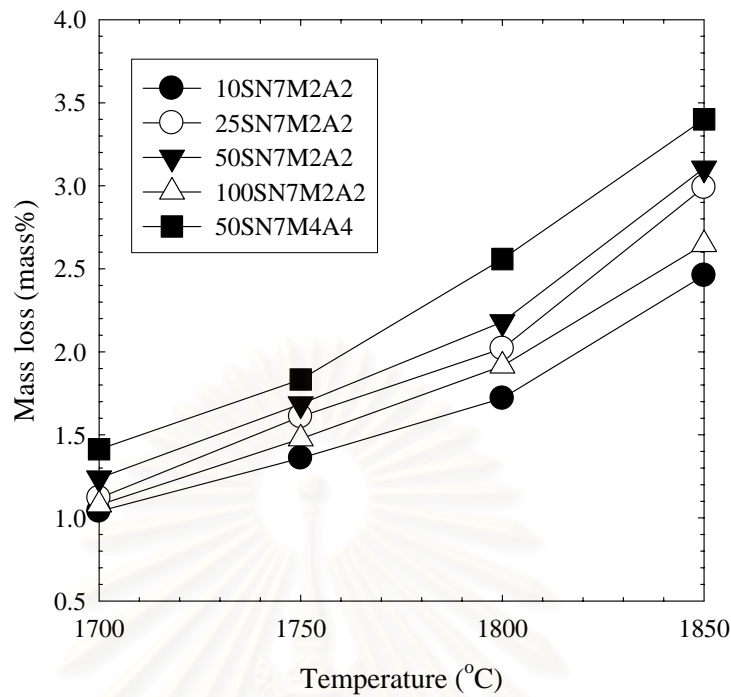
Fig. 4.37 Mass loss of the sintered Si_3N_4 with various temperatures and amounts of α phase contents

4.5.2 Density

Figure 4.38 shows bulk density of the sintered Si_3N_4 specimens as a function of sintering temperature which corresponds to the relative density shown in Fig. 4.39. The density of all samples except 50SN7M4A4 increased with increasing the sintering temperature. For 50SN7M4A4, the density slightly increased up to 1750 ℃ and decreased when the temperature was higher than 1750 ℃. The density was decreased dramatically due to the swelling of the specimens. The highest density of ~3.16 g/cm^3 (~98 % relative density) was obtained in the specimens containing 25 wt% and 100 wt% of SN-7 powder.
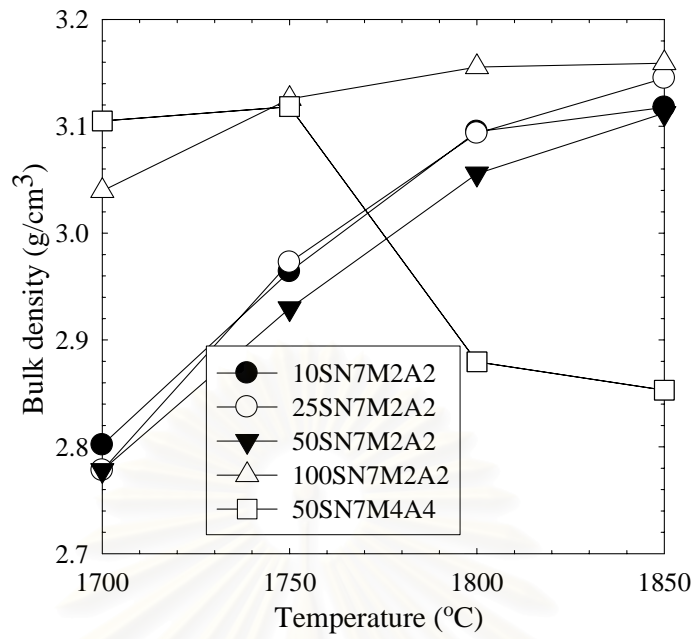
Fig. 4.38 Bulk density of the sintered Si_3N_4 with various temperatures and amounts of α phase contents
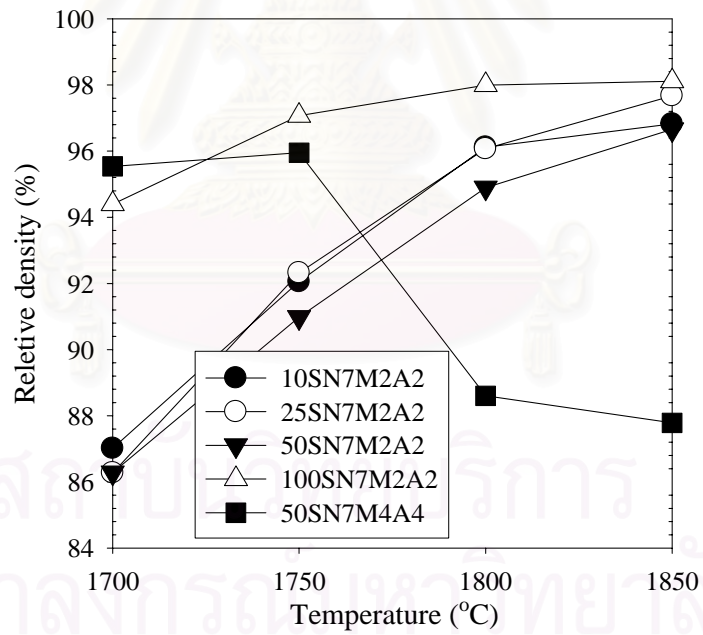
Fig. 4.39 Relative density of the sintered Si_3N_4 with various temperatures and amounts of α phase contents

4.5.3 Microstructure and Mechanical Strength

Figure 4.40 shows the fracture surfaces of the specimens sintered at 1850 ºC for 2 h under a nitrogen gas pressure of 1.0 MPa. The micrographs show that the needle-like shape or high aspect ratio grains gradually increased with amount of α phase content in the powder mixtures. It was corresponded to the amounts of α phase in the powder mixtures before sintering which were 7 wt% for 10SN7M2A2, 19 wt% 25SN7M2A2, 37 wt% for 50SN7M2A2 and 74 wt% for 100SN7 M2A2. For the specimens contained higher amount of α phase (Fig. 4.40 (c) and (d)), the materials exhibit a microstructure with self-reinforcing, abnormally-grown β-Si_3N_4 grains randomly embedded in a more equiaxed matrix. The needle-like shapes of β-Si_3N_4 grains come from α to β transformation during sintering *(69-70)*. At the time of liquid phase sintering of Si_3N_4, grain growth occurs during the solution-precipitation process, in which the grains with higher solubility are dissolved in the liquid phase and subsequently precipitated on β-nuclei with a lower solubility *(127)*. The solubility of a smaller grain in the liquid phase is higher than that of a larger one of the same phase, and the solubility of α phase grains is higher than that of β grains with a similar particle size and high α phase content in the matrix will increase the driving force for grain growth. As the amount of β phase in the starting powder increases, the microstructure will go through a refinement because the driving force for grain growth is lower and the grain growth is inhibited by other β-Si_3N_4 grains. The difference in microstructures of all specimens is also obviously seen from the polished and chemical etched surfaces shown in Fig. 4.41.
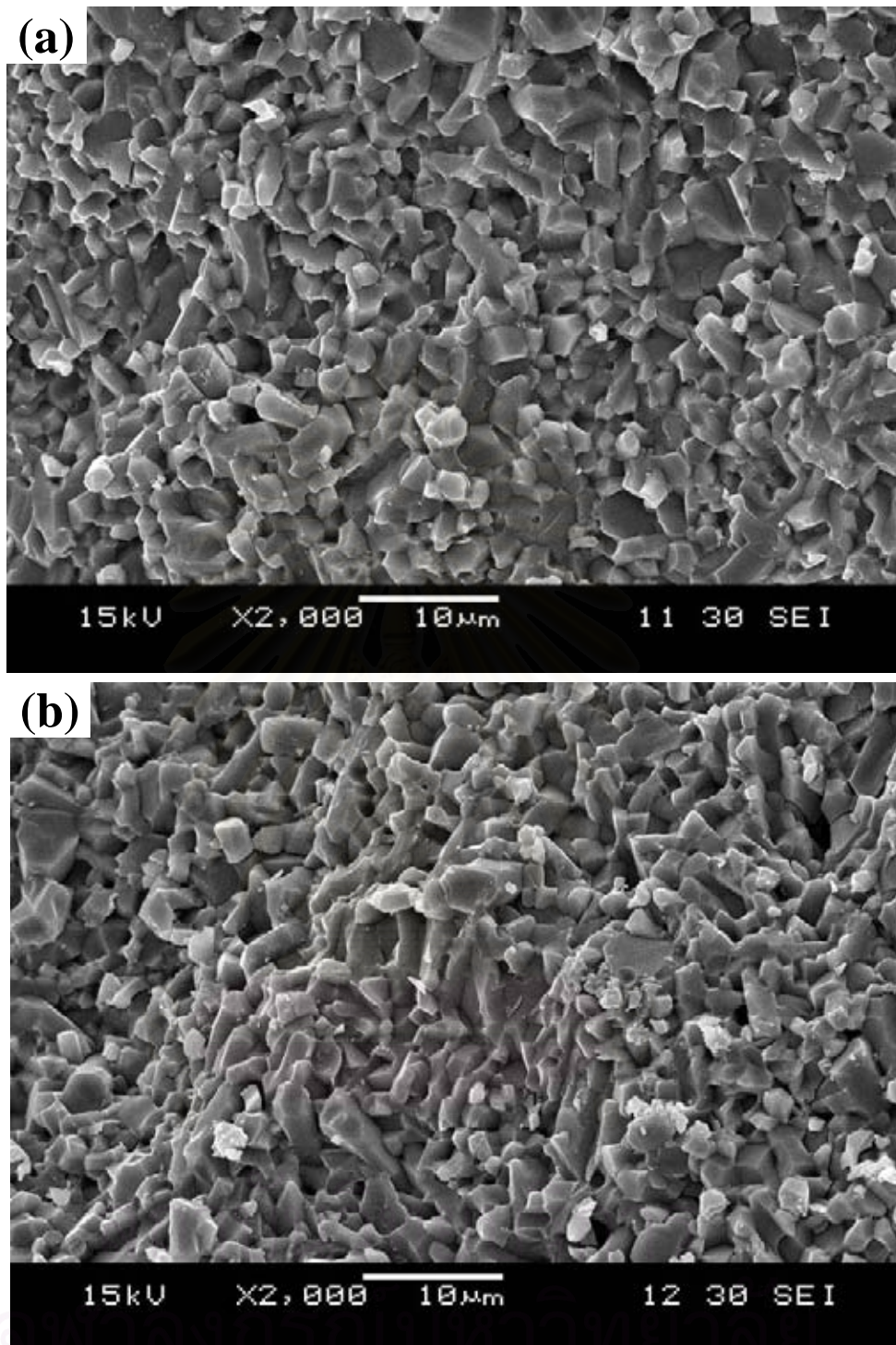
Fig. 4.40 Fracture surfaces of Si_3N_4 sintered at 1850 °C for 2 h under N_2 gas pressure of 1.0 MPa; (a) 10SN7M2A2, (b) 25SN7M2A2
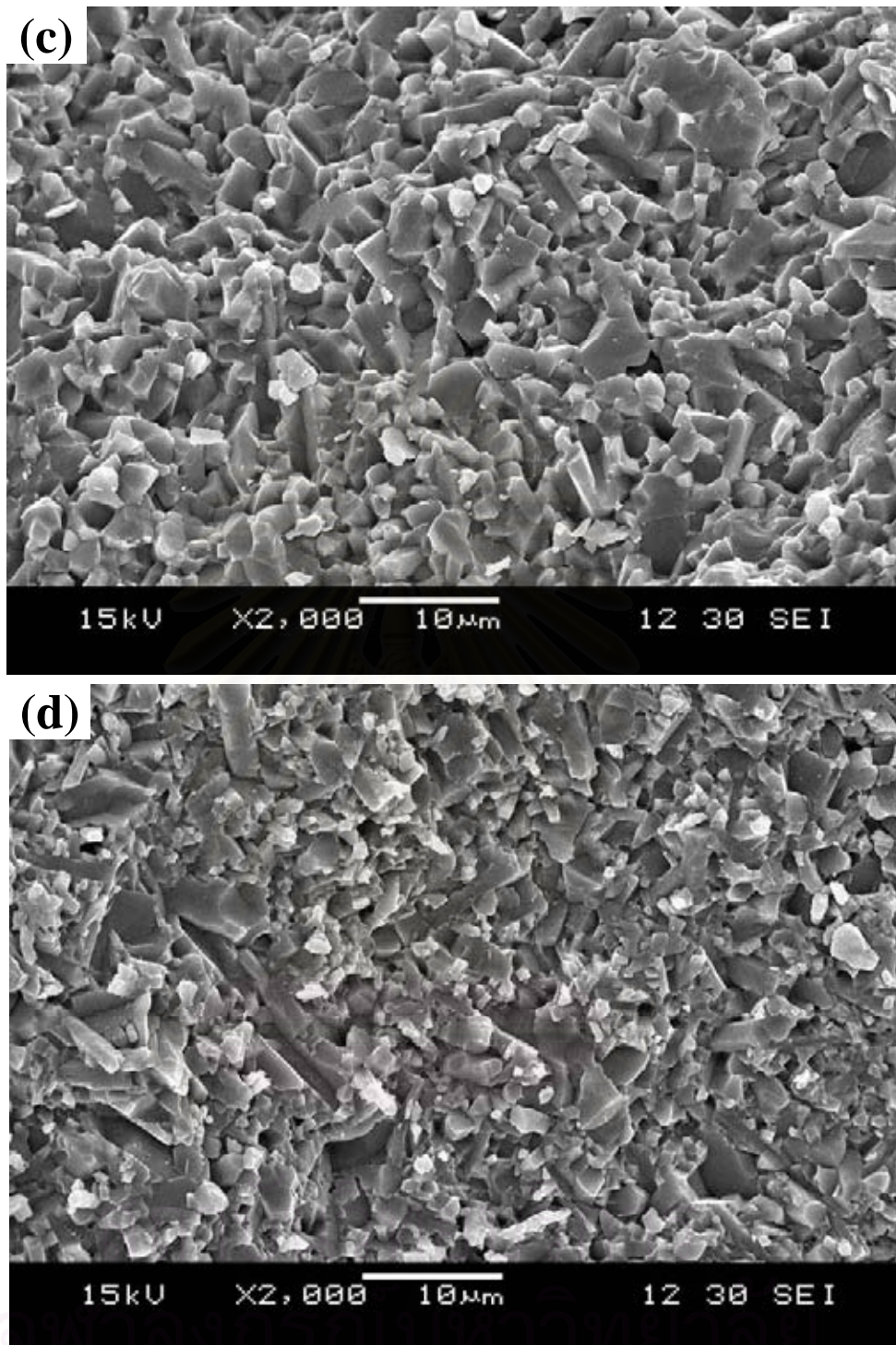
Fig. 4.40 (continued) Fracture surfaces of Si_3N_4 sintered at 1850 °C for 2 h under N_2 gas pressure of 1.0 MPa; (c) 50SN7M2A2 and (d) 100SN7M2A2
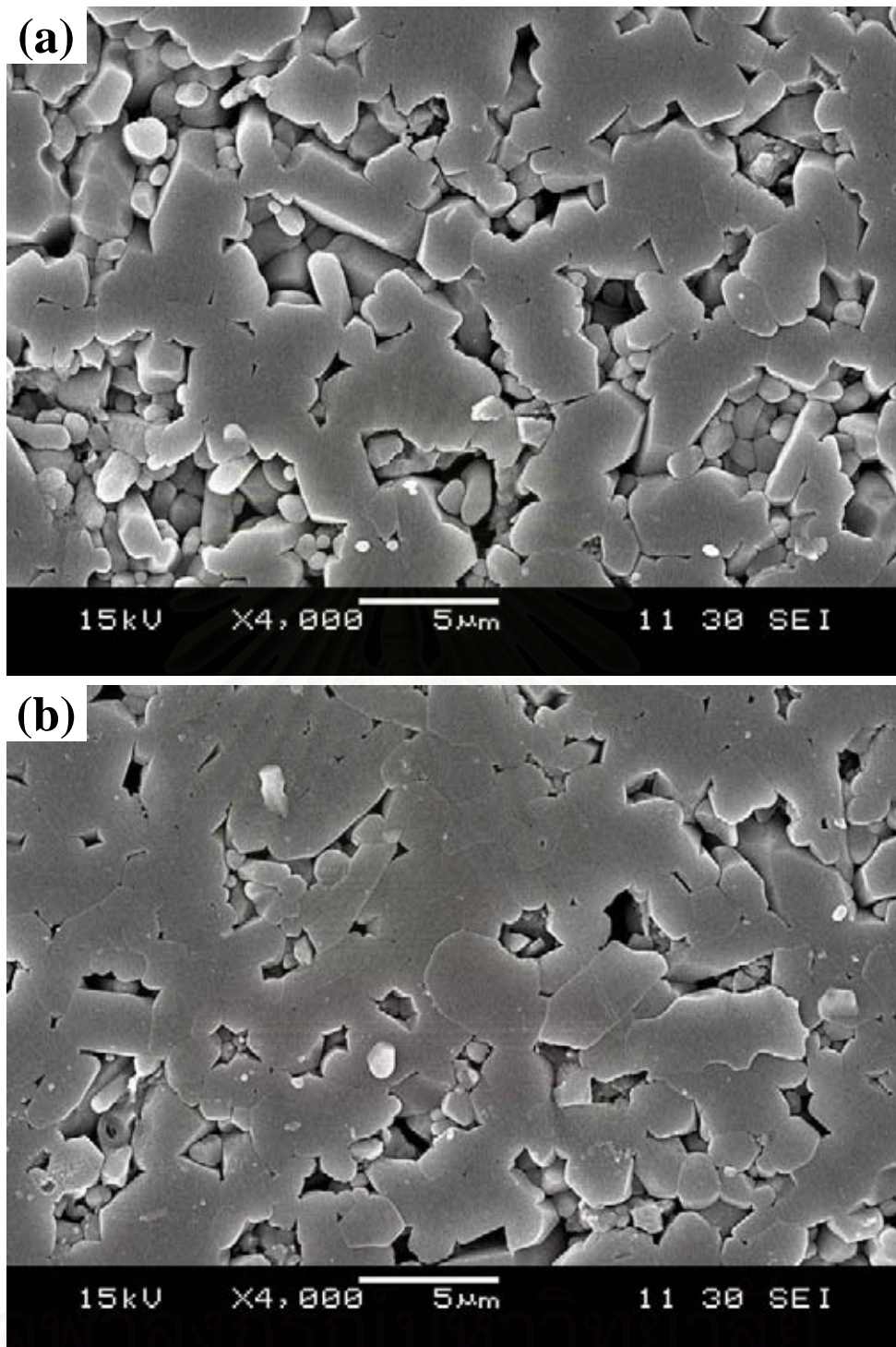
Fig. 4.41 SEM micrographs (polished and etched with 50% HF) of the Si_3N_4 sintered at 1750 °C for 2 h under N_2 gas pressure of 1.0 MPa; (a) 10SN7M2A2, (b) 25SN7M2A2
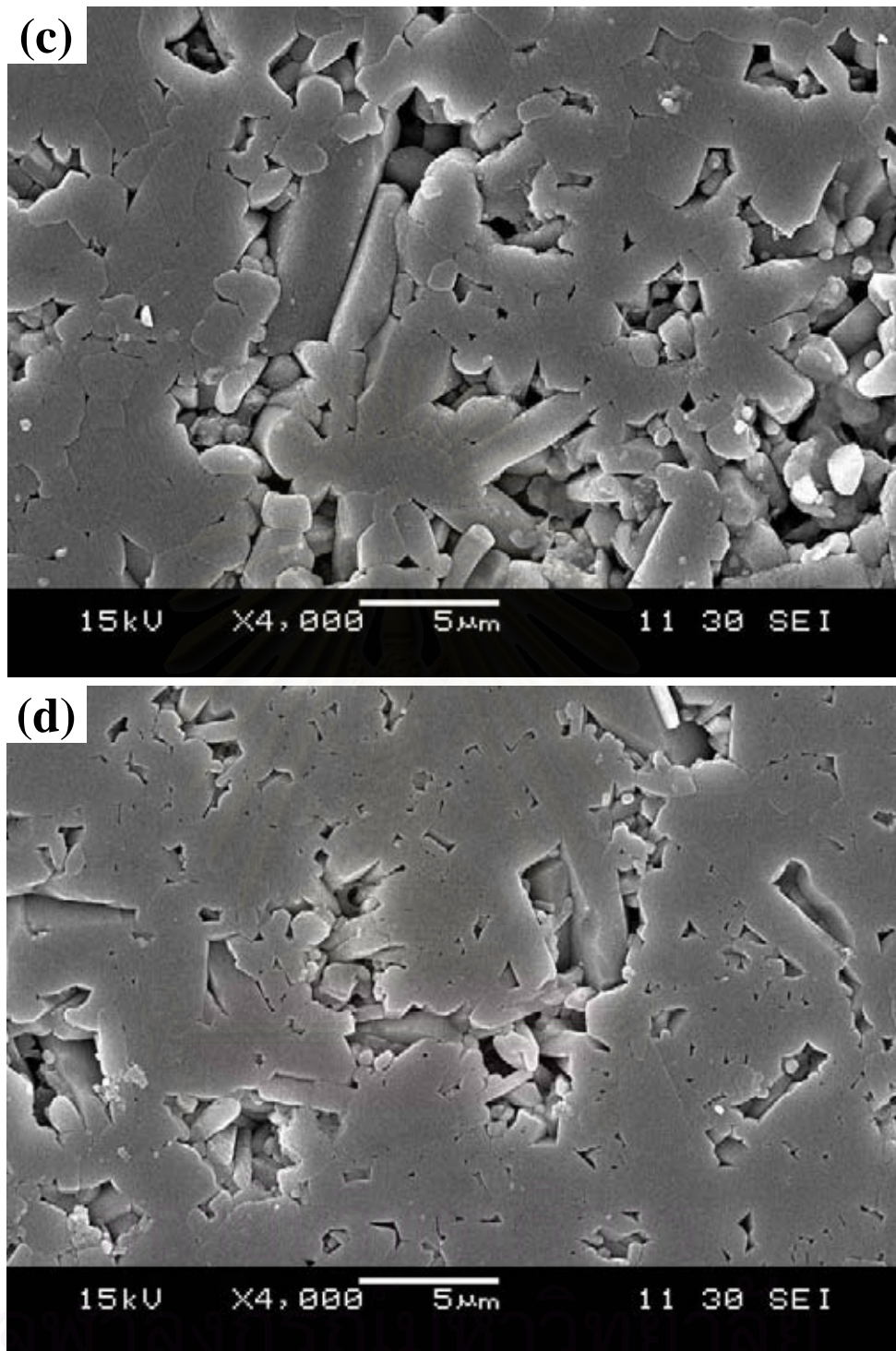
Fig. 4.41 (continued) SEM micrographs (polished and etched with 50% HF) of Si_3N_4 sintered at 1750 °C for 2 h under N_2 gas pressure of 1.0 MPa; (c) 50SN7M2A2, (d) 100SN7M2A2

The 3-point bending strengths of the sintered Si_3N_4 at 1850 °C for 2 h were 504 ± 59 MPa for 10SN7M2A2, 525 ± 50 MPa for 25SN7M2A2, 562 ± 37 MPa for 50SN7M2A2 and 624 ± 61 MPa for 100SN7M2A2. It indicates that the strengths of the specimens correspond to the amount of α content in the starting powders.

CHAPTER V

CONCLUSIONS AND RECOMMENDATIONS

5.1 Conclusions

The solid/gas reaction during sintering of Si_3N_4 ceramics in air atmosphere was investigated through the experimental data of the sintered specimens and packing powders. The following conclusions are drawn.

(1)   Mass loss of Si_3N_4 ceramics sintered in air significantly increased as a function of SiO_2 content in the specimen, but was less affected by the temperature change. The mass losses of the specimen placed at the top and the bottom positions in the small crucible were different due to the difference of the oxygen partial pressure during sintering. The main mass loss of Si_3N_4 specimen was due to the following reaction:

$$Si_3N_4\,(s) + 3SiO_2\,(s,l) \rightarrow 6SiO\,(g) + 2N_2\,(g)$$
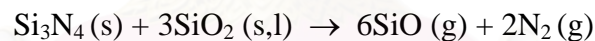
(2)   There was a gradient of the oxygen partial pressure (Po_2) in the small crucible during sintering. The Po_2 at the top side of the crucible was assumed to be lower than the bottom side. This assumption was convinced by the formation of Si_2N_2O in the bottom surface of the sintered specimen, of which the content decreased inward.

(3)   The trends of mass loss with increasing temperature between sintering under air and N_2 atmospheres were obviously different.

For the improvement of the mechanical properties part, the target properties of the Si_3N_4 ceramics to be developed and the obtained properties of M2A2 specimen are shown in Table 5.1. From the result in the Table 5.1, all the properties except the fracture strength exceed those of the target values. Although the obtained fracture strength is approximately 79% of the target, the standard deviation (S.D.) is only 6.3 % which is quite small because, generally, the S.D. of ceramics is over 10-15 %. Though the higher price α-phase powder was added to M2A2 specimen, the fracture strength increased insignificantly. The flexural strength value was higher than 600 MPa when the α-phase powder (SN-7) was used.

Table 5.1 Comparison of the target values and achieved values of sintered Si_3N_4 in this project.

Properties	Commercial Si_3N_4 *(78)*	M2A2
Relative density (%)	99.0	99.0
Vickers hardness (GPa)	14.5	16.0
Flexural strength (MPa at RT)	690	544 ±34
Fracture toughness (MPa m$^{1/2}$)	5.7	5.9

5.2 Recommendations

(1) Reduction of glassy phase in the specimen by reducing O_2 contamination in the powder after milling or mixing would also enhance the fracture strength of the sintered Si_3N_4 ceramic. Therefore, the effort to realize this assumption by reducing the O_2 content without increasing the process cost should be researched. To perform this research, a large Si_3N_4 mill and Si_3N_4 media balls and a rotary evaporator are necessary.

(2)   Finding practical applications is of great interest for the achieved Si_3N_4 ceramic because it has some potential benefits to industries as replacement of high grade alumina ceramics.

REFERENCES

(1)   Verevka, V. G. et al. Mechanical properties of structural ceramic materials based on silicon nitride. Refractories and Industrial Ceramics 37, 11-12 (1996): 387-390.

(2)   Terwilliger, G. R. Properties of sintered Si_3N_4. J. Am. Ceram. Soc. 57, 1 (1974): 48-49.

(3)   Zhoua, L. et al. Preparation of Si_3N_4 ceramics with high strength and high reliability via a processing strategy. J. Eur. Ceram. Soc. 22 (2002): 1347–1355.

(4)   Watari, K. and Shinde, S. L. High thermal conductivity materials. MRS Bulletin (June 2001): 440-441.

(5)   Kitayama, M. et al. Thermal Conductivity of β-Si_3N_4: I, Effects of various microstructural factors. J. Am. Ceram. Soc. 82, 113 (1999): 105-112.

(6)   Ziegler, G., Heinrich, J. and Wotting, G. Relationships between processing, microstructure and properties of dense and reaction-bonded silicon nitride. J. Mater.Sci. 22 (1987): 3041-3086.

(7)   Richerson, D. W. Modern ceramic engineering: properties, processing and use in design. New York: Marcel Dekker, Inc., 1982.

(8)   Bengisu, M.. Engineering Ceramics. New York: Springer, 2001.

(9)   Saito, S. Fine Ceramics. New York: Elsevier, 1988.

(10)   www.kyocera.com/kicc/industrial/types/index.htm

(11)   Riley, F. L. Silicon nitride and related materials. J. Am. Ceram. Soc. 83, 2 (2000): 245-265.

(12)   Wada, S., Hattori, T. and Yokoyama, K. Sintering of Si_3N_4 ceramics in air atmosphere furnace. J. Ceram. Soc. Japan. 109 (2001): 281-283.

(13)   Wada, S. et al. Sintering of Si_3N_4 ceramics in air atmosphere furnace (Part 2). J. Ceram. Soc. Japan. 112 (2004): 234-237.

(14)   Plucknett, K. P. and Lin, H.T. Sintering silicon nitride ceramics in air. J. Am. Ceram. Soc. 88, (2005): 3538-3541.

(15) Mitomo, M., Tsutsumi, M. and Tanaka, H. Grain growth during gas-pressure sintering of β-silicon nitride. J. Am. Ceram. Soc. 73, 8 (1990): 2441-2445.

(16) Hirosaki, N., Akimune, Y. and Mitomo, M. Effect of grain growth of β-silicon nitride on strength, Wiebull modulus, and fracture toughness. J. Am. Ceram. Soc. 76, 7 (1993): 1892-1894.

(17) Hirosaki, N. et al. Sintering of Y$_2$O$_3$-Al$_2$O$_3$-doped β-Si$_3$N$_4$ powder and mechanical properties of sintered materials. J. Ceram. Soc. Japan. 102, 8 (1994): 790-794.

(18) Hirosaki, N. et al. Effect of purification of β-Si$_3$N$_4$ powder on the strength of sintered materials. J. Ceram. Soc. Japan. 103, 6 (1995): 639-643.

(19) Ogasawara, T. et al. Fatigue behavior of silicon nitride ceramics prepared from β-phase powder. J. Ceram. Soc. Japan. 103, 7 (1995): 709-712.

(20) Okamoto, Y. et al. Mechanical properties and oxidation resistance of silicon nitride produced from low purity β-powder. J. Ceram. Soc. Japan. 103, 7 (1995): 720-723.

(21) Wangmooklang, N. Development of low cost Si$_3$N$_4$ ceramics. Master's Thesis, Department of Materials Science, Faculty of Science, Chulalongkorn University, 2004.

(22) Hardie, D. and Jack, K. H. Crystal structures of silicon nitride. Nature (London United Kingdom) 180 (1957): 332-333.

(23) Zerr, A. et al. Synthesis of cubic silicon nitride. Nature (London, United Kingdom) 400 (1999): 340-342.

(24) Wang, C. M., Pan, X. and Ruhle, C. Review silicon nitride crystal structure and observations of lattice defects. J. Mater. Sci. 31 (1996): 5281-5298.

(25) Sekine, T. Shock synthesis of cubic silicon nitride. J. Am. Ceram. Soc. 85 (2002): 113-116.

(26) Rhodes, W. and Natansonh, S. Powder for advanced structural ceramics. Am. Ceram. Soc. Bull. 68 (1989): 1804-1812.

(27) Atkinson, A. Moulson, A. J. and Roberts, E. W. Nitridation of high-purity silicon. J. Am. Ceram. Soc. 59, 7-8 (1973): 285-289.

(28) Jennings, H. M. and Richman, M. H. Structure, formation mechanisms and kinetics of reaction-bonded silicon nitride. J. Mater. Sci. 8 (1983): 951-967.

(29) Pigeon, R. G. and Varma, A. Quantitative kinetic analysis of silicon nitridation. J. Mater. Sci. 28 (1993): 2999-3013.

(30) Varma, A., Pigeon, R. G. and Miller, A. E. Kinetics of α- and β-Si$_3$N$_4$ formation from oxide-free high-purity Si powder. J. Mater. Sci., 26 (1991): 4541-4544.

(31) Segal, D. L. Developments in the synthesis of silicon nitride. Chemistry and industry, 16 (1985): 544-545.

(32) Ekelund, M. and Forslund, B. Carbothermal preparation of silicon nitride: Influence of starting material and synthesis parameters. J. Am. Ceram. Soc. 75, 3 (1992): 532-539.

(33) Schwier, G., Nietfeld, G. and Franz, G. Production and characterization of silicon nitride powders. Materials Science Forum, 47 (1989): 1-20.

(34) Yamada, T. Preparation and evaluation of sinterable silicon nitride powder by imide decomposition method. Am. Ceram. Soc. Bull. 72, 5 (1993): 99-106.

(35) Ault, N. and Yeckley, R. L. Silicon nitride. Am. Ceram. Soc. Bull. 73, 6 (1994): 129-133.

(36) Greskovich, C. and Rosolowski, J. H. Sintering of covalent solid. J. Am. Ceram. Soc. 59, 7-8 (1976): 336-343.

(37) Greskovich, C. and Prochazka, S. Stability of Si$_3$N$_4$ and liquid phase(s) during Sintering. J. Am. Ceram. Soc. 63 (1981): C96-C97.

(38) Heuer, A. H. and Lou, V. L. Volatility diagrams for silica, silicon nitride, and silicon carbide and their application to high-temperature decomposition and oxidation. J. Am. Ceram. Soc. 73, 10 (1990): 2789-2803.

(39) Clarke, D. R. and Thomas, G. Grain boundary phases in a hot-pressed MgO fluxed silicon nitride. J. Am. Ceram. Soc., 60, 11-12 (1977): 491-495.

(40) Benco, L. Chemical bonding at grain boundaries: MgO on β-Si$_3$N$_4$. Surface Science., 327 (1995): 274-284.

(41) Clarke, D. R. and Lange, F. F. Oxidation of Si$_3$N$_4$ alloys: relation to phase equilibria in the system Si$_3$N$_4$-SiO$_2$-MgO. J. Am. Ceram. Soc. 63 (1980): 586-593.

(42) Bowen, L. J., et al. Mechanism of densification during the pressure sintering of alpha-silicon nitride. Ceramugia International 2, 4 (1976): 173-176.

(43) Sajgalik, P. and Haviar, M. Pressureless sintering of Si$_3$N$_4$ with Y$_2$O$_3$ and Al$_2$O$_3$ additives—Compatibility of powder beds. Ceram. Int. 18 (1992): 279-283.

(44) Yang, J. F., Ohji, T. and Niihara, K. Influence of yttria-alumina content on sintering behavior and microstructure of silicon nitride ceramics. J. Am. Ceram. Soc. 83 (2000): 2094-2096.

(45) Jack, K. H. and Wilson, W. I. Ceramics based on the Si-Al-O-N and related systems. Nature (London) Phys. Sci. 238, 80 (1972): 28-29.

(46) Lange, F. F., Singhal, S. C. and Kuznicki, R. C. Phase relations and stability studies in the Si$_3$N$_4$–Si$_2$N$_2$O–SiO$_2$–Y$_2$O$_3$ pseudo-ternary system. J. Am. Ceram. Soc. 60, 5-6 (1977): 249-252.

(47) Gauckler, L. J., Hohnke, H. and T. Y. Tien, T. Y. The system Si$_3$N$_4$– Y$_2$O$_3$– SiO$_2$. J. Am. Ceram. Soc. 63, 1-2 (1980): 35-37.

(48) Gazza, G. E. Effect of yttria additions on hot-pressed Si$_3$N$_4$. Am. Ceram. Soc. Bull. 54, 9 (1975): 778–781.

(49) Weaver, G. Q. and Lucek, J. W. Optimization of hot-pressed Si$_3$N$_4$ and Y$_2$O$_3$ materials. Am. Ceram. Soc. Bull. 57, 12 (1978): 1131-1136.

(50) Das, P. K and Mukerji, J. Sintering of silicon nitride densified with liquids in the system MgO-AlN-SiO$_2$. J. Eur. Ceram. Soc. 5 (1989): 105-112.

(51) Huseby, I. C., Lukas, H. L. and Petzow, G. Phase equilibria in the system Si$_3$N$_4$– SiO$_2$–BeO–Be$_3$N$_2$. J. Am. Ceram. Soc. 58, 9-10 (1976): 377

(52) Palm, J. A. and Greshkovich, C. D. Thermomechanical properties of hot-pressed S1$_{2.9}$Be$_{0.1}$N$_{3.8}$O$_{0.2}$. Am. Ceram. Soc. Bull. 59 (1980): 447-452.

(53) Haitao, Y., et al. Crystallization of MgO during sintering of silicon nitride with magnesia and ceria. J. Mater. Sci. 34 (1999): 2875-2878.

(54) Yang, H., Yang, G. and Yuan, R. Pressureless sintering of silicon nitride with magnesia and ceria. Mater. Res. Bull. 33, 10 (1998): 1467-1473.

(55) Gao, L., et al. Sintering and microstructure of silicon nitride with magnesia and cerium additives. J. Mater. Proc. Tech. 115 (2001): 298-301.

(56) Dutta, S. and Buzek, B. Microstructure, strength, and oxidation of a 10 wt% zyttrite-Si_3N_4 ceramic. J. Am. Ceram. Soc. 67 (1984): 89-92.

(57) Hoffmann, M. J. Relationship between microstructure and mechanical properties of silicon nitride ceramics. Pure & App. Chem. 67, 6 (1995): 939-946.

(58) Lu, H. H. and Huang, J. L. Effect of Y_2O_3 and Yb_2O_3 on the microstructure and mechanical properties of silicon nitride. Ceram. Int. 27 (2001): 621-628.

(59) Lange, F. F. Volatilization associated with the sintering of polyphase Si_3N_4 Materials. J. Am. Ceram. Soc. 65 (1982): C120-C121.

(60) Lou, V. K., Mitchell, T. E. and Heuer, A. H. Review—Graphical displays of the thermodynamics of high-temperature gas-solid reactions and their application to oxidation of metals and evaporation of oxides. J. Am. Ceram. Soc. 68 (1985): 49-58.

(61) Kingery, W. D. Densification during sintering in the presence of a liquid phase. I. Theory. J. App. Phys. 30 (1959): 301-306.

(62) Kingery, W. D. Introduction to Ceramics, John Wiley, New York, 1960.

(63) German, R. M. Sintering theory and practice, John Wiley & Sons, Inc.: New York, 1996.

(64) Rahaman, M. N. Ceramic processing and sintering. Dekker: New York, 1959.

(65) Bowen, L. J., et al. Hot-pressing and the α−β phase transformation in silicon nitride. J. Mater. Sci. 13 (1978): 341-351.

(66) Sarin, V. K. On the α-to-β phase transformation in silicon nitride. Mater. Sci. Eng. A 105/106 (1988): 151-159.

(67) Ordonez, S. Iturriza, I. and Castro, F. The influence of amount and type of additives on $\alpha \rightarrow \beta$ Si$_3$N$_4$ transformation. J. Mater. Sci. 34 (1999): 147-153.

(68) Petzow, G. and Herrmann, M. Structure and Bonding; Vol. 102. Springer-Verlag: Berlin, 2002.

(69) Brook, R. J., Messier, D. R. and Riley, F. L. The α/β silicon nitride phase transformation. J. Mater. Sci. 13 (1978): 1199–205.

(70) Okamoto, Y., et al. Effect of α/β phase transformation on the rate of grain growth. J. Ceram. Soc. Jpn. 105 (1977): 476.

(71) Einarsrud, M. A. and Mitomo, M. Mechanism of grain growth of β-SiAlON. J. Am. Ceram. Soc. 76 (1993): 1624-1624.

(72) Kleebe, H. J. Structure and chemistry of interfaces in Si$_3$N$_4$ ceramics studied by transmission electron microscopy. J. Ceram. Soc. Jpn. 105 (1997): 453-475.

(73) Park, H., Kim, H. E. and Niihara, K. Microstructural evolution and mechanical properties of Si$_3$N$_4$ with Yb$_2$O$_3$ as a sintering additive. J. Am. Ceram. Soc., 80 (1997): 750–756.

(74) De Arellano-Lopez, et al. Microstructure and room-temperature mechanical properties of Si$_3$N$_4$ with various α/β phase ratios. J. Mater. Sci. 33 (1998): 5803–5810.

(75) Rodel, J. Interaction between crack deflection and crack bridging. J. Eur. Ceram. Soc. 10 (1992): 143-150.

(76) Faber, K. T. and Evans, A. G. Crack deflection processes—I. Theory. Acta. Matall. 31 (1983): 565-576.

(77) Hoffmann, M. J. and Petzow, G. Tailored microstructures of silicon nitride ceramics. Pure & Appl. Chem. 66, 9 (1994): 1807-1814.

(78) http://www.accuratus.com/silinit.html

(79) Komeya, K. Fine Ceramics, ed. S. Saito, Elsevier Science Publishing: NewYork, 1988.

(80) Fyzik, A. J. and Beaman, D. R. Microstructure and properties of self-reinforced silicon nitride. J. Am. Ceram. Soc. 76 (1993): 2737-2744.

(81) Yoshimura, M., et al. Grain size controlled high-strength silicon nitride ceramics. J. Ceram. Soc. Jpn. (1995): 407.

(82) Kramer, M., Hoffmann, M. J. and Petzow, G. Grain growth studies of silicon nitride dispersed in an oxynitride glass. J. Am. Ceram. Soc. 76 (1993): 2778-2784.

(83) Peillon, F. C. and Thevenot, F. Microstructural designing of silicon nitride related to toughness. J. Eur. Ceram. Soc. 22 (2002): 271-278.

(84) Becher, P.F., et al. Toughening behavior in whisker-reinforced ceramic matrix composites. J. Am. Ceram. Soc. 71 (1988): 1050-1061.

(85) Sajgalik, P., Dusza, J. and Hoffmann, M. Relationship between microstructure, toughening mechanisms, and fracture toughness of reinforced silicon nitride ceramics J. Am. Ceram. Soc. 78 (1995): 2619-2624.

(86) Lee, S. G., Kim, Y. W. and Mitomo, M. Relationship between microstructure and fracture toughness of toughened silicon carbide ceramics. J. Am. Ceram. Soc. 84 (2001): 1347–1353.

(87) Peterson, I. and Tien, T. Effect of the grain boundary thermal expansion coefficient on the fracture toughness in silicon nitride. J. Am. Ceram. Soc. 78 (1995): 2345-2352.

(88) Tanaka, I.,et al. Hot isostatic press sintering and properties of silicon nitride without additives. J. Am. Ceram. Soc. 72 (1989): 1656-1660.

(89) Mende, S., et al. Proceeding of 10th European Symposium on Comminution. 2-5 September Heidelberg Germany, 2002.

(90) Becker, M., Kwade, A. and Schwedes, J. Proceeding of World Congress on Particle Technology 3, 2002

(91) Catalogue of Wiley A. Bachofen AG Maschinenfabrik

(92) British Standard. Advanced Technical Ceramics—Monolithic Ceramic—General and Textural Properties—Part3: Determination of grain size and size distribution (characterized by the linear intercept method), BS EN 623-3: 2001.

(93)   Prochazka, S.   Advances in Ceramics Vol.21: Ceramic Powder Science, The American Ceramic Society, 1987.

(94)   Wada, S. Increase of oxygen content in Si_3N_4 powder during ball milling using alcohol as solvent, J. Ceram. Soc. Japan. 104 (1996): 1092-1094.

(95)   Yokoyama, K. and Wada, S. Solid-gas reaction during sintering of Si_3N_4 ceramics, Part 4: Mass loss reaction and morphology of Si_3N_4 ceramics, J. Ceram. Soc. Japan. 108 (2000): 357-364.

(96)   Yokoyama, K. and Wada, S. Solid-gas reaction during sintering of Si_3N_4 ceramics, Part 5: Mass change reaction of Si_3N_4 ceramics during sintering under N_2 gas flow in a non-carbon-element furnace, J. Ceram. Soc. Japan., 108 (2000): 627-632.

(97)   Yokoyama, K. and Wada, S. Solid-gas reaction during sintering of Si_3N_4 ceramics, Part 6: Suppression of mass loss reaction of Si_3N_4 ceramics during sintering, J. Ceram. Soc. Japan. 109 (2001): 238-243.

(98)   Wada, S. Control of instability of Si_3N_4 during pressureless sintering. J. Ceram. Soc. Japan. 109 (2001): 803-808.

(99)   Z. K. Huang, P. Greil and G. Petzow. Formation of silicon oxynitride from Si_3N_4 and SiO_2 in the presence of Al_2O_3, Ceram. Int., 10 (1984): 14-17.

(100) Mitomo, M., et al. Effect of atmosphere on the reaction sintering of Si_2N_2O, Ceram. Int. 15 (1989): 345-350.

(101) Ohashi, M. and Iida, Y. Nucleation control for hot –working of Si_2N_2O based ceramics, J. Mater. Res. 14 (1999): 170-177.

(102) Ohashi, M., Kanzaki, S. and Tabata, H. Processing, mechanical properties, and oxidation behavior of oxynitride ceramics, J. Am. Ceram. Soc. 74 (1991): 109-114.

(103) Ohashi, M., et al. Factors affecting mechanical properties of silicon oxynitride ceramics, Ceram. Int. 23 (1997): 27-37.

(104) Ohashi, M., Kanzaki, S. and Tabata, H. Effect of additives on some properties of silicon oxynitride ceramics, J. Mater. Sci. 26 (1991): 2608-2614.

(105) Lewis, M. H., Reed, C. J. and Butler, N. D. Pressureless-sintered ceramics based on the compound Si_2N_2O. Mater. Sci. Eng. 71 (1985): 87-94.

(106) Li, Y. L., Zheng, F. and Liang, Y. Reaction and formation of crystalline silicon oxynitride in Si-O-N systems under solid high pressure. J. Am. Ceram. Soc. 84 (2001): 875-877.

(107) Wang, C., Emoto, H. and Mitomo, M. Nucleation and growth of silicon oxynitride grains in a fine-grained silicon nitride matrix. J. Am. Ceram. Soc. 81 (1998): 1125-1132.

(108) Larker, R. Reaction sintering and properties of silicon oxynitride densified by hot isostatic pressing. J. Am. Ceram. Soc. 75 (1992): 62-66.

(109) Wallace, L. V. and Howard, G. M. Active-to-passive transition in the oxidation of silicon carbide and silicon nitride in air. J. Am. Ceram. Soc. 73 (1990): 1540-1543.

(110) Singhal, S. C. Thermodynamic analysis of the high-temperature stability of silicon nitride and silicon carbide, Ceram. Int. 2 (1979): 123-130.

(111) Yokoyama, K. and Wada, S. Solid-Gas Reaction during Sintering of Si_3N_4 Ceramics (Part 3): Mass losses in a Carbon Heater Furnace. J. Ceram. Soc. Japan. 108, 3 (2000): 230-235.

(112) Rudiser, O. and Exner, H. E. Application of basic research to the Development of Hard Metals. Powder Metall. Int. 8 (1976): 7-13.

(113) Sigl, L. S. and Kleebe, H. J. Core/rim structure of liquid-phase-sintered silicon carbide, J. Am. Ceram. Soc. 76 (1993): 773-776.

(114) Hirosaki, N., Akimune, Y. and Mitomo, M. Microstructure characterization of gas-pressure-sintered β-silicon nitride containing large β-silicon nitride seeds. J. Am. Ceram. Soc. 77 (1994): 1093-1097.

(115) Mitomo, M., et al. Plasma etching of non oxide ceramics, J. Matar. Sci. Lett. 10 (1991): 83-84.

(116) Mitomo, M., et al. Plasma etching of α-SiAlON Ceramics. J. Am. Ceram. Soc. 74 (1991): 856-858.

(117) McColm, I. J. Ceramic Hardness. Plenum Press: New York, 1990.

(118) Lange, F. F. Relation between strength, fracture energy, and microstructure of hot-pressed Si_3N_4. J. Am. Ceram. Soc. 56, 10 (1973): 518-522.

(119) Hoffmann, M. J. et al. Relationship between microstructure, toughening mechanisms, and fracture toughness of reinforced silicon nitride ceramics. J. Am. Ceram. Soc. 78, 10 (1995): 2619-2624.

(120) Messier, D. R., Riley, F. L. and Brook, R. J. The α/β silicon nitride phase transformation, J. Mater. Sci. 13 (1978): 1199-1205.

(121) Greskovich C. and Prochazka, S. Observations on the $\alpha \rightarrow \beta$-Si_3N_4 transformation. J. Am. Ceram. Soc. 60, 9-19 (1977): 471-472.

(122) Proksova, M. and Panek, Z. Phase transformation and densification during pressureless sintering of Si_3N_4 with MgO and $Y_3Al_5O_{12}$ additives. J. Mater. Sci. 25 (1990): 3709-3713.

(123) Cho, S. J., et al. Grain-size and R-curve effects in the abrasive wear of aluminas. J. Am. Ceram. Soc. 72, 7 (1989): 1249-1252.

(124) Wang, D. and Mao, Z. Studies on abrasive wear of monolithic silicon nitride and a silicon carbide whisker-reinforced silicon nitride composite. J. Am. Ceram. Soc. 78, 10 (1995): 2705.

(125) Zutshi, A., et al. Processing, microstructure, and wear behavior of silicon nitride hot-pressed with alumina and yttria. J. Am. Ceram. Soc. 77, 4 (1994): 883.

(126) Skopp, A. Woydt, M. and Habig, K. H. Tribological behavior of silicon nitride materials under unlubricated sliding between 22 °C and 100 °C, Wear 181-183 (1995): 571-580.

(127) Emoto, H. and Mitomo, M. Control and characterization of abnormally-grown grains in silicon nitride ceramics. J. Eur. Ceram. Soc. 17, 6 (1997): 797–804.

(128) Hendry, A. Thermodynamics of silicon nitride and oxynitride (in Nitrogen Ceramics ed. By Riley, F. L.). Noorhoff-Leyden: Massachusetts, 1977.

(129) Chase, M. W., et al. JANAF Thermodynamical table, 3rd edition, Part II, Cr-Zr. J. Phys. Chem. Ref. Data. 14, 1 (1985): 1677.

APPENDICES

Appendix A

1) Data for calculating equilibrium P_{SiO}, Po_2 and free energy of formation of Si_2N_2O

at various temperatures under specific atmosphere. The data are given in Table A-1.

Table A-1 $\Delta G°$ (β-Si_3N_4(s)), $\Delta G°$ (SiO_2(l)) and $\Delta G°$ (Si_2N_2O(s)) at 1400 – 1700 °C

Temperature (°C)	#$\Delta G°$(β-Si_3N_4(s)) [kcal.mol^{-1}]	*$\Delta G°$(SiO_2(l)) [kcal.mol^{-1}]	$^\varsigma\Delta G°$(Si_2N_2O(s)) [kcal.mol^{-1}]	$^\varsigma\Delta G°$(SiO(g)) [kcal.mol^{-1}]
1400	-41.19	-146.71	-104.96	-57.52
1500	-30.44	-142.21	-101.83	-58.84
1600	-19.68	-137.57	-98.69	-59.94
1700	-8.93	-132.96	-95.56	-61.04

Calculated by using the equation *(128)*: $\Delta G°$ (β-Si_3N_4) = -925.2 + 0.45T   kJ.mol^{-1}

* Obtained from JANAF thermodynamics table *(129)*

$^\varsigma$ Calculated by using the equation *(128)*: $\Delta G°$ (Si_2N_2O) = -658.3 + 0.131T   kJ.mol^{-1}

2) Calculation of equilibrium P_{SiO} under 1 atm (P_{N2} = 0.8 atm) at 1700 °C for the

equation: **Si_3N_4 (s) + 3SiO_2 (l) $\rightarrow$ 6SiO (g) + 2N_2 (g)**

Given data; $\Delta G°$ (β-Si_3N_4(s)) = -8.93   kcal.mol^{-1}

$\Delta G°$ (SiO_2(l))   = -132.96 kcal.mol^{-1}

$\Delta G°$ (SiO(g))   = -61.04   kcal.mol^{-1}

$\Delta G°$ (N_2(g))   = 0   kcal.mol^{-1}

$\Delta G°_{reaction}$ = $G°_{products}$ − $G°_{reactants}$

= [(6(-61.04) + 0] – [(-8.93) + (3(-132.96))]

= 41.558 kcal.mol^{-1}

At equilibrium; $\Delta G°_{reaction}$ = –RTlnK

$$41.558 \text{ kcal.mol}^{-1} \quad = \quad -RT\ln\left[\frac{(P_{SiO})^6.(P_{N2})^2}{a_{Si3N4}.(a_{SiO2})^3}\right]$$

$$\ln\left[\frac{(P_{SiO})^6.(P_{N2})^2}{(1)}\right] \quad = \quad [-41558 \text{ cal.mol}^{-1}]/ RT$$

$$\ln(P_{SiO})^6 = [-41558 \text{ cal.mol}^{-1}]/(1.987 \text{ cal.mol}^{-1}\text{K}^{-1} \times 1973 \text{ K}) - \ln(0.8 \text{ atm})^2$$

$$\ln(P_{SiO})^6 = -10.15$$

$$(P_{SiO})^6 = 3.91 \times 10^{-5} \text{ atm}$$

$$\therefore \quad P_{SiO} \quad = 1.84 \times 10^{-1} \text{ atm} = \underline{1.84 \times 10^4 \text{ Pa}}$$

The other calculated data of P_{SiO} at temperature ranging from 1400 – 1700 °C are

shown in Table A-2.

Table A-2 Equilibrium P_{SiO} under 1 atm (P_{N2} = 0.8 atm) at 1400 – 1700 °C

Temperature (°C)	P_{SiO} (Pa)	log P_{SiO} (Pa)
1400	5.75×10^2	2.76
1500	7.80×10^2	2.89
1600	4.14×10^3	3.62
1700	1.84×10^4	4.26

3) Calculation of equilibrium P_{SiO} for P_{O_2} = 1 atm and P_{N2} = 1 atm, at 1400 °C for the

equation: **2Si₃N₄ (s) + 3O₂ (g) → 6SiO (g) + 4N₂ (g)**

Given data; $\Delta G°$ (β-Si₃N₄(s)) = -41.19 kcal.mol⁻¹

$\Delta G°$ (O₂(g)) = 0 kcal.mol⁻¹

$\Delta G°$ (SiO(g)) = -57.52 kcal.mol⁻¹

$\Delta G°$ (N₂(g)) = 0 kcal.mol⁻¹

$$\Delta G^{\circ}_{reaction} \;=\; G^{\circ}_{products} \;-\; G^{\circ}_{reactants}$$

$$= \;[(6(-57.52) + 0)] - [2(-41.19) + 0]$$

$$= \;-262.74 \; kcal.mol^{-1}$$

At equilibrium; $\Delta G^{\circ}_{reaction} \;=\; -RTlnK$

$$-262.74 \; kcal.mol^{-1} \;\;=\; -RTln\left[\frac{(P_{SiO})^6.(P_{N2})^4}{(a_{Si3N4})^2.(P_{O2})^3}\right]$$

$$ln\left[\frac{(P_{SiO})^6.(1)}{(1)(1)}\right] \;=\; [262740 \; cal.mol^{-1}]/ \; RT$$

$$ln\,(P_{SiO})^6 \;=\; [262740 cal.mol^{-1}]/(1.987 \; cal.mol^{-1}K^{-1} \times 1673 \; K)$$

$$ln\,(P_{SiO})^6 \;=\; 79.04$$

$$(P_{SiO})^6 \;=\; 2.12 \times 10^{34} \; atm$$

$$\therefore \;\; P_{SiO} \;\;\;=\; 5.40 \times 10^5 \; atm \;=\; \underline{5.40 \times 10^{10} \; Pa}$$

The other calculated data of P_{SiO} with different Po_2 at temperature ranging from 1400

– 1700 °C are shown in Table A-3.

Table A-3 Equilibrium P_{SiO} with different Po_2 at temperature ranging from 1400 –
1700 °C

Temperature (°C)	P_{SiO} (Pa)			
	$Po_2 = 1$ atm	$Po_2 = 10^{-5}$ atm	$Po_2 = 10^{-10}$ atm	$Po_2 = 10^{-15}$ atm
1400	5.40×10^{10}	1.69×10^8	5.28×10^5	1.60×10^3
1500	1.02×10^{11}	3.20×10^8	1.00×10^6	3.10×10^3
1600	1.74×10^{11}	5.44×10^8	1.70×10^6	5.30×10^3
1700	2.79×10^{11}	8.72×10^8	2.73×10^6	8.50×10^3

4) Calculation of the Gibb's free energy on the formation of Si_2N_2O at 1400 °C by the

equation: **Si_3N_4 (s) + SiO_2 (l) $\rightarrow$ 2Si_2N_2O (s)**

Given data; $\Delta G°$ (β-Si_3N_4(s)) = -41.19   kcal.mol^{-1}

$\Delta G°$ (SiO_2(l))   = -146.71   kcal.mol^{-1}

$\Delta G°$ (Si_2N_2O(s))   = -104.96   kcal.mol^{-1}

$\Delta G°_{reaction}$ = $G°_{products}$ − $G°_{reactants}$

= [2(-104.96)] – [(-41.19) + (-146.71)]

= -22.02 kcal.mol^{-1}

The calculated data at other temperatures and $\Delta G°$ (Si_2N_2O) formed by the other

equations are summarized in Table A-4.

Table A-4 Gibb's free energy for the formation of 1 mol Si_2N_2O by various reactions
and temperatures

Reaction	$\Delta G°_{reaction}$ [kcal.mol^{-1}]			
	1400 °C	1500 °C	1600 °C	1700 °C
Si_3N_4 (s) + SiO_2 (l) $\rightarrow$ 2Si_2N_2O (s)	-11.01	-15.51	-20.07	-24.62
Si_3N_4 (s) + 3SiO (g) + N_2 (g) $\rightarrow$ 3Si_2N_2O (s)	-33.71	-32.87	-32.20	-31.54
4Si_3N_4 (s) + 3O_2 (g) $\rightarrow$ 6Si_2N_2O (s) + 2N_2 (g)	-77.50	-81.54	-85.57	-89.61

Appendix B
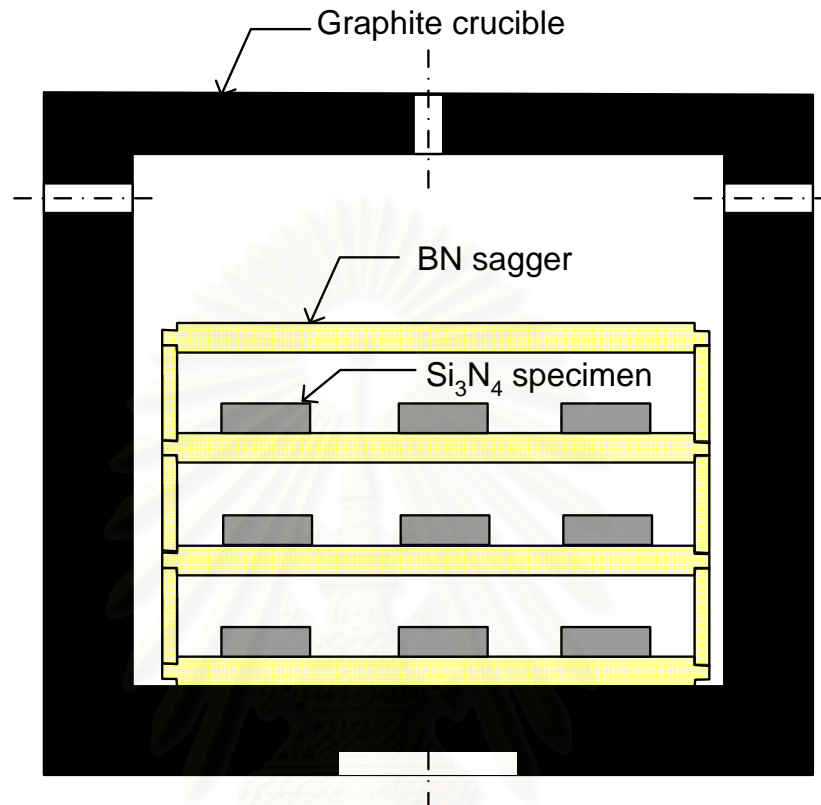
Fig. B-1 Schematic crucible structure for setting Si_3N_4 green specimens for sintering in high temperature furnace controlling atmosphere with N_2 gas

Appendix C

Table C-1 Mass loss of Si_3N_4 specimens with MgO-Al_2O_3 additives sintered at various conditions under N_2 gas pressure of 1.0 MPa.

Formula	Sintering temperature (°C)/soaking time (h)					
	1700/2	1750/2	1800/2	1850/2	1850/0.5	1850/6
M0.5A0.5	3.05±0.11	4.27±0.19	5.80±0.01	5.56±0.07		
M1A1	2.85±0.12	4.02±0.14	5.58±0.08	4.18±0.11		
M2A2	2.04±0.04	3.02±0.21	3.56±0.14	4.50±0.32	2.42±2.25	9.45±0.34
M3A3	1.82±0.15	2.58±0.14	3.34±0.29	4.60±0.31		
M4A4	2.15±0.10	2.91±0.21	3.59±0.32	5.81±0.36		
M5A5	2.24±0.08	3.12±0.34	4.01±0.30	5.92±0.61		
10SN7M2A2	1.04±0.14	1.36±0.04	1.72±0.06	2.46±0.08		
25SN7M2A2	1.12±0.17	1.61±0.45	2.02±0.13	2.99±0.84		
50SN7M2A2	1.24±0.12	1.69±0.04	2.18±0.11	3.11±0.09		
100SN7M2A2	1.08±0.05	1.48±0.15	1.92±0.10	2.56±0.59		
50SN7M4A4	1.41±0.03	1.83±0.21	2.56±0.12	3.40±0.43		

* All of the values are averaged from at least 3 disc specimens

Table C-2 Bulk density of Si_3N_4 specimens with MgO-Al_2O_3 additives sintered at various conditions under N_2 gas pressure of 1.0 MPa.

Formula	Sintering temperature (°C)/soaking time (h)					
	1700/2	1750/2	1800/2	1850/2	1850/0.5	1850/6
M0.5A0.5	2.48±0.01	2.54±0.02	2.52±0.02	2.71±0.00		
M1A1	2.76±0.01	2.86±0.01	2.92±0.01	3.03±0.13		
M2A2	3.12±0.00	3.15±0.01	3.17±0.00	3.16±0.01	3.14±0.00	3.20±0.01
M3A3	3.15±0.00	3.15±0.00	3.16±0.01	3.15±0.01		
M4A4	3.14±0.00	3.14±0.01	3.13±0.02	3.03±0.02		
M5A5	3.12±0.00	3.05±0.05	2.96±0.05	2.89±0.04		
10SN7M2A2	2.80±0.02	2.96±0.00	3.10±0.01	3.12±0.01		
25SN7M2A2	2.78±0.02	2.97±0.02	3.09±0.00	3.15±0.01		
50SN7M2A2	2.28±0.05	2.93±0.00	3.06±0.02	3.11±0.00		
100SN7M2A2	3.04±0.00	3.13±0.00	3.16±0.00	3.16±0.00		
50SN7M4A4	3.11±0.01	3.12±0.00	2.88±0.04	2.85±0.13		

* All of the values are averaged from at least 3 disc specimens

Appendix D

Table D-1 Flexural strength of Si_3N_4 specimens with MgO-Al_2O_3 additives sintered at various conditions under N_2 gas pressure of 1.0 MPa.

Specimen	Flexure strength (MPa)					
	M2A2-1850/2h	M2A2-1800/2h	M3A3-1800/2h	M4A4-1800/2h	M2A2-1850/0.5h	M2A2-1850/6h
1	558	473	505	508	451	526
2	501	567	514	439	476	523
3	494	485	511	533	533	576
4	572	593	467	453	504	487
5	575	544	527	516	454	497
6	572	570	465	486	461	497
7	564	513	551	513	496	550
8	519	567	510	491	548	569
9		513	509	470		
Average	*544*	*536*	*507*	*490*	*490*	*528*
S.D.	*34*	*42*	*27*	*31*	*36*	*34*

Table D-2 Flexural strength of Si_3N_4 specimens with Y_2O_3-Al_2O_3 additives sintered at various conditions under N_2 gas pressure of 1.0 MPa.

Specimen	Flexure strength (MPa)		
	Y3A3-1850/2h	**Y4A4-1850/2h**	**Y5A3-1850/2h**
1	531	505	553
2	481	524	516
3	512	518	610
4	505	541	533
5	457	490	551
6	482	502	480
7	489	556	557
8	486	472	
Average	*493*	*514*	*543*
S.D.	*23*	*27*	*40*

Table D-3 Flexural strength of Si_3N_4 ceramics prepared from α and β powder mixtures with $MgO-Al_2O_3$ additives sintered under N_2 gas pressure of 1.0 MPa

Specimen	Flexure strength (MPa)			
	10SN7M2A2-1850/2h	25SN7M2A2-1850/2h	50SN7M2A2-1850/2h	100SN7M2A2-1850/2h
1	500	548	536	549
2	524	486	574	596
3	575	518	552	718
4	487	587	504	661
5	426	586	617	583
6	573	479	590	637
7	440	469	557	
Average	*504*	*525*	*562*	*624*
S.D.	*59*	*50*	*37*	*61*

Table D-4 Vickers hardness (Hv) of Si_3N_4 specimens with MgO-Al_2O_3 additives sintered at various conditions under N_2 gas pressure of 1.0 MPa.

Specimen	Hv (GPa)					
	M2A2-1850/2h	M2A2-1800/2h	M3A3-1800/2h	M4A4-1800/2h	M2A2-1850/0.5h	M2A2-1850/6h
1	15.6	14.0	14.1	13.1	12.3	14.5
2	15.8	14.7	13.4	13.4	12.0	14.3
3	15.8	14.8	13.7	13.9	12.0	14.5
4	16.2	14.7	13.0	13.7	12.2	13.9
5	15.8	14.9	13.9	13.1	12.1	14.1
6	16.2	14.4	13.4	13.4	12.4	13.9
7	16.4	14.5	14.0	14.1	12.2	14.0
8	16.2	14.1	14.3	13.2		
9	16.1	14.7	13.7	13.4		
10	15.6	14.5	14.2	13.3		
Average	*16.0*	*14.5*	*13.8*	*13.5*	*12.2*	*14.1*
S.D.	*0.3*	*0.3*	*0.4*	*0.3*	*0.1*	*0.3*

Table D-5 Vickers hardness (Hv) of Si_3N_4 specimens with Y_2O_3-Al_2O_3 additives sintered at various conditions under N_2 gas pressure of 1.0 MPa.

Specimen	Hv (GPa)		
	Y3A3-1850/2h	Y4A4-1850/2h	Y5A3-1850/2h
1	11.5	13.9	14.2
2	11.5	13.9	13.5
3	11.8	13.7	13.6
4	11.7	13.5	13.7
5	11.8	13.5	13.5
6	11.4	13.6	13.6
7	12.1	13.3	13.5
Average	*11.7*	*13.6*	*13.6*
S.D.	*0.3*	*0.2*	*0.2*

Table D-6 Fracture toughness (K_{IC}) of Si_3N_4 specimens with $MgO-Al_2O_3$ additives sintered at various conditions under N_2 gas pressure of 1.0 MPa.

Specimen	K_{IC} (MPa m$^{1/2}$)					
	M2A2-1850/2h	M2A2-1800/2h	M3A3-1800/2h	M4A4-1800/2h	M2A2-1850/0.5h	M2A2-1850/6h
1	5.5	5.2	4.3	4.7	4.7	5.8
2	7.0	4.5	4.7	4.8	5.1	5.7
3	5.7	5.4	4.3	5.1	5.4	6.1
4	5.6	4.7	4.8	4.7	5.4	5.7
5	6.2	4.8	4.5	5.0	5.4	5.2
6	5.6	4.8	4.5	4.9	5.0	5.6
7	6.0	4.2	4.2	4.3	5.7	6.0
8	6.2	4.5	4.3	4.6		
9	5.7	5.9	4.8	4.7		
10	5.3	4.2	5.1	4.6		
Average	*5.9*	*4.8*	*4.5*	*4.7*	*5.2*	*5.7*
S.D.	*0.5*	*0.5*	*0.3*	*0.2*	*0.3*	*0.3*

Table D-7 Fracture toughness (K_{IC}) of Si_3N_4 specimens with Y_2O_3-Al_2O_3 additives sintered at various conditions under N_2 gas pressure of 1.0 MPa.

Specimen	K_{IC} (MPa m$^{1/2}$)		
	Y3A3-1850/2h	Y4A4-1850/2h	Y5A3-1850/2h
1	4.9	5.7	5.8
2	4.9	5.4	5.1
3	4.6	5.1	4.6
4	4.6	5.3	4.8
5	4.6	4.9	5.2
6	4.9	5.7	5.5
7	4.4	5.2	5.1
Average	*4.7*	*5.3*	*5.2*
S.D.	*0.2*	*0.3*	*0.4*

List of Publications and Presentations

Publications

1. Nirut Wangmooklang, Kuljira Sujirote, Supatra Jinawath and Shigetaka Wada. Gas/solid reaction during sintering of Si_3N_4 ceramics in an air furnace. J. Eur. Ceram. Soc. 27 (2007): 2111-2117.

2. Nirut Wangmooklang, Kuljira Sujirote, Thanakorn Wasanapiarnpong, Supatra Jinawath and Shigetaka Wada. Properties of Si_3N_4 ceramics sintered in an air and nitrogen atmosphere furnaces. (submitted)

3. Nirut Wangmooklang, Kuljira Sujirote, Thanakorn Wasanapiarnpong, Supatra Jinawath and Shigetaka Wada. Sintering and properties of Si_3N_4 ceramics prepared from low-cost β-powder with MgO-Al_2O_3 additives. (to be submitted)

Presentations

1. Nirut Wangmooklang, Kuljira Sujirote and Shigetaka Wada. Sintering of MgO and Al_2O_3 doped β-Si_3N_4 powder in air atmosphere furnace and properties of the sintered ceramics. *The 3th Thailand Materials Science and Technology Conference*. Bangkok, Thailand, 10-11 August 2004 (Poster)

2. Nirut Wangmooklang, Khantima Hemra and Shigetaka Wada. Improvement of attrition mill. *The 3th Thailand Materials Science and Technology Conference*. Bangkok, Thailand, 10-11 August 2004 (Poster)

3. Nirut Wangmooklang, Kuljira Sujirote and Shigetaka Wada. Effect of the length of soaking time on the properties of Si_3N_4 ceramics prepared from low cost β-powder. *The 4th Thailand Materials Science and Technology Conference*, 31 March - 1 April 2006 (Oral)

4. Nirut Wangmooklang, Kuljira Sujirote, Supatra Jinawath and Shigetaka Wada. Comparison between the sintering of Si_3N_4 ceramics under air and nitrogen atmosphere. *10th International Conference and Exhibition of the European Ceramic Society, June 17 - 21, 2007, Berlin* (Accepted for oral presentation)

VITA

Mr. Nirut Wangmooklang was born on 24th November 1977 in Nakhonratchasima, Thailand. He received a Bachelor's Degree in Chemistry from Faculty of Science and Technology, Rajabhat Bansomdejchaopraya University in November 2001. During his Bachelor study, he was also working at the Siam Research and Development Co., Ltd (SCG Group). He received a Master's Degree in the field of Ceramic Technology from the Department of Materials Science, Faculty of Science, Chulalongkorn University in April 2004. After graduation with Master's Degree, he continued studying in the Doctor of Philosophy Program in Materials Science in the Department of Materials Science, Faculty of Science, Chulalongkorn University and graduated in April 2007. He also received the Thailand Graduate Institute of Science and Technology (TGIST) scholarship from the National Science and Technology Development Agency (NSTDA) throughout the course of study.